

Development of X-Ray Beam Size Monitor for
the SuperKEKB Rings

Emy Mulyani

Doctor of Philosophy

Department of Accelerator Science
School of High Energy Accelerator Science
SOKENDAI (The Graduate University for
Advanced Studies)

Development of X-Ray Beam Size Monitor for the SuperKEKB Rings

SuperKEKBでのX線を用いたビームサイズモニターの開発



Emy Mulyani

Department of Accelerator Science
School of High Energy Accelerator Science
The Graduate University for Advanced Studies

A Thesis submitted for the degree of

Doctor of Philosophy

June 2018

Supervisor: Prof. John W. Flanagan
Reviewers: Prof. Toshiyuki Mitsuhashi
Prof. Makoto Tobiyama
Prof. Hitoshi Fukuma
Prof. Gary Varner
Prof. Takashi Naito
Dr. Hitomi Ikeda

Day of submission: 7th of June 2018

Abstract

The objective of this research was dedicated to studying the development of the X-ray beam size monitor (XRM) for vertical beam size measurements in the SuperKEKB rings (Low Energy Ring LER and High Energy Ring HER). The XRM installation images X-rays from a bending magnet through an optical element onto a detector. The studies cover the designing of optical elements, studying the XRM systematics during commissioning of the SuperKEKB operation, and exploring an image reconstruction technique using uniformly redundant arrays (URA) coded aperture. The longterm aim of XRM is to provide high-resolution bunch-by-bunch, turn-by-turn measurements for low-emittance tuning, collision tuning, and instability measurements. The preparations of a deep Si detector and high-speed readout electronics for single-shot measurements using XRM are underway, in the meantime for Phase 1 and 2 commissioning, we used a scintillator screen and CCD camera for multi-shot measurements.

There are two types of the optical element for XRM in both rings: a single pinhole and coded apertures (CA). In the pinhole imaging, the hole should be small to provide resolution. However, a small hole often has an insufficient area to collect enough X-rays to produce an interpretable image. The CA is randomly distributed pinholes to produce an image that is made up of many overlapping images, unrecognizable as the original object. With knowledge of the location of each pinhole, it is possible for the complex overlapping pinhole images to be reconstructed. The capabilities of CA become useful to overcome the limitation of pinhole imaging and provide better resolution. Because CA offers greater open aperture and photon throughput than a single pinhole, it makes CA has a capability for a better statistical resolution in single-shot measurements. Accordingly, three optical elements or masks have been designed and installed at each ring: pinhole, 17 multi-slits, and 12-slits Uniformly Redundant Array (URA).

Several studies (geometrical scale factors, emittance control knob, and beam

lifetime study) were carried out during the commissioning. In Phase 1 (February - June 2016), the measured vertical emittances ε_y are ~ 10 pm for LER (consistent with the optical estimation) and ~ 35 pm for HER ($3.5 \times$ greater than the optical estimation). Analysis of the beam size and lifetime measurements implies unexpectedly large point spread functions (PSF), particularly in the HER. The spatial resolution of the imaging system (defect of focus, diffraction, and spherical aberration) and scattering in the beamline (EGS5 simulation) contribute ~ 6 μm of PSF, which does not adequately account for the observed of the PSF.

The Phase 2 commissioning commenced in May - July 2018, with thinner Be filters, new optical elements, scintillator, and CCD camera with the purpose to reduce the PSF in HER. The Phase 2 study results imply the PSF $\sigma_s \sim 6.6$ μm in HER (corresponding to the spatial resolution of the imaging system and scattering in the beamline), which is $\sim 5 \times$ smaller than in Phase 1. The overall performances of XRM in LER and HER are accurate. The XRM in LER will be able to measure the design beam size at the zero current (~ 14 μm). For the HER, the PSF that we observed during the Phase 2 indicates that the minimum measured beam size corresponds to the emittance at the design current (12.9 pm) and the XRM will be able to measure the design beam size at the zero current (7 μm).

The last part of this thesis explored the fast reconstruction using a URA coded aperture and the possibility to be implemented in the XRM image reconstruction.

Contents

| | | |
|----------|---|-----------|
| 1 | Introduction | 1 |
| 1.1 | SuperKEKB Accelerator Facility | 1 |
| 1.1.1 | Luminosity | 3 |
| 1.1.2 | Nano-beam collision scheme | 4 |
| 1.2 | Beam Instrumentation | 6 |
| 1.3 | Motivation | 7 |
| 1.4 | Structure of the Thesis | 9 |
| 2 | Synchrotron Radiation Theory and Its Application in Beam Diagnostics | 11 |
| 2.1 | Bending Magnet SR Source | 12 |
| 2.2 | SR Application for Transverse Beam Diagnostic | 15 |
| 2.2.1 | Visible light SR Interferometry | 16 |
| 2.2.2 | X-ray imaging | 17 |
| 2.2.3 | Fresnel–Kirchhoff Diffraction | 18 |
| 2.2.4 | Fraunhofer Approximation | 19 |
| 3 | X-Ray Beam Size Monitor | 25 |
| 3.1 | General XRM System | 25 |
| 3.2 | Detector Image Simulation Using Point Response Function | 25 |
| 3.3 | Optical Element Design | 28 |
| 3.3.1 | Optimizing the pinhole (single slit) size | 29 |
| 3.3.2 | Design of the multi-slits coded aperture | 31 |
| 3.3.3 | Design of the URA coded aperture | 33 |

| | | |
|----------|--|-----------|
| 3.4 | Detector Image and Resolution | 36 |
| 3.5 | Apparatus | 38 |
| 3.5.1 | Beamline | 39 |
| 3.5.2 | Optical elements | 40 |
| 3.5.3 | Detector system: Scintillator, lens, camera | 41 |
| 4 | Phase 1 of SuperKEKB Commissioning | 43 |
| 4.1 | Geometrical scale factors | 44 |
| 4.2 | Emittance control knob | 46 |
| 4.3 | Beam lifetime technique | 49 |
| 4.4 | Spatial resolution of the detector system | 53 |
| 5 | Phase 2 of SuperKEKB Commissioning | 57 |
| 5.1 | Strategy in Phase 2 | 57 |
| 5.1.1 | Thinner Be filter | 57 |
| 5.1.2 | Optimizing the pinhole size | 58 |
| 5.2 | Scintillator, lens, and camera system | 59 |
| 5.2.1 | LuAG:Ce Scintillator | 59 |
| 5.2.2 | Lens and camera system | 60 |
| 5.3 | Study results | 60 |
| 6 | Coded Aperture Reconstruction Image | 67 |
| 6.1 | The History of Coded Aperture | 67 |
| 6.1.1 | Fresnel zone plates | 70 |
| 6.1.2 | Random arrays | 70 |
| 6.2 | Fundamental of Code Aperture Imaging | 71 |
| 6.2.1 | Mathematical Formulation of Coded Aperture Imaging | 71 |
| 6.2.2 | Coded Aperture Imaging in X-Ray Beam Size Monitor | 73 |
| 6.2.3 | Implementation | 75 |
| 7 | Summary and Outlook | 79 |
| 7.1 | Summary | 79 |
| 7.1.1 | X-Ray Beam Size Monitor | 79 |
| 7.1.2 | Optical Element | 80 |

| | | |
|-------------------------|---|------------|
| 7.1.3 | Phase 1 and 2 Commissioning | 81 |
| 7.2 | Direction for future work | 81 |
| 7.2.1 | Fast detector for single-shot measurement | 82 |
| 7.2.2 | Image reconstruction based on URA coded aperture | 82 |
| Appendix A | | 83 |
| A.1 | Derivation of the SR spatial distribution emitted by relativistic charges on circular orbit | 83 |
| A.2 | Energy Radiated per-unit Frequency per-unit Solid Angle | 87 |
| Appendix B | | 91 |
| B.1 | Definitions | 91 |
| B.2 | Theorem 1: Correlation with a constant | 91 |
| B.3 | Theorem 2: $(O \times A) \otimes G = O * (A \otimes G)$ | 92 |
| Abbreviations | | 93 |
| Symbol | | 95 |
| List of Figures | | 100 |
| List of Tables | | 109 |
| Bibliography | | 111 |
| Acknowledgements | | 118 |
| Declaration | | 120 |

1 | Introduction

This chapter presents the introduction to the SuperKEKB accelerator facility at the High Energy Accelerator Research Organization (KEK); luminosity, nano-beam collision scheme, and beam instrumentation. Furthermore, the motivation and structure of this dissertation are also described.

1.1 SuperKEKB Accelerator Facility

The KEKB B-factory (KEKB) is an electron-positron collider developed by the KEK to search for CP violation in the B-meson scheme [1]. The operation of the KEKB began in 1998 and finished in 2010. During these 12 years of operations, KEKB recorded a world record for luminosity at $2.1 \times 10^{34} \text{ cm}^{-2}\text{s}^{-1}$ and experimentally proved the CP violation of B and anti-B mesons predicted by Kobayashi and Maskawa (receipts of the 2008 Nobel Physics). The SuperKEKB facility is the upgrade of KEKB to increase the luminosity 40 times, to $8 \times 10^{35} \text{ cm}^{-2}\text{s}^{-1}$, with the overarching mission is to search a new physics beyond the standard model of the particle physics in the B meson regime.

The layout of the SuperKEKB is shown in Fig.1.1. They are two rings in the main ring with circumference $\sim 3 \text{ km}$, High Energy Ring (HER) and Low Energy Ring (LER) for 7 GeV electron and 4 GeV positron, respectively. SuperKEKB incorporated various technologies, i.e., beam pipes with antechambers were adopted to reduce the beam impedance and to relax the irradiation power density of the synchrotron radiation (SR) and suppress the electron-cloud effect, which has been a severe problem in the positron ring [3]. In the upgrading of the SuperKEKB main ring vacuum system, approximately 93% of

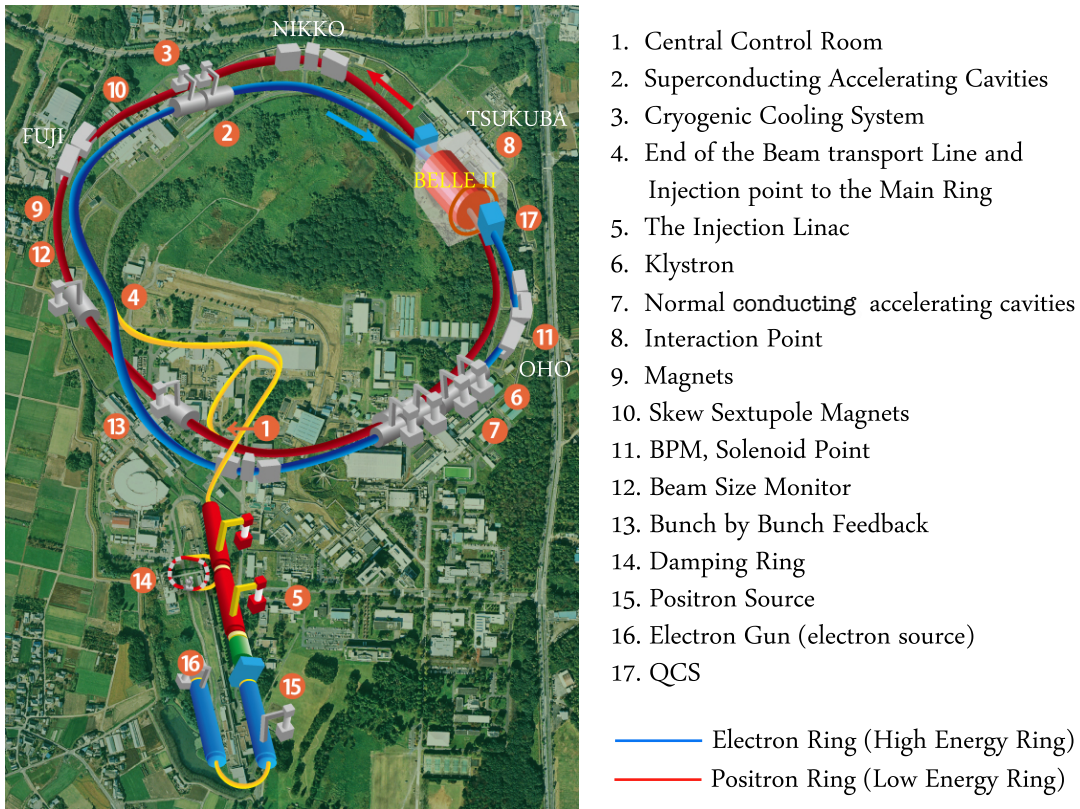


Figure 1.1: Facilities and components of the SuperKEKB accelerator facility. Ring's circumference is ~ 3 km with four experimental hall buildings (Fuji, Nikko, Tsukuba, and Oho) [2].

the beamline pipes and vacuum components of the positron ring were replaced with new ones. On the other hand, approximately 80% of the components in the electron ring were reused because the layout of the magnet did not change significantly [4].

Higher stored current need an upgrade in ARES and Superconducting cavities as well as higher-order mode resistant vacuum components. High precision superconducting quadrupole magnet at the interaction region assembly within the Belle detector, and also upgrade in all subsystems including magnet and power supply, RF system, vacuum, beam diagnostics and feedback, injection and beam abort system, and control safety system. The injector Linac also needs an upgrade in the RF gun, positron source, beam transport and control,

and the new positron damping ring.

1.1.1 Luminosity

In particle physics experiments the energy available for the production of new effects is the most critical parameter. The required large center of mass energy can only be provided with colliding beams where a little or no energy is lost in the motion of the center of the mass system (cms). Besides the energy, the number of the interactions (events) is also an important parameter, especially right when rare events with a small production cross section σ_p are studied. The quantity that measures the ability of a particle accelerator to produce the required number of interactions is called a luminosity \mathcal{L} and is the proportionality factor between the number of events per second dN_e/dt and the cross section σ_p as shown in Eq. 1.1 [5]. The unit of the luminosity, therefore, is $\text{cm}^{-2}\text{s}^{-1}$.

$$\frac{dN_e}{dt} = \mathcal{L} \cdot \sigma_p. \quad (1.1)$$

The luminosity term in Eq. 1.1 can be expanded in more detail as expressed by the Eq. 1.2.

$$\mathcal{L} = \frac{\gamma_{\pm}}{2er_e} \left(1 + \frac{\sigma_y^*}{\sigma_x^*} \right) \left(\frac{I_{\pm} \xi_{y\pm}}{\beta_y^*} \right) \left(\frac{R_L}{R_{\xi_{y\pm}}} \right). \quad (1.2)$$

The suffix \pm specifies the positron (+) and electron (-). The parameters γ , e , and r_e are the Lorentz factor, the elementary electric charge, and the classical electron radius, respectively. These parameters are constant and can not be taken freely. The σ_x^* and σ_y^* represent horizontal and vertical beam sizes with * indicates values at the interaction point (IP). It is assumed the flat beams and equal beam sizes for two beams at IP (horizontal and vertical). The R_L and R_{ξ_y} represent reduction factors for the luminosity and vertical beam-beam parameter. The ratio of these parameters is usually not far from unity. Therefore, the Eq. 1.2 tells us that the luminosity is proportional to the beam current I , the vertical beam-beam parameter ξ_y , and an inverse of the vertical beta function

at IP β_y^* . The vertical beam-beam parameter is described by [6]

$$\xi_{y\pm} = \frac{r_e}{2\pi\gamma_{\pm}} \frac{N_{\mp}\beta_y^*}{\sigma_y^*(\sigma_x^* + \sigma_y^*)} R_{\xi_{y\pm}} \propto \frac{N_{\mp}}{\sigma_x^*} \sqrt{\frac{\beta_y^*}{\varepsilon_y}}, \quad (1.3)$$

where N is the number of particles in a bunch. A maximum value of the beam-beam parameter has been obtained from various colliders in 40 years, is about 0.02 – 0.1. The beam-beam parameter increases with increasing the bunch population. However, the vertical emittance becomes large when the beam-beam parameter reaches the limit. Then, if we back to Eq. 1.2, the luminosity is only proportional to one of the beam currents and becomes a constant value as a result of compensating the increase of the beam current for the decrease of the beam-beam parameter. If we maintain the ratio of the vertical beta function to the vertical emittance with a constant beam current, the vertical beta function can be squeezed with a constant beam-beam parameter [6].

1.1.2 Nano-beam collision scheme

One of the keys for a high luminosity collider is how to make an extremely small beta function at the interaction point (IP). Raimodi developed a nano-beam scheme for the SuperB factory in Italy [7]. The basic idea of it is to squeeze the vertical beta function at the IP β_y^* to its minimum by minimizing the size of the overlap region of the two beams, with a schematic view of the beam collision as shown in Fig. 1.2. The length of d is determined by the half-crossing angle ϕ_x and the horizontal beam size at IP (σ_x^*) as shown in Eq. 1.4 [6]. In the nano-beam scheme, a relatively large horizontal crossing angle, extremely small horizontal emittance and horizontal beta function at IP for both beams are required to shorten the length of d .

$$d = \frac{\sigma_x^*}{\sin\phi_x}. \quad (1.4)$$

The d is much shorter than the bunch length σ_z along the beam axis and should be compared to the vertical beta function at IP β_y^* for the hourglass effect. The

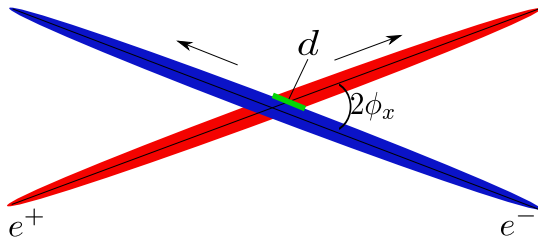


Figure 1.2: Schematic view of beam collision in the nano-beam scheme. The red and blue lines represent positron and electron beams, respectively. The size of the overlap region is d , which is considered to be an effective bunch length for the nano-beam scheme.

β_y^* should satisfy this hourglass requirement:

$$\beta_y^* \geq d = \frac{\sigma_x^*}{\sin\phi_x}, \quad (1.5)$$

Therefore, to squeeze the β_y^* , the effective bunch length, d , is decreased by decreasing the horizontal spot size at the IP and increasing the crossing angle. Therefore, the spot size in the horizontal direction effectively becomes $\sigma_z \sin\phi_x$, which is larger than nominal σ_x^* . The luminosity formula in Eq. 1.2 and beam-beam parameter in Eq. 1.3 are modified by replacing σ_x^* with the effective spot size, $\sigma_z \sin\phi_x$. The horizontal beam-beam parameter in the nano-beam scheme can be small compared to the general head-on scheme [8]:

$$\xi_{x\pm} = \frac{r_e}{2\pi\gamma_{\pm}} \frac{N_{\mp}\beta_x^*}{\sigma_x^*(\sigma_x^* + \sigma_y^*)} R_{\xi_{y\pm}} \propto \frac{N_{\mp}\beta_x^*}{(\sigma_z \sin\phi_x)^2}. \quad (1.6)$$

Based on those considerations, the machine parameters for the SuperKEKB is shown in Table 1.1 and compared with those achieved at KEKB. The vertical emittance is estimated from the sum of contribution from beam-beam interaction and orbit distortion due to a solenoid field in the vicinity of the IP and so on. When a crossing angle 83 mrad, an emittance 3.2 nm, and a horizontal beta function 32 mm, the vertical beta function can be squeezed up to 244 μm while the bunch current length is 6 mm in the LER. The beam-beam parameter is assumed to be 0.09 at the maximum. Finally, the beam currents are

determined to achieve the target peak luminosity $8 \times 10^{35} \text{ cm}^{-2}\text{s}^{-1}$. The beam currents and beta function for SuperKEKB become approximately twice and $1/20$ of KEKB, respectively.

Table 1.1: Final machine parameters for the KEKB and SuperKEKB [6, 8–11].

| Parameter | | KEKB | SuperKEKB | Unit |
|-----------------------------|-----------------|---------------------|-----------------------------|-------------------------------|
| | | Achieved LER/HER | Nano-beam scheme LER/HER | |
| Beam Energy | E_b | 3.5/8.0 | 4.000 / 7.007 | GeV |
| Beam current | I | 1.64/1.19 | 3.6/ 2.6 | A |
| Bunches current | I_b | 1.44 | 1.04 | mA |
| Number of bunches/ring | n_b | 1585 | 2,500 | |
| Circumference | C | 3,016 | 3,016 | m |
| Half Crossing angle | ϕ_x | 11 | 41.5 | mrاد |
| Horizontal Emittance | ε_x | 18 | 3.2 (1.9)/4.6 (4.4) | nm |
| Vertical Emittance | ε_y | 360 | 8.64 (2.8)/12.9 (1.5) | pm |
| Horizontal β function | β_x^* | 1200/1200 | 32 /25 | mm |
| Vertical β function | β_y^* | 5.9/5.9 | 0.27/ 0.3 | mm |
| Horizontal beam size | σ_x^* | 147/170 | 10 /11 | μm |
| Vertical beam size | σ_y^* | 940 | 48/62 | nm |
| Bunch length | σ_z | 6 \sim 7 | 6 (4.7)/5 (4.9) | mm |
| Luminosity | \mathcal{L} | 2.11 | 80×10^{34} | $\text{cm}^{-2}\text{s}^{-1}$ |
| Beam-beam parameter | ξ_y | 0.129/0.09 | 0.088/0.082 | |

The LER (Low Energy Ring) is the positron ring and the HER (High Energy Ring) is the electron ring. The * and (): indicate values at interaction point (IP) and zero current, respectively.

1.2 Beam Instrumentation

Beam instrumentation and diagnostics combine the disciplines of accelerator physics with mechanical, electronics, and software engineering, making it a

fascinating field in which to work. Beam instrumentation in the accelerator is the 'eyes' of the machine operators, its entail the design, construction and operation of instruments to observe particle beams, and also the research and development to find new or improve existing technique to fulfill particularly new requirements. Several beam parameters that we need to measure in the accelerator (i.e., circular collider) are beam position (to know the horizontal and vertical positions of the beam throughout the accelerator chamber), beam intensity, and lifetime measurement. Other parameters are beam loss, beam profile (actual shape of the beam, both transverse and longitudinal planes), and collision rate to measure of how well the beams overlap at the collision point.

In the SuperKEKB, the beam instrumentation to be installed is shown in Table 1.2. To maintain a stable collision condition of the SuperKEKB, precise beam control based on the beam instrumentations, such as beam-position monitors (BPMs), beam-size monitors, and tune monitors, are highly required. To realize a high luminosity, SuperKEKB is operated at high beam current with extremely many beam bunches (2500 bunches). Therefore, the beam-feedback system that is used to suppress strong coupled-bunch instabilities is indispensable for the stable accelerator operation.

1.3 Motivation

The motivation of the present research was the development of the X-ray beam size monitor (XRM) for the SuperKEKB rings, consisting of designing the mask patterns, studying of the XRM systematics during the commissioning of the SuperKEKB operation, and exploring the image reconstruction technique using uniformly redundant arrays (URA) coded apertures.

When the LER and HER beams achieve their targeted low emittances (see Table 1.1), the vertical beam sizes at the monitor source points are less than 18 μm in both rings. The resolution of the SR interferometer is fundamentally limited by the measurement wavelength λ and the opening angle between slits as seen from the beam source point, as well as the maximum visibility Γ (fringe

Table 1.2: Beam Instrumentation of SuperKEKB [12].

| System | Quantity | |
|---|---------------|---------------|
| | LER (e^+) | HER (e^-) |
| Beam position monitor (BPM) | 444 | 486 |
| BPM displacement sensor | 108 | 110 |
| Gate turn-by-turn monitor | 59 | 58 |
| Transverse bunch-by-bunch feedback | 2 | 2 |
| Longitudinal bunch-by-bunch feedback | 1 | 0 |
| Visible synchrotron radiation (SR) size monitor | 1 | 1 |
| X-ray beam size monitor (XRM) | 1 | 1 |
| Beamstrahlung monitor | 1 | 1 |
| Betatron tune monitor | 2 | 2 |
| Beam loss monitor | | 200 |
| DCCT | 1 | 1 |
| CT | 1 | 1 |
| Bunch current/fill pattern monitor | 1 | 1 |

modulation) that can be reliably measured. For a Gaussian beam, the beam size is given by $\sigma_{beam} = \frac{\lambda}{\pi} \frac{F_{SRM}}{D_{SRM}} \sqrt{1/2 \ln 1/\Gamma}$.

The opening angle is in principle limited by the SR opening angle and by mechanical considerations, with the latter being the dominant restriction at SuperKEKB; the mirrors are located in antechambers to minimize Higher Order Mode (HOM) losses, with the height of the antechambers limited by the pole gap of upstream quadrupole magnets to 24 mm in height. The mirrors are located at a distance of 24.5 (23.5) m downstream of the source point in the LER (HER), so with a maximum effective slit separation of 20 mm at the mirror location, the slits opening angle is 0.8 (0.9) mrad in the LER (HER).

For a 400 nm measurement wavelength, it would be necessary to be able to measure visibilities of around 98% to measure the vertical beam sizes at the source points, which is extremely challenging. In the horizontal direction, the beam sizes are 10 times (or more) larger than those in the vertical direction,

so the required measurable maximum visibility is more reasonable than in the vertical direction (around 90%) [9]. Furthermore, the SR interferometer will not be adequate for single-shot (bunch-by-bunch, turn-by-turn) measurements, which are useful for studying beam instabilities, because of limited photon statistics at short integration times.

An X-ray Beam Size Monitor (XRM) [13] based on a coded aperture (CA) [14] is being developed for SuperKEKB. The longterm aim of XRM is to provide high-resolution bunch-by-bunch, turn-by-turn measurements for low-emittance tuning, collision tuning, and instability measurements. The preparations of a deep Si detector and high-speed readout electronics for single-shot measurements using XRM are underway, in the meantime for Phase 1 and 2, we used a scintillator screen and CCD camera for multi-shot measurements. CA imaging was initially developed by X-ray astronomers using a pattern mask to modulate the incoming light. The projected image is then decoded using the known mask pattern, allowing the original image to be reconstructed. The large open aperture provides much higher photon throughput than a single pinhole, allowing better photon statistics in single-shot measurements. Accordingly, there are two types of SR monitor on each SuperKEKB ring: visible SR interferometers, primarily used for horizontal beam size measurements, and XRM, primarily used for the vertical beam size measurements.

1.4 Structure of the Thesis

This thesis is structured into seven chapters. The followings are the short description of each chapter.

- Chapter 2 describes the characteristic of synchrotron radiation, especially the radiation from the bending magnet, and the synchrotron radiation application for transverse beam diagnostics.
- Chapter 3 explains the concept of XRM. This chapter includes the general XRM system, image simulation using point response function, optical system design, detector image and resolution, and apparatus of the XRM.
- Chapter 4 explains several studies in Phase 1 of SuperKEKB commis-

sioning. These studies cover; geometrical scale factors check, emittance control knob, and beam lifetime study.

- Chapter 5 explains the study during the Phase 2 of SuperKEKB commissioning. These cover the emittance control knob and beam lifetime study.
- Chapter 6 explores the image reconstruction technique with the uniformly redundant array (URA) coded aperture.
- Chapter 7 presents the summary of the thesis and plan.

2 | Synchrotron Radiation Theory and Its Application in Beam Diagnostics

Synchrotron Radiation (SR) has been investigated theoretically for over a century. The fundamental theoretical considerations and investigations of the radiation emitted by the relativistic charged particles in circular motion goes back to the work of Liénard (1898) followed by Schott (1933), Ivanenko and Pomeranchuk (1944), Schwinger (1945), and others; but the first observation—literally, since it was visible light that was generated—came at the General Electric Research Laboratory in Schenectady, New York, on April 24, 1947 [15].

The unique property of SR has its origin in the fact that, for a charged particle moving with speed close to the speed of light toward a stationary observer, the motion appears to occur on a time scale much shorter than the real motion [16]. Nowadays, SR is widely produced by the use of dedicated synchrotron and is employed in applications, ranging from solid-state physics to medicine. More related to this thesis work, SR results as a powerful tool for non-invasive beam diagnostics and a valuable tool for accelerator operation.

There are three kinds of SR sources, bending magnets, wigglers, and undulators. In this chapter, the general formulas describing the SR from bending magnets in the circular accelerator will be discussed. Furthermore, two techniques for exploiting the SR for beam diagnostics are also described: Visible light interferometry and X-ray monitor (XRM). The derivation and discussion of the synchrotron radiation theory in this section are based on Jackson [17],

Kim [18], and Wille [19].

2.1 Bending Magnet SR Source

In the bending magnet, charged particles move in a circular trajectory, producing a smooth spectrum. The total SR radiated power in the relativistic can be expressed by [19]:

$$P_{tot} = \frac{e^2 c}{6\pi\epsilon_0(m_0c^2)^4} \frac{E_b^4}{\rho^2}. \quad (2.1)$$

Its angular distribution can be derived based on [20, 21] as in Appendix A.1 and results to be:

$$\frac{dP}{d\Omega} = \frac{1}{c\mu_0} \frac{e^2}{(4\pi\epsilon_0)^2} \frac{\beta^4 (\beta^2 - 1) \sin^2 \psi \cos^2 \phi + (1 - \beta \cos \psi)^2}{\rho^2 (1 - \beta \cos \psi)^5}, \quad (2.2)$$

where e is the charge of the electron, β is the velocity, ψ is the angle between the direction of the particle acceleration and the direction of observation, c is the velocity of light, μ_0 is the permeability, ϵ_0 is dielectric constant, and ρ is the radius of instantaneous curvature of the electron trajectory. Figure 2.1 shows that, for the relativistic case, the synchrotron radiation occurs in a narrow cone of nominal angular width γ^{-1} in the direction of the observer.

The general form of the power radiated per unit solid angle is

$$\frac{dP(t)}{d\Omega} = \left| \mathbf{A}(t) \right|^2, \quad (2.3)$$

where

$$\mathbf{A}(t) = \left(\frac{c}{4\pi} \right)^{1/2} [R\mathbf{E}]_{ret}. \quad (2.4)$$

The \mathbf{E} being the electric field, and subscript '*ret*' describe the emitter time/real motion of the particle. The total energy radiated per unit solid angle is the

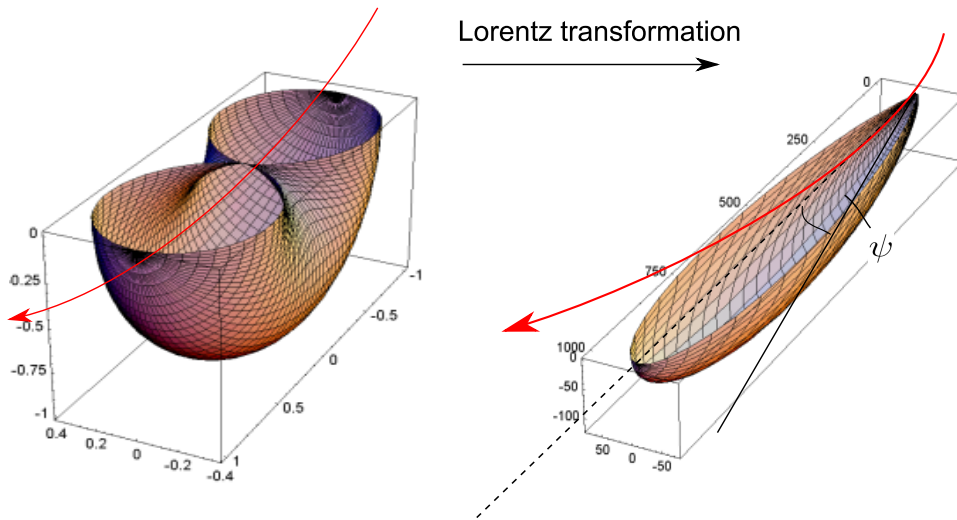


Figure 2.1: Lorentz transformation for the relativistic case, shapes the emitted SR angular distribution in a forward narrow cone: (left) Power distribution in the center of mass frame ($v = 0$), and (right) Power distribution in the laboratory frame ($v = 0.9c$) [19].

time integral of Eq. 2.1:

$$\frac{dW}{d\Omega} = \int_{-\infty}^{\infty} |\mathbf{A}(t)|^2 dt. \quad (2.5)$$

Furthermore, the energy radiated per unit frequency per unit solid angle can be derived based on [17] as in Appendix A.2 and results to be:

$$\frac{d^2I}{d\Omega d\omega} = \frac{e^2}{3\pi^2c} \left(\frac{\omega\rho}{c}\right)^2 \left(\frac{1}{\gamma^2} + X^2\right)^2 \left[K_{2/3}^2(\xi) + \frac{X^2}{(1/\gamma^2) + X^2} K_{1/3}^2(\xi) \right], \quad (2.6)$$

where K is a modified Bessel function of the second kind, and ξ is defined as $\xi = \omega\rho/3c\gamma^3(1 + \gamma^2\Theta^2)^{3/2}$. The first term in the square bracket corresponds to radiation polarized in the plane of the orbit, and the second to radiation polarized perpendicular to that plane.

For the beam of parallel charges with current I , the spectral flux into a small

bandwidth $\Delta\omega$ can be expressed as [18]:

$$\frac{d^2 F}{d^2 \Omega} = \alpha \frac{\Delta\omega}{\omega} \frac{I}{e} |\mathbf{A}(\omega)|^2, \quad (2.7)$$

where $\alpha = e^2/4\pi\epsilon_0\hbar c = 1/137$ is the fine-structure constant. Correspond to radiation polarized (σ -component for radiation polarized in the plane of the orbit and π -component for radiation polarized perpendicular in that plane), it can be expressed as

$$\begin{bmatrix} \frac{d^2 \mathcal{F}_\sigma}{d^2 \Omega} \\ \frac{d^2 \mathcal{F}_\pi}{d^2 \Omega} \end{bmatrix} = \frac{3\alpha}{4\pi^2} \gamma^2 \frac{\Delta\omega}{\omega} \frac{I}{e} \left(\frac{\omega}{\omega_c}\right)^2 (1 + X^2)^2 \begin{bmatrix} K_{2/3}^2(\eta) \\ \frac{X}{1+X^2} K_{1/3}^2(\eta) \end{bmatrix}, \quad (2.8)$$

where the variables η , X , and critical frequency ω_c are defined as

$$\begin{aligned} \eta &= \frac{1}{2} \frac{\omega}{\omega_c} (1 + X^2)^{\frac{3}{2}}, \\ X &= \gamma\psi, \\ \omega_c &= \frac{3\gamma^3 c}{2\rho}. \end{aligned} \quad (2.9)$$

In the plane of the bending radius ($\psi=0$), the flux for the π -component vanishes and for the practical units (photons/s/mrad²/0.1%BW) the distribution of the SR spectral flux becomes [18]

$$\frac{d^2 F}{d^2 \Omega} \Big|_{\psi=0} = 1.33 \times 10^{13} E_{el}^2 [\text{GeV}] I_{el} [A] \left(\frac{\omega}{\omega_c}\right)^2 K_{2/3}^2 \left(\frac{\omega}{2\omega_c}\right), \quad (2.10)$$

giving the spectral flux per mrad² solid angle and per 0.1% photon energy bandwidth. If we use the parameter values for a bending magnet at each of the SuperKEKB rings (LER and HER), we can plot the spectral distribution of the SR as shown in Fig. 2.2

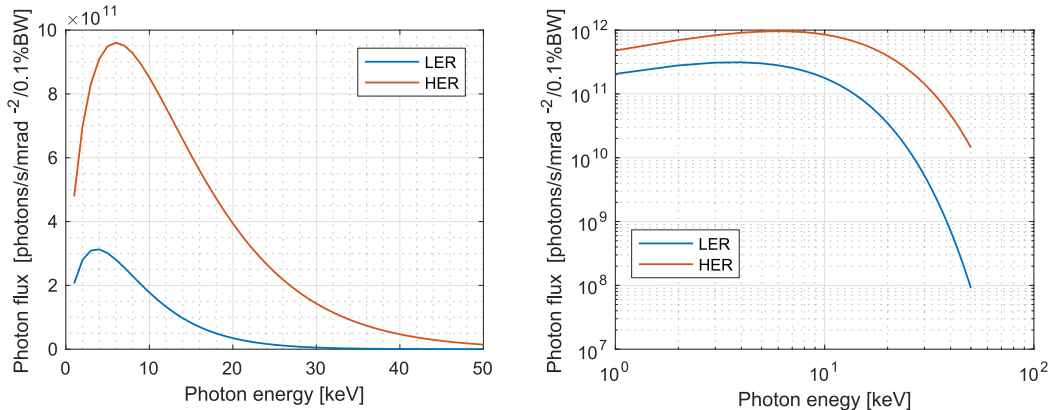


Figure 2.2: The spectral distribution of synchrotron radiation from bending magnet for LER and HER in linear scale (left) and log scale (right). The critical energies are 4.4 and 7.2 keV for LER and HER, respectively. The critical energy corresponds to critical frequency ω_c , and divides the spectrum into two parts of equal radiated power: 50% of the total power is radiated at frequencies lower than ω_c and 50% is radiated at frequencies higher than ω_c . In the X-ray beam size monitor, we are using $E > E_c$

2.2 SR Application for Transverse Beam Diagnostic

SR is a tool for non-destructive beam diagnostics since its characters are substantially related to those of the source beam and generally used in accelerator and storage rings. By studying the pulsed nature of SR, originated from the bunched structure of the beam, the longitudinal profiling of the entire ring can be performed. Additionally, since the SR brilliance is dominated by transverse size and angular divergence of the beam, probing its intensity distribution gives direct information of the beam transverse profiles. An example overview of the methods presently applied to exploit SR for transverse beam diagnostics purpose is given in [22] and [23]. For the SuperKEKB, there are two kinds of SR monitor for transverse beam diagnostics, visible light SR interferometry and XRM, primarily for horizontal and vertical beam size measurements, respectively. However, since the development of XRM is the primary topic of this thesis, the SR interferometry technique will be briefly presented in the subsection 2.2.1.

2.2.1 Visible light SR Interferometry

An alternative technique to SR imaging, for non-destructive beam diagnostics, is the SR interferometry. A rigorous derivation of the principle can be found in [24, 25]. In the following, a brief overview of the technique is given. The interferometry instrument is a wavefront-division type of two-beam interferometer using polarized quasi-monochromator light. The SR interferometer uses a double slit to sample the incoming wavefront and obtain the interference pattern along the vertical or horizontal axis with the schematic setup as shown in Fig. 2.3.

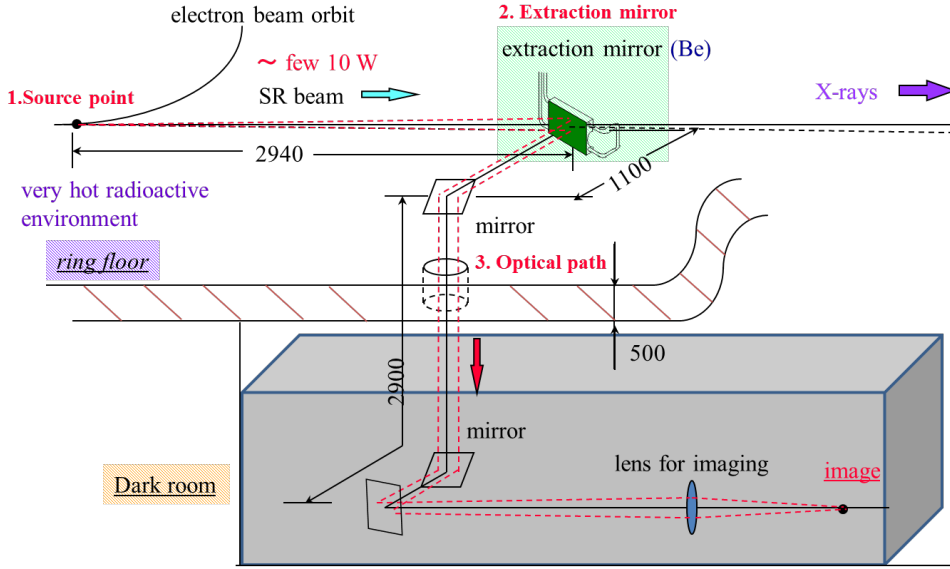


Figure 2.3: Setup of the SR monitor based on visible light interferometry at Photon Factory, KEK [26].

With this interferometer setup, the intensity of the interferogram is given by [24]

$$I(y, D) = (I_1 + I_2) \left\{ \text{sinc} \left(\frac{\pi a y \chi(D)}{\lambda f} \right) \right\} \cdot \left\{ 1 + \Gamma \cos \left(k D \left(\frac{y}{f} + \Psi \right) \right) \right\}$$

$$\Gamma = \left(\frac{2\sqrt{I_1 I_2}}{I_1 + I_2} \right) \left(\frac{I_{max} - I_{min}}{I_{max} + I_{min}} \right), \quad \Psi = \tan^{-1} \frac{S(D)}{C(D)}, \quad (2.11)$$

where y denotes the position of the interferogram, a denotes the half-weight of a slit, and f denotes the distance between the principal secondary point of the lens and interferogram. $S(D)$ and $C(D)$ are the sine and cosine components of the Fourier transform of the SR source distribution function. $\chi(D)$ in this equation represents an instrumental function of the interferometer; this term has a cosine-like dependence, and comes mainly from two sources: (1) A cosine term in the Fresnel-Kirchoff diffraction formula which represents the angular dependence between the incident and diffracted light of a single slit; (2) Reduction of effective slit height as double slit separation D_{SRM} increases.

The term χ is generally neglected in diffraction theory under the paraxial approximation, but we can not neglect this term in the practical use of the interferometer. We can measure the RMS beam size from one data visibility, which is measured at a fixed separation of the double slit. The RMS beam size σ_{beam} is given by [24],

$$\sigma_{beam} = \frac{\lambda F_{SRM}}{\pi D_{SRM}} \sqrt{\frac{1}{2} \ln \left(\frac{1}{\Gamma} \right)}, \quad (2.12)$$

where Γ denotes the visibility, which is measured at a double slit separation of D_{SRM} .

2.2.2 X-ray imaging

One obstacle to using the information carried by X-rays is the difficulty in imaging them. In contrast to ordinary light, the X-ray cannot be reflected promptly by mirrors or bent by lenses. An instrument that can be used is the single-pinhole camera, which consists only of a small hole in an otherwise opaque material through which an image is projected onto a piece of film. An image is formed because the small hole limits the view of any point onto the film to only one small part of the emitting source.

However, there are conflicting requirements for imaging with a single-pinhole camera. The hole should be small to provide resolution. However, a small hole often has an insufficient area to collect enough X-rays to produce an interpretable picture. This conflict between needing a small hole to obtain resolu-

tion and needing a large hole to obtain a sharp X-ray signal often limits the usefulness of the obtainable X-ray pinhole pictures. It is at this point that the capabilities of coded apertures become useful. Coded aperture techniques were first proposed in 1961 by Mertz and Young [27] that overcomes the conflicting requirements for imaging with a single pinhole camera. The detail design concept and reconstruction image of the coded aperture will be discussed in Chapters 3 and 6.

An XRM [13] with two types of optical elements (pinhole and coded aperture , CA [14]) is being developed for SuperKEKB. The aim is that eventually, it can provide a high-resolution bunch-by-bunch, turn-by-turn measurements for low-emittance tuning, collision tuning, and instability measurements. Each of the SuperKEKB rings has four straight-sections and four arc-sections. The X-ray sources are the final arc-sections, located immediately upstream of the straight-sections in Fuji (LER) and Oho (HER). The XRM installation images X-rays from a bending magnet through an optical element onto a detector. A schematic of the beamline is shown in Fig. 2.4 with the detail parameters will be explained in Chapter. 3.

After passing through an optical element, the X-rays from a point source form a diffraction pattern with single or multiple peaks on the detector depending on the pattern of the optical element. This pattern is the point spread function (PSF), i.e., the expected X-ray intensity distribution at the image plane for a given X-ray spectrum, beamline geometry, and optical element. Fresnel–Kirchhoff diffraction approximation is used to estimate the X-ray distribution from the source point to the detector. A brief introduction to diffraction theory will be discussed in the following subsections.

2.2.3 Fresnel–Kirchhoff Diffraction

The term *diffraction* has been conveniently defined by Sommerfeld [28] as "any deviation of light rays from rectilinear paths which cannot be interpreted as reflection or refraction." Consider system as shown in Fig. 2.5, consisting of closed surface S_1 and S_2 . S_1 lying directly behind the diffracting screen, be joined and closed by a large spherical cap, S_2 , of radius R and centered at the

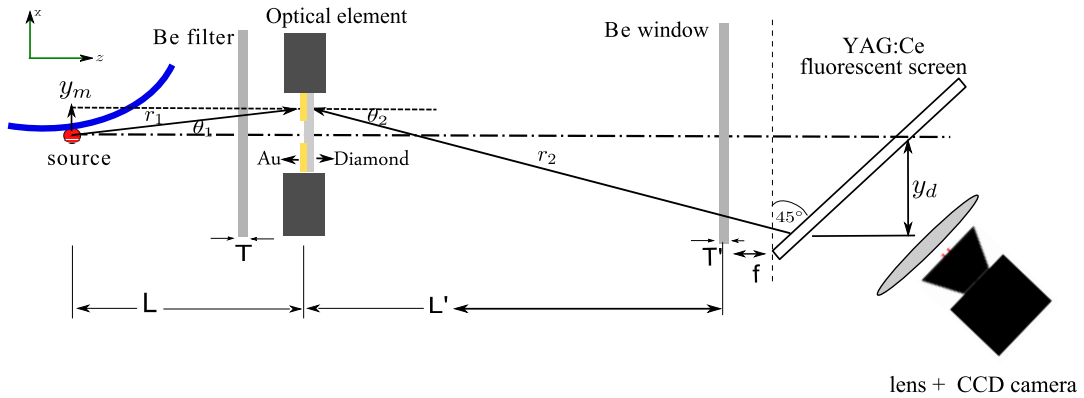


Figure 2.4: Schematic of the XRM beamline at each of the SuperKEKB rings (not to scale). It consists of a beryllium filter placed upstream of the optics to reduce the heat load, three sets of optical elements (a single pinhole and two sets of coded apertures), a beryllium window, and the detector system. For the Phase 1 (Phase 2) of SuperKEKB commissioning, a 141- μm -thick YAG:Ce (LuAG:Ce) scintillator with a CCD camera focused on it as the imaging system. The scintillator screen is tilted 45° in the horizontal plane, so that the camera and lens are out of the way beam. In the next phase, the scintillator will be supplemented by 128 channels of silicon detector with 2-mm sensing depth and a pixel pitch of $50\ \mu\text{m}$, for a single-shot measurement.

observation point P_0 . The total closed surface S is simply the sum of S_1 and S_2 . The diffracted disturbance $U(P_0)$ by incident disturbance U is defined as

$$\mathbf{U}(\mathbf{P}_0) = \frac{1}{4\pi} \iint_{\Sigma} \frac{\exp(ik\mathbf{r}_{01})}{\mathbf{r}_{01}} \left[\frac{\partial \mathbf{U}}{\partial \mathbf{n}} - ik\mathbf{U} \cos(\mathbf{n}, \mathbf{r}_{01}) \right] ds. \quad (2.13)$$

Now suppose that the aperture is illuminated by a single spherical wave $\mathbf{U}(P_1) = A \exp(ikr_{21})/r_{21}$ arising from a point source at P_2 , a distance r_{21} from P_1 as shown in Fig. 2.6 Then Eq. 2.13 can be directly reduced to [29]

$$\mathbf{U}(\mathbf{P}_0) = \frac{1}{4\pi} \iint_{\Sigma} \frac{\exp[ik(r_{21} + r_{01})]}{\mathbf{r}_{21}\mathbf{r}_{01}} \left[\frac{\cos(\mathbf{n}, \mathbf{r}_{01}) - \cos(\mathbf{n}, \mathbf{r}_{21})}{2} \right] ds. \quad (2.14)$$

This is commonly known as the Fresnel-Kirchhoff Diffraction formula.

2.2.4 Fraunhofer Approximation

Fraunhofer diffraction occurs when both the incident and diffraction waves are effectively planes waves. This will be the case when the distance from source

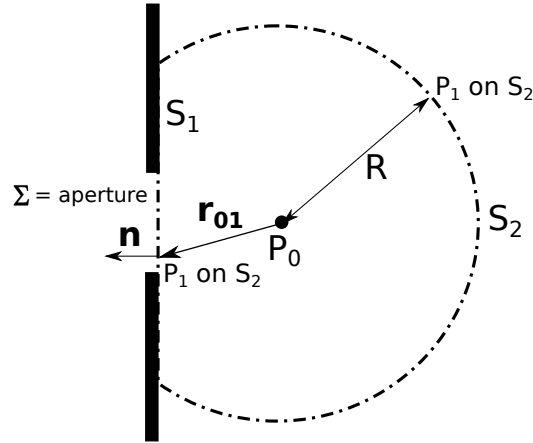


Figure 2.5: Kirchhoff formulation of diffraction by a plane screen.

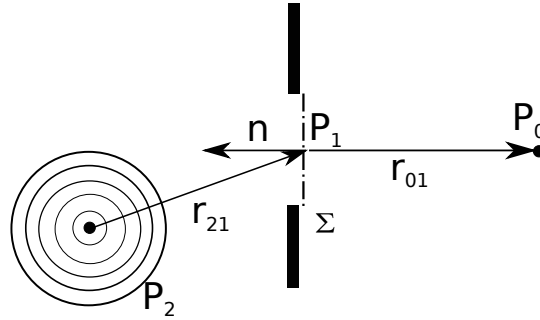


Figure 2.6: Kirchhoff formulation of diffraction by a plane screen.

to the diffracting pattern and from the aperture to the receiving points are both large enough. If we back to Fig. 2.6 and Eq. 2.14, several approximation are used for Fraunhofer diffraction:

1. The aperture is relatively small in this situation, therefore, $(n, r_{01}) \simeq (n, r_{21}) \simeq 0^\circ$, the obliquity factor $\frac{\cos(\mathbf{n}, \mathbf{r}_{01}) - \cos(\mathbf{n}, \mathbf{r}_{21})}{2} \simeq 1$.
2. The quantity $\frac{e^{-i\vec{k} \cdot \mathbf{r}_{01}'}}{r_{21}}$ is very nearly constant and can be taken outside the integral.
3. The variation of the remaining factor $\frac{e^{-i\vec{k} \cdot \mathbf{r}_{01}}}{r_{01}}$ over the aperture comes principally from the exponential part, so the factor $\frac{1}{r_{01}}$ can be replaced by its mean value and taken outside the integral. Also, \vec{k} and \vec{r}_{01} are nearly parallel with each other, so $\vec{k} \cdot \vec{r}_{01} \simeq kr_{01}$.

Consequently, the Fresnel-Kirchhoff formula reduces to the very simple equation for Fraunhofer diffraction, and is called the Fraunhofer diffraction formula,

$$U_{(P_0)} = C \iint_{\Sigma} e^{ikr_{01}} ds, \quad (2.15)$$

where all constant have been lumped into one constant C , where $C = \frac{i}{\lambda} E_0 e^{\frac{-ikr_{01}}{r_{01}r_{21}}}$. The formula above states that the distribution of the diffracted light is obtained simply by integrating the phase factor $e^{ikr_{01}}$ over the aperture.

Fraunhofer diffraction from a single slit

The case of diffraction by a single narrow slit is treated here as one-dimensional problem. Let the slit be of length L and of width b with an assumption of infinite some distance given plane wave at slit so that all amplitude elements are in phase. The element of area is then $ds = L dy$ as indicated in Fig. 2.7. Furthermore, we can express r as, $r = r_0 + y \sin \theta$. Where r_0 is the value of r

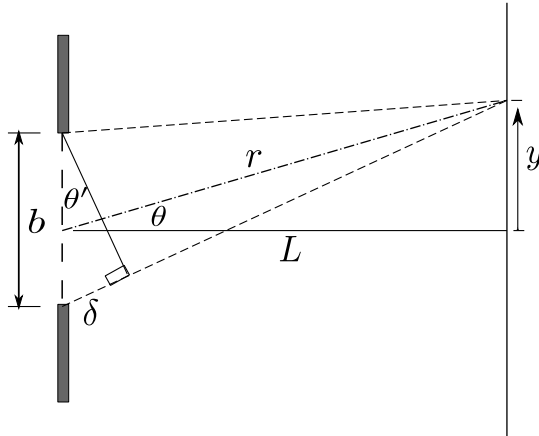


Figure 2.7: Fraunhofer diffraction on single slit.

for $y = 0$, and where θ is the angle shown, and for $L \gg b$ this approach $\theta' \approx \theta$.

The Fraunhofer diffraction formula yields

$$\begin{aligned}
 U_{(P_0)} &= C e^{ikr_0} \int_{-b/2}^{b/2} e^{iky \sin \theta} L \, dy \\
 &= \frac{CL e^{ikr_0}}{ik \sin \theta} \int_{-b/2}^{b/2} e^{iky \sin \theta} d(iky \sin \theta) \\
 &= CL b e^{ikr_0} \left[\frac{e^{i(kb \sin \theta/2)} - e^{-i(kb \sin \theta/2)}}{2i} \right] \cdot \left[\frac{1}{kb \sin \theta/2} \right] \\
 &= C' \left(\frac{\sin \beta}{\beta} \right), \tag{2.16}
 \end{aligned}$$

where $\beta = \frac{1}{2}kb \sin \theta$ and $C' = CL b e^{ikr_0}$ is just another constant. Thus $C' \left(\frac{\sin \beta}{\beta} \right)$ is the total amplitude of the light diffracted in a given direction defined by β . Then intensity (irradiance) distribution in the focal plane is given by the expression

$$I_s = I_0 \left(\frac{\sin \beta}{\beta} \right)^2, \tag{2.17}$$

where $I_0 = (CLb)^2$, which is the intensity for $\theta = 0$. The maximum value occurs at $\theta = 0$, and zero values occurs for $\beta = \pm\pi, \pm 2\pi \dots$. In general, the diffraction pattern of a single slit is shown in Fig. 2.8.

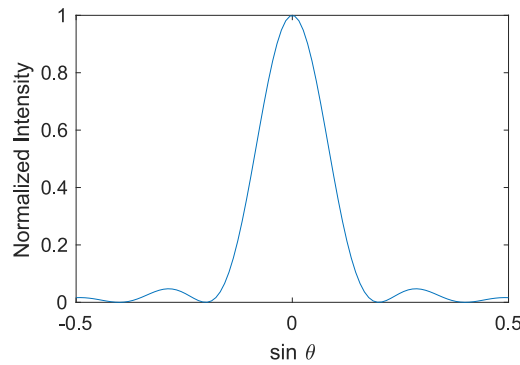


Figure 2.8: Fraunhofer diffraction pattern on single slit.

Fraunhofer diffraction from double slits

For the double slit, we can imagine that we place an obstruction in the middle of the single slit with the aperture schematic as shown in Fig. 2.9. Then

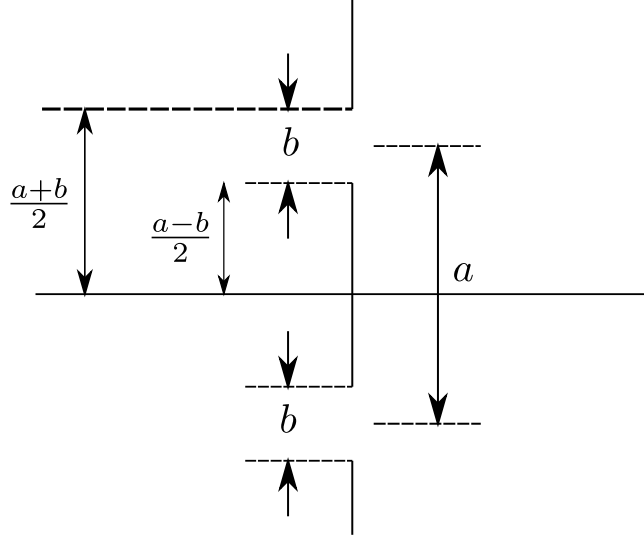


Figure 2.9: Schematic of double slit aperture.

the field from the double slit is calculated by summed up the single slit field with consider the limit of integration.

$$U_{(P_0)} = C e^{ikr_0} \int_{(a-b)/2}^{(a+b)/2} e^{iky \sin \theta} L dy + C e^{ikr_0} \int_{-(a+b)/2}^{-(a-b)/2} e^{iky \sin \theta} L dy. \quad (2.18)$$

Then by integrating and summed up all field, we have

$$U_{(P_0)} = C' \frac{(2 \cos \theta)(2i \sin \beta)}{2i\beta}. \quad (2.19)$$

Then intensity (irradiance) distribution in the focal plane is given by the expression

$$I_d = 4I_0 \cos^2 \theta \left(\frac{\sin \beta}{\beta} \right)^2. \quad (2.20)$$

The irradiance at point P_0 from double slit is given by the product of the diffraction pattern from single slit and interference pattern from a double slit

as shown in Fig. 2.10.

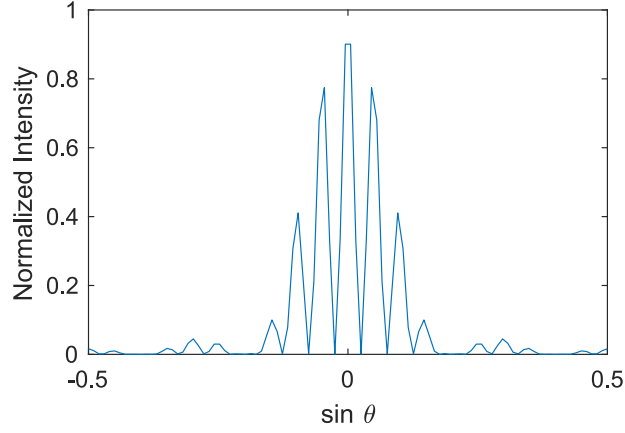


Figure 2.10: Fraunhofer diffraction pattern on double slit.

Fraunhofer diffraction from N slits (periodic width and space)

For the multiple slits we just need to again change the limits of integration. for N even slits with width b evenly spaced a distance a apart, we can place the origin of the coordinate system at the center obstruction and label the slits with the index j .

$$U_{(P_0)} = C e^{ikr_0} \sum_{j=1}^{j=N/2} \left\{ \int_{[(2j-1)a-b]/2}^{[(2j-1)a+b]/2} e^{iky \sin \theta} L dy + C e^{ikr_0} \int_{[-(2j-1)a-b]/2}^{[-(2j-1)a+b]/2} e^{iky \sin \theta} L dy \right\}. \quad (2.21)$$

With the same procedure as double slit, then intensity (irradiance) distribution in the focal plane is given by expression

$$I_m = N^2 I_0 \left(\frac{\sin \beta}{\beta} \right)^2 \left(\frac{\sin N\alpha}{\sin \alpha} \right)^2. \quad (2.22)$$

If we have N non-periodic slits that have different width and space, the same procedure is applied, we need to change the limit integration.

3 | X-Ray Beam Size Monitor

This chapter described the X-ray beam size monitor (XRM) in each SuperKEKB rings; the general XRM system, detector image simulation using point response function, optical element design, resolution, and apparatus of the XRM beamline.

3.1 General XRM System

The SuperKEKB rings have four straight-sections and four arc-sections. The X-ray sources are the final arc-sections, located immediately upstream of the straight-sections in Fuji (LER) and Oho (HER). The XRM installation images X-rays from a bending magnet through an optical element onto a detector. A schematic of the beamline is shown in Fig. 2.4.

3.2 Detector Image Simulation Using Point Response Function

After passing through an optical element, the X-rays from a point source form a diffraction pattern with an arrange of peaks on the detector depending on the pattern of the optical element. This pattern is the point spread function (PSF), i.e., the expected X-ray intensity distribution at the observation plane for a given X-ray spectrum, beamline geometry, and optical elements due to a mathematical 'point source'. We use a Fresnel–Kirchhoff diffraction approximation to estimate propagation of the X-ray distribution from the SR source

to the detector. For a one-dimensional mask as has been described in Fig. 2.4, the path integral in the vertical direction on the mask leads to

$$A_{\sigma,\pi(\text{detector})} = \frac{iA_{\sigma,\pi(\text{source})}}{\lambda} \int_{\text{mask}} \frac{t(y_m)}{r_1 r_2} e^{i\frac{2\pi}{\lambda}(r_1+r_2)} \left(\frac{\cos\theta_1 + \cos\theta_2}{2} \right) dy_m, \quad (3.1)$$

where $A_{\sigma,\pi(\text{source})}$ is the (angle-dependent) amplitude of the wave at the source point, λ is the wavelength, and y_m is the vertical coordinates at the mask. $\{r_1, \theta_1\}$ are the distance and angle from the source point to the mask point at y_m , and $\{r_2, \theta_2\}$ are the distance and angle from the mask point y_m to the detector point y_d , respectively. $t(y_m)$ is the complex transmission function at the mask point y_m . The complex transmission is represented as $t(y_m) = T(y_m)e^{i\delta(y_m)}$, where T is the real transmission and δ is the phase shift due to passing through the mask at y_m .

For each pixel in the detector, the wavefront amplitude from each source point is calculated and converted to the detected flux using Eqs. 2.7 and 3.1, respectively. The angular density of the spectral flux (number of radiated photons per unit time) at the detector is then defined as

$$\left[\frac{d^2 \mathcal{F}_\sigma}{d\theta d\psi} \right] = \alpha \frac{\Delta\omega}{\omega} \frac{I}{e} \left| \frac{iA_{\sigma,\pi(\text{source})}}{\lambda} \int_{\text{mask}} \frac{t(y_m)}{r_1 r_2} e^{i\frac{2\pi}{\lambda}(r_1+r_2)} \left(\frac{\cos\theta_1 + \cos\theta_2}{2} \right) dy_m \right|^2. \quad (3.2)$$

The synchrotron radiation field emission is incoherent, so the weighted flux contributions from all source points are then summed over the source distribution. This process is repeated over the detectable spectral range, taking into account the response properties of the detector. By varying the weighting of the Gaussian distribution source points and comparing the resulting (measured) image against the data templates, the Gaussian source profile can be reconstructed.

A large number of 1-dimensional templates corresponding to different values of the initial source parameters are pre-calculated, and the measured coded image is compared to each of the templates, searching for a ‘best-fit’ using a

least-squares method. The variable parameters for the pre-calculated templates include the beam size, normalization of the intensity, pedestal, offset of mask relative to the detector, and offset of the source relative to the detector. It takes one day to calculate a full set of detector images (PSFs), from which the template images are later constructed. Typically, some 1 million templates have been utilized for fitting images obtained at XRM, taking less than 10 minutes to generate. In the fitting process, the number of free parameters and their steps is generally limited to what we can process in 1 second.

At low intensities, the single-shot resolution of the system is limited by statistical fluctuations in the number of detected photons. To estimate the resolution as a function of beam size, simulated images are calculated for Gaussian beams of various sizes. The simulated detector images for different-sized beams are then compared pair-wise against each other, with one image in a pair representing a measured image for known beam size, and the other image representing a proposed model. The differences between the two images in signal heights for each detector channel are used to evaluate the χ^2 per degree of freedom v for this “fit” [30]

$$\frac{\chi^2}{v} = \frac{1}{N - n - 1} \sum_{i=1}^N \frac{[s_i' - s_i]^2}{\sigma_i^2}, \quad (3.3)$$

where N is the number of detector channels (pixels), and n is the number of fit parameters. The residual weighting σ_i for a channel is taken to be proportional to the square root of the signal height (number of photons) in that channel s_i ($\sigma_i = \sqrt{s_i}$). For a 128-pixel detector, the number of degrees of freedom v ($N - n - 1$) is then taken to be 126. The signal height in each channel is set to the number of expected number of photons detected in that channel for a given bunch intensity. More explicitly, the average number of photons per pixel at the detector is calculated, and the simulated image is normalized so that the average signal height is equal to n_p . Finally, the value of χ^2/v that corresponds to a confidence interval of 68% is chosen to represent the 1- σ confidence interval. The resolution is then defined as the change in the beam size, where the increment of $\chi^2/v = 1$. An example of χ^2/v map is shown in

Fig. 3.1.

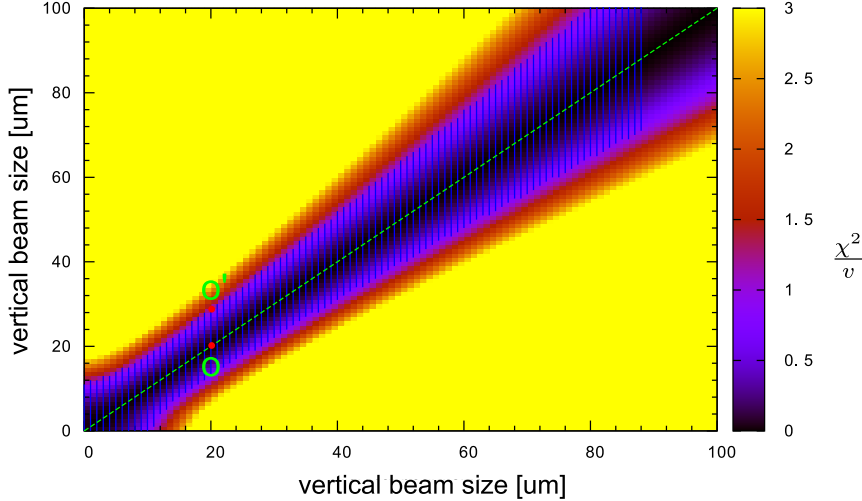


Figure 3.1: The resolution is defined where the increment of $\chi^2/v = 1$. A narrower χ^2/v distribution around the $y = x$ line (blue area), a better statistical resolution. The resolution chart can be calculated by comparing each beam size in x and y axes at $\Delta(\chi^2/v) = 1$, for example at 20 μm beam size, the resolution is a distance between O' and O.

3.3 Optical Element Design

As mentioned in Subsection 2.2.2, an optical element that can be used for the X-ray imaging is the single-pinhole camera, which consists only of a small hole in an otherwise opaque material through which an image is projected onto a piece of film. However, a small hole often has an insufficient area to collect enough X-rays to produce an interpretable picture. The capabilities of a coded aperture become useful to solve the pinhole limitation.

Two types of optical elements were used during the Phase 1 commissioning: a single pinhole and CAs (multi-slits and a Uniformly Redundant Array, URA [31]). Table 3.1 lists the parameters and specifications for each of the optical elements. CAs offer a greater open aperture than a single pinhole and better statistical resolution for single-shot measurements. The concept of CAs

is for a pseudo-random array of pinholes (apertures) to project a mosaic of pinhole images onto a detector. The detector image is then decoded using the known mask pattern to reconstruct the original image. Image reconstruction to estimate the beam size can be done by deconvolution (e.g., inverse Fourier transform or direct deconvolution), however the deconvolution of the 'coded aperture' to restore the original image is difficult. This difficulty is due to issues of dealing with background and detector noise, the diffraction effects, and also the non-uniform intensity profile of the incident beam. These effects are not accounted for in the direct reconstruction methods.

An alternative method of analyzing the coded aperture image is used in order to extract the beam parameters. Models/templates of the expected flux seen through the coded aperture are produced for several initial beam parameters. The measured X-ray flux at the detector is then compared to those templates (fitting method) as has been explained in Subsection 3.2. An example of a CA pattern is URA, which has been successfully tested for beam size measurements at CsrTA [32] and DLS [33]. In this section, we discuss the characteristics of each optical element and relevant design considerations. The optical elements in the XRM consist of 20- μm -thick gold masking material on 600- μm -thick diamond substrates. The diamond substrate mask is more robust than silicon because of better heat conduction providing better tolerance to the LER and HER power densities [34]. Subsections 3.3.1, 3.3.2 and 3.3.3 explain the pinhole and CA design procedures.

3.3.1 Optimizing the pinhole (single slit) size

The pinhole size is optimized by simulating detector images for a point source in both rings using various pinhole (slit) sizes with a trade-off diffraction effects and geometric smearing to achieve the best resolution. An example of detector image is shown in Fig. 3.2. Then the Gaussian distribution has been fitted to the simulated detector image to obtain the standard deviation. The minimum standard deviation of the resulting detector images was found to be 33 μm for LER and 30 μm for HER, as shown in Fig. 3.3. Eventually, we prefer to use an identical system with 33 μm as the optimum pinhole size for both

Table 3.1: Parameters of the optical elements for Phase 1 commissioning.

| Optical element | Parameter | Value |
|--|-------------------|-------------------|
| PH (pinhole) | width | 33 μm |
| Multi-slits | Diamond thickness | 600 μm |
| | Au thickness | 20 μm |
| | Number of slits | 17 |
| Pattern, S=slit, M=Au mask (μm) | | |
| 33S-22M-33S-66M-33S-22M-33S-110M-33S-22M-33S-44M-33S-22M-33S-198M-33S-22M-33S-44M-33S-22M-33S-66M-33S-22M-33S-44M-33S-22M-33S-110M-33S | | |
| URA | Diamond thickness | 600 μm |
| | Au thickness | 20 μm |
| | Number of slits | 12 |
| Pattern, S=slit, M=Au mask (μm) | | |
| 66S-33M-66S-99M-33S-33M-33S-33M-66S-132M-33S-165M-132S-33M-132S-66M-33S-33M-33S-33M-99S-66M-33S | | |

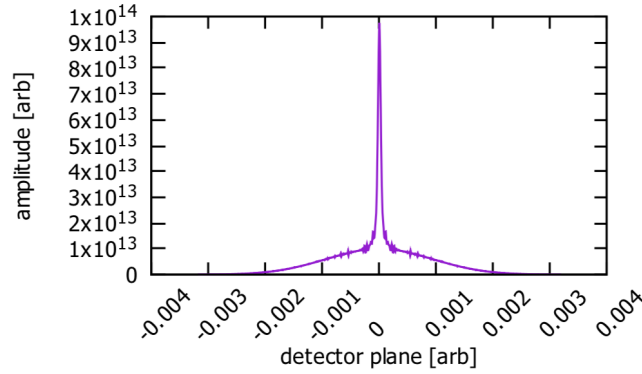


Figure 3.2: Expected X-ray intensity distribution at the detector (PSF pattern) for a point source in using a pinhole.

rings.

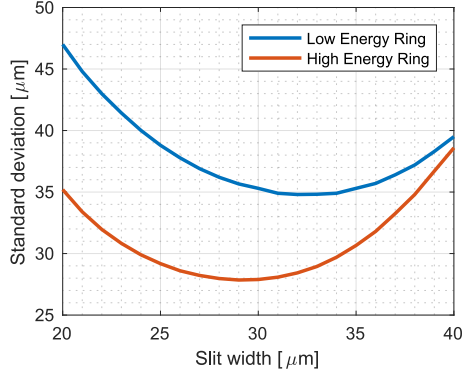


Figure 3.3: Standard deviation of images for various slit widths for LER and HER. The 33 μm slit size was taken as the optimum slit and basic size for both rings.

3.3.2 Design of the multi-slits coded aperture

Pairs of 33 μm slits were simulated with different separations between the pairs. For each separation, we calculated the resolution curves for different beam sizes using Eq. 3.3, as in Fig. 3.4, to determine the resolution of each range of beam sizes. We optimized the resolution at the smallest beam sizes, then used a large spacing to cover larger beam sizes. The 22 μm slit separation size was optimal for small beam sizes, so we used this for the design.

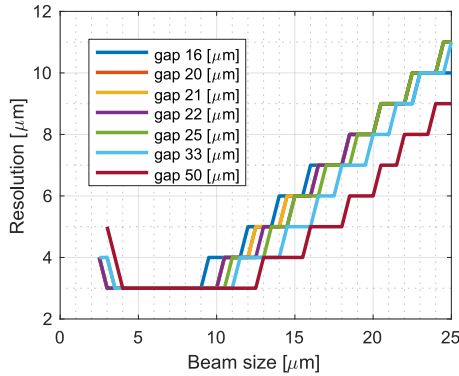


Figure 3.4: Pairs of 33 μm slits were simulated with different separations between the pairs (16, 20, 21, 22, 25, 33, and 50 μm). The 22 μm slit separation size is optimal for small beam sizes.

A series of multi-slit patterns were devised, using a suitable range of slit separations to cover the dynamics of interest. The example of expected X-

ray intensity distribution at detector (PSF pattern) for a point source using multi-slit aperture is shown in Fig 3.5.

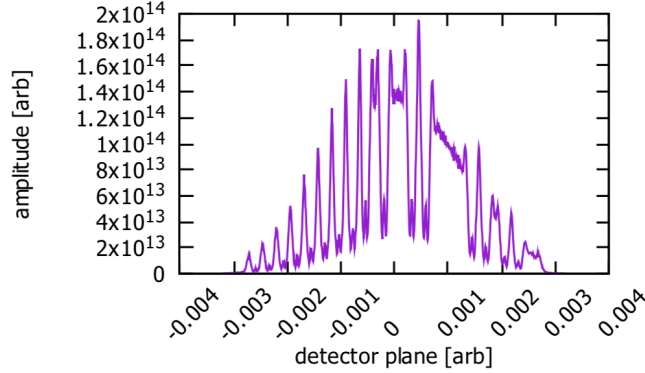


Figure 3.5: Expected X-ray intensity distribution at detector (PSF pattern) for a point source using 17 multi-slit.

Figure 3.6 shows some examples of the multi-slit patterns along with their resolutions, which were quantized into 0.5 μm step sizes. The resolution is defined as the change in beam size, where $\Delta(\chi^2/v)=1$ (see equation. 3.3), for a given number of photons. In general, more slits are better for photon statistics,

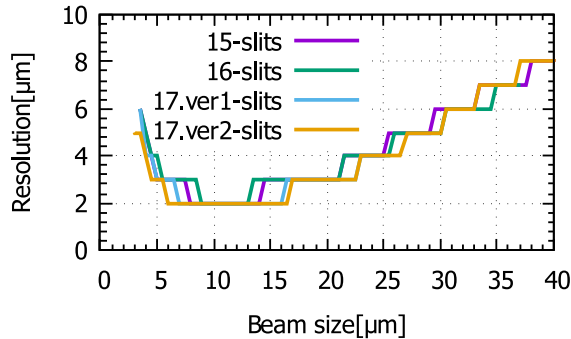


Figure 3.6: Series of multi-slit patterns with their resolutions. The spacing size for 15-, 16-, 17.ver1-, and 17.ver2-slits was 13151911319151, 131517191315171, 1213151272151311, and 1315121912131215, respectively. A spacing size of 1 means 22 μm , 2 means 44 μm , 3 means 66 μm , and so on. The 17.ver2-slits achieve better resolution than the others with the small beam sizes that we are interested in (<30 μm).

but large beam sizes require large slit separations to maintain the resolution. For aperture reasons, the mask pattern width in our XRM system should be

less than 2 mm. Thus, the best resolution was found to have 17 slits with the pattern has been listed in Table 3.1 and Fig. 3.7.

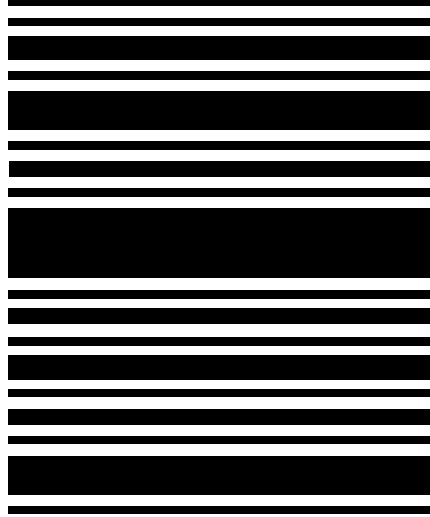


Figure 3.7: The multi-slit coded aperture pattern, consist of 17-slit with 33 μm and 22 μm as minimum slit and gap sizes, respectively. The holes occupied $\approx 40\%$ of the area.

3.3.3 Design of the URA coded aperture

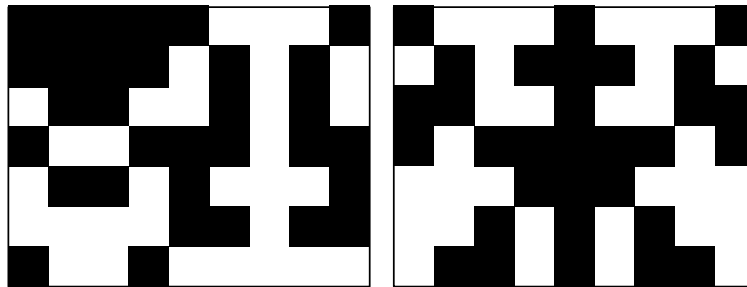
The uniformly redundant arrays URA mask patterns generated by the technique described by Fenimore and Cannon [31], are a particular case of coded aperture which be generated by cyclic difference sets. The basic patterns are generated in a one-dimensional string of n elements which regarded as 0 or 1, corresponding to transparent and opaque. A one-dimensional mask is generated from the n transparent or opaque bars as in Fig. 3.8. A two-dimensional mask is constructed by filling a rectangular array of p elements by q , where $p \cdot q = n$ with the elements of the one-dimensional string, p and q must be mutually prime, so for a two-dimensional mask the value of n chosen must have at least one pair of mutually prime factors. The elements are filled along an extended diagonal as shown in Fig. 3.9. In the XRM, we are using one-dimensional based 47 cyclic different set of the pattern as shown in Fig. 3.10 with 33 μm as a basic size. This pattern is $\sim 48\%$ occupied by holes that allow better photon statis-



Figure 3.8: A simple one-dimensional optimum-coded mask based on the modulo 15 cyclic difference set (0, 1, 2, 3, 7, 10, 11, 13). This figure is adapted from Ref. [35].

| | | | | | | | | |
|----|----|----|----|----|----|----|----|----|
| 0 | 28 | 56 | 21 | 49 | 14 | 42 | 7 | 35 |
| 36 | 1 | 29 | 57 | 22 | 50 | 15 | 43 | 8 |
| 9 | 37 | 2 | 30 | 58 | 23 | 51 | 16 | 44 |
| 45 | 10 | 38 | 3 | 31 | 59 | 24 | 52 | 17 |
| 18 | 46 | 11 | 39 | 4 | 32 | 60 | 25 | 53 |
| 54 | 19 | 47 | 12 | 40 | 5 | 33 | 61 | 26 |
| 27 | 55 | 20 | 48 | 13 | 41 | 6 | 34 | 62 |

(a)



(b)

(c)

Figure 3.9: A simple two-dimensional optimum-coded mask based on the modulo 63 cyclic difference set (0, 1, 2, 3, 4, 5, 11, 16, 17, 21, 23, 26, 27, 28, 29, 31, 35, 37, 40, 43, 45, 46, 48, 49, 50, 52, 53, 56, 57, 59, 61). (b) and (c) show two possible designs. This figure is adapted from Ref. [35].

tic than multi-slit coded aperture ($\sim 40\%$). The example of expected X-ray intensity distribution at detector (PRF pattern) for a point source using URA is shown in Fig. 3.11. In conclusion, they are three optical elements (masks) that are being used in the XRM. Figures 3.12 and 3.13 show the final patterns

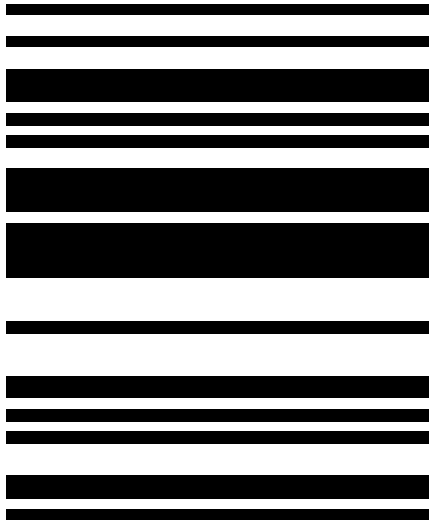


Figure 3.10: The URA pattern for XRM, based on the modulo 47 cyclic different set consist of 12-slit with $33\ \mu\text{m}$ and $22\ \mu\text{m}$ as the minimum slit and gap sizes, respectively. The holes occupied $\approx 48\%$ of the area

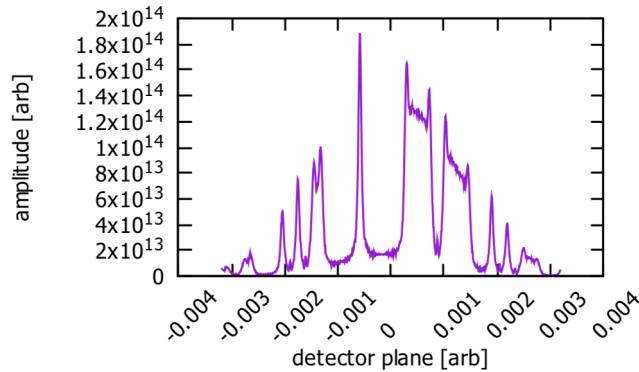


Figure 3.11: Expected X-ray intensity distribution at detector (PRF pattern) for a point source using 12-slit URA.

and a $1000\times$ magnification under Scanning Electron Microscope of all three optical elements. The mask consists of $20\text{-}\mu\text{m}$ -thick gold masking material on $600\text{-}\mu\text{m}$ -thick diamond substrates. The diamond substrate mask is more robust than silicon because of the better heat conduction, providing better tolerance to the LER and HER power densities [34].

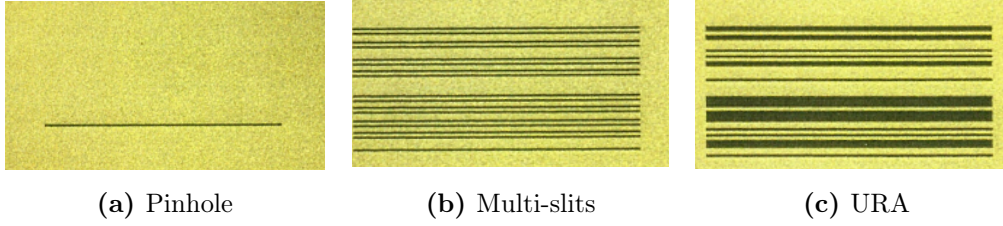


Figure 3.12: Mask pattern (pinhole, 17 multi-slits, and 12-slits URA) for both rings. The mask consists of 20- μm -thick gold masking material on 600- μm -thick diamond substrates.

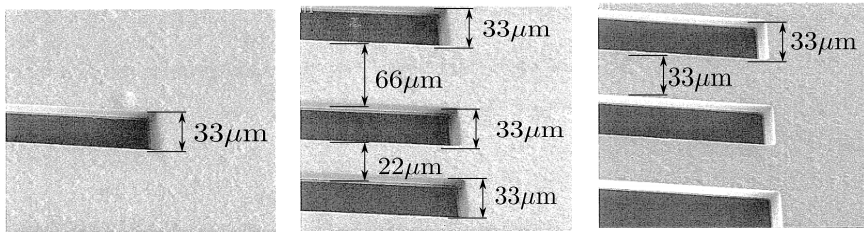


Figure 3.13: Three types of optical elements imaged using a 1000 \times Scanning Electron Microscope: (left) pinhole, (middle) multi-slits, and (right) URA.

3.4 Detector Image and Resolution

For the optical element design, a PSF image simulation was applied in an ideal condition without noise using 128 channels of silicon with 2 mm sensing depth and a pixel pitch of 50 μm (as a detector system that will be used for single-shot measurements). Figures 3.14 and 3.15 show simulated detector images for all mask patterns under ideal conditions from LER and HER with number of photons in LER and HER detectors are 1943 and 3342 photons/turn/mA/bunch, respectively. Equation 3.3 defines the resolution as the change in beam size where the increment of χ^2 per degree of freedom (χ^2/v) = 1, and Figs. 3.16, 3.17 show the contours of χ^2/v for both rings. A narrower distribution around the $y = x$ line, a better statistical resolution that we achieve. Fig. 3.18 represent the statistical resolution for all optical elements in both rings, calculated by comparing each beam size in x- and y-axes of Figs. 3.16, 3.17 at $\Delta(\chi^2/v) = 1$. The coded apertures show the superiority in resolution

compares to pinhole. The multi-slit elements are estimated to provide 2 – 3 μm resolution for 10 – 25 μm vertical beam sizes in both rings at 1 mA bunch current, as shown in Fig. 3.18. For larger beam sizes ($> 30 \mu\text{m}$), the 12-slits URA mask has better resolution than the 17 multi-slits.

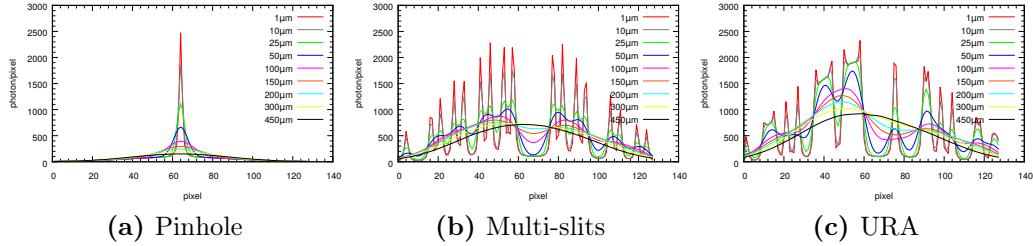


Figure 3.14: Simulated detector images showing the number of photons/pixel for single-pass 1 mA bunches for different beam sizes in LER. A series of detector image templates are generated for a range of beam sizes, and these are then compared with the data to find the closest match. (a) Pinhole mask, (b) multi-slits mask consisting of 17 peaks, and (c) URA mask consisting of 12 peaks. The number of peaks represents the number of slits that allow light to pass through.

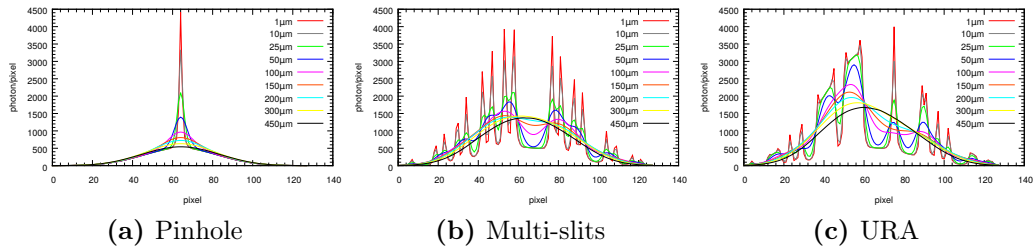


Figure 3.15: Simulated detector images showing the number of photons/pixel for single-pass 1 mA bunches for different beam sizes in HER. A series of detector image templates are generated for a range of beam sizes, and these are then compared with the data to find the closest match. (a) Pinhole mask, (b) multi-slits mask consisting of 17 peaks, and (c) URA mask consisting of 12 peaks. The number of peaks represents the number of slits that allow light to pass through.

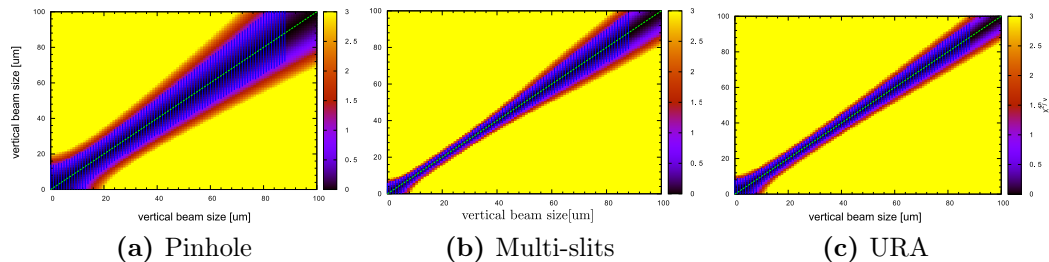


Figure 3.16: Calculated χ^2/v contours for each mask in LER at single-pass 1 mA bunch current. The x- and y-axes are the beam size, to get the resolution we compared it each other at the point where $(\Delta\chi^2/v) = 1$. A narrower χ^2/v distribution around the $y = x$ line, a better statistical resolution that we achieve. The coded apertures show the superiority in resolution compares to pinhole.

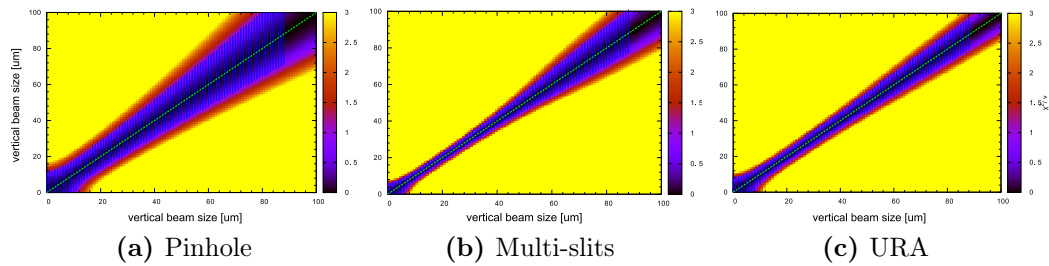


Figure 3.17: Calculated χ^2/v contours for each mask in HER at single-pass 1 mA bunch current. The x- and y-axes are the beam size, to get the resolution we compared it each other at the point where $(\Delta\chi^2/v) = 1$. A narrower χ^2/v distribution around the $y = x$ line, a better statistical resolution that we achieve. The coded apertures show the superiority in resolution compares to pinhole.

3.5 Apparatus

Two XRM diagnostic beamlines have been installed at SuperKEKB for electrons (HER) and for positrons (LER). These are identical, differing only in the distances from the source to the optics and from the optics to the detector, and the thickness of the beryllium filter (L , L' , and T , respectively, in Fig. 2.4), with the values given in Table 3.2. Each apparatus consists of three primary components: beamline, optical elements, and detector.

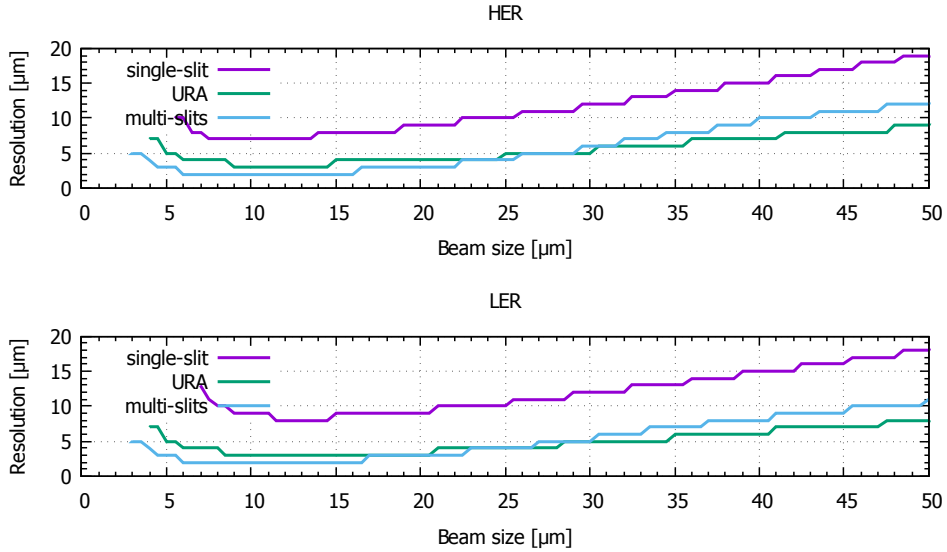


Figure 3.18: Single-bunch, single-turn vertical beam size resolutions for 1 mA bunch current in LER and HER for each optical element (pinhole, multi-slits, and URA) calculated by comparing each beam size in x- and y-axes of Figs. 3.16, 3.17 at $\chi^2/\nu = 1$. The 17 multi-slits is estimated to provide 2 – 3 μm resolution for 10 – 25 μm vertical beam sizes at 1 mA bunches. For larger beam sizes ($> 30 \mu\text{m}$), the 12-slits URA mask has better resolution than the 17 multi-slits.

3.5.1 Beamline

Figures 3.19, 3.20 [36], and Table 3.2 show the layout and parameters for each of the beamlines, respectively. In each case, the distance from the source point to the detector is ~ 40 m. The optical elements are placed in optics boxes $\sim 9 - 10$ meter from the source point, so that the geometrical magnification factor is $\sim 3\times$ for both lines. The beamlines are connected directly to the ring vacuum system. A gate valve is located upstream of the optics boxes for isolation during vacuum work downstream of the beamlines, or in the event of vacuum leaks. The X-rays from the upstream bending magnet go through the beryllium filter and optical elements, then propagate down the beamline toward the detector. Screen monitors are installed on the downstream ends of the beamlines, midway between the optic boxes and detector for beam-based alignment.

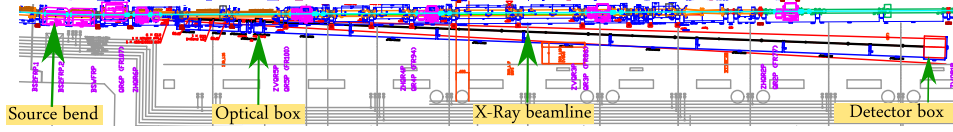


Figure 3.19: Location of XRM beamline for the LER in Fuji straight-section.

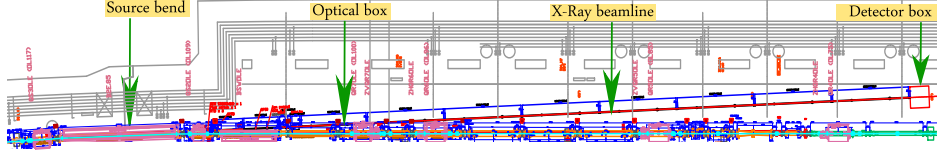


Figure 3.20: Location of XRM beamline for the HER in Oho straight-section.

Table 3.2: XRM beamline parameters.

| Parameter | | LER (e^+) | HER (e^-) | Unit |
|----------------------------------|--------|---------------|---------------|---------------|
| Radius of source bend | ρ | 31.85 | 105.98 | m |
| Distance from source to optic | L | 9.47 | 10.26 | m |
| Distance from optic to Be window | L' | 31.79 | 32.69 | m |
| Thickness of Be filter \otimes | T | 0.5 | 16 | mm |
| Thickness of Be window | T' | 0.2 | 0.2 | mm |
| Thickness of Au | | 20 | 20 | μm |
| Thickness of Diamond | | 600 | 600 | μm |
| Air gap | f | 100 | | mm |
| Effective thickness of YAG:Ce | | 141 | | μm |

The \otimes indicates value at Phase 1 of SuperKEKB commissioning.

3.5.2 Optical elements

A photograph of the coded aperture masks taken with a $1000\times$ Scanning Electron Microscope is shown in Fig. 3.13. Figure 3.21 shows the enclosed chamber for the optics, approximately 31.79 (32.69) m upstream of the detector

box and 9.47 (10.26) m downstream of the source point in LER (HER).

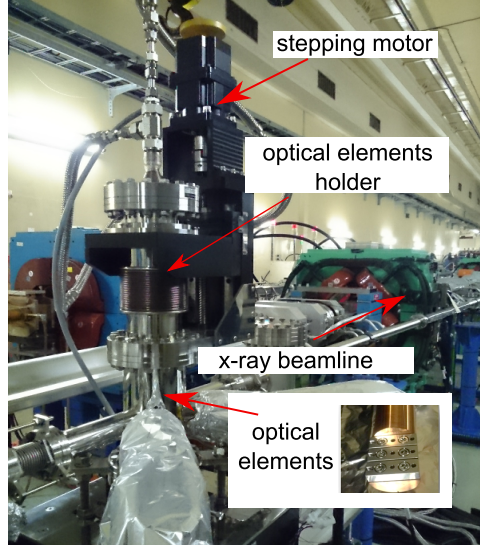


Figure 3.21: Optical system at Fuji straight-section (LER). The X-ray beam goes through the optical elements via a beryllium filter that is placed between the source point and optic box to reduce the heat load. The optical element is mounted on a stage controlled by a stepper motor that allows vertical motion.

3.5.3 Detector system: Scintillator, lens, camera

The longterm aim of XRM is for single-shot vertical beam size measurement using a Si detector and high-speed readout electronics, but the aim of Phase 1 is to benchmark the performance of the XRM in a multi-shot setup measurements using scintillator screen. The detector system is placed in a lead box, and incoming X-rays reach the scintillator through the beryllium window with the layout as shown in Fig. 3.22. For the Phase 1 commissioning of SuperKEKB, a cerium-doped yttrium-aluminum-garnet (YAG:Ce) scintillator was combined with a CCD camera for the X-ray imaging system, as shown in Fig. 3.23. The YAG:Ce has the maximum emission wavelength 550 nm, decay time 70 ns, and 4.55 g/cm^3 of density. The CCD ROX-40 was selected because of its high sensitivity (0.0005 lx) with peak around 500 nm, and $8.4 \mu\text{m} \times 9.8 \mu\text{m}$ pixel size.

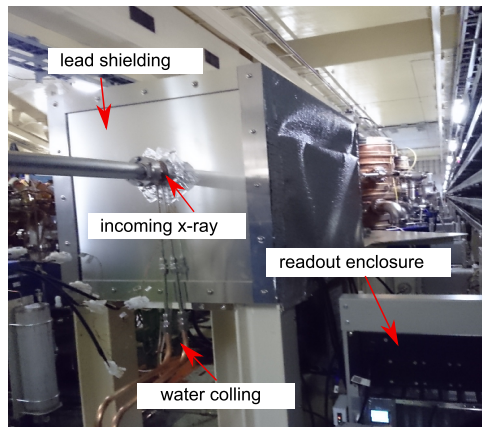


Figure 3.22: Detector system at Fuji straight-section (LER) for Phase 1 commissioning of SuperKEKB operation. The incoming X-rays go through to the scintillator via the Be window.

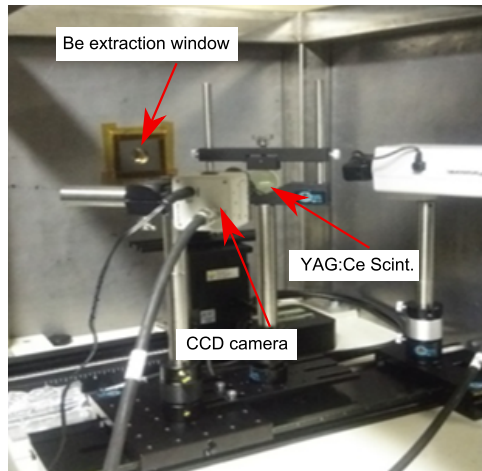


Figure 3.23: Detection system at Fuji straight-section (LER) for Phase 1 commissioning of SuperKEKB. Inside the detector box: Be extraction window and a 141- μm -thick YAG:Ce scintillator with CCD camera. The scintillator is tilted 45° in the horizontal plane, so that the camera and lens are out of the way beam. The camera and lens are also tilted 45° , so that they view the scintillator face-on. This does not effect the image in the vertical direction.

4 | Phase 1 of SuperKEKB Commissioning

The Phase 1 commissioning of SuperKEKB operations commenced in February 2016 and lasted approximately five months (until June 2016); the machine parameters are presented in Table 4.1 [8,12]. The display of the X-ray monitor in the control room for LER and HER rings is shown in Fig 4.1. An XRM was installed in each of the SuperKEKB rings, and several studies were carried out during the commissioning process.

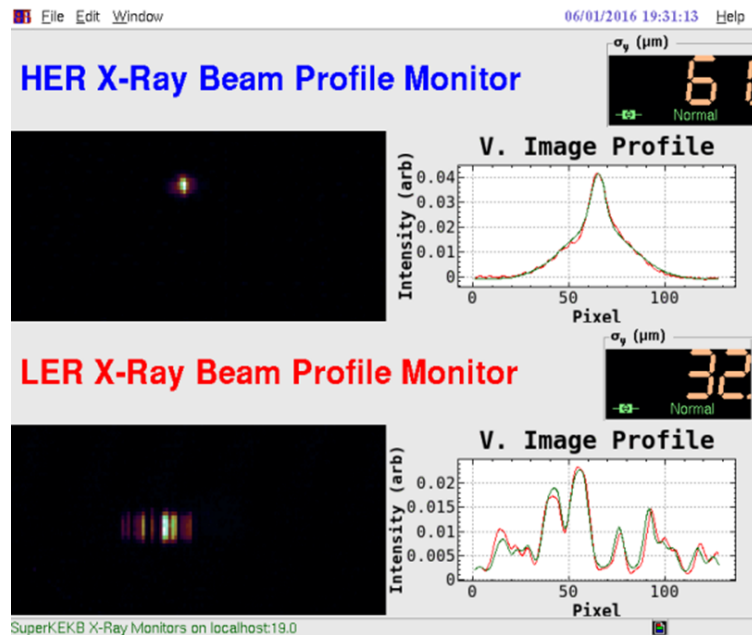


Figure 4.1: XRM panel in the control room, showing LER and HER vertical beam sizes.

Table 4.1: Machine parameters in Phase 1 commissioning of SuperKEKB Operation.

| Parameter | | LER (e^+) | HER (e^-) | Unit |
|---|-----------------|---------------|---------------|------|
| Beam energy | E_b | 4.000 | 7.007 | GeV |
| Max. beam current | I | 1.01 | 0.87 | A |
| Max. number of bunches | n_b | 2363 | 2455 | |
| Horizontal emittance (optic estimation) | ε_x | 1.8 | 4.6 | nm |
| Vertical emittance (optic estimation) | ε_x | 10 | 10 | pm |
| Bunch length | σ_z | 4.6 | 5.3 | mm |

4.1 Geometrical scale factors

Using beam-based measurements (see schematic in Fig. 4.2), the geometrical scale factors are measured by moving either the beam or the optical elements and observing how the peak features change. The ratio of geometric magnification from source-to-scintillator M and camera scale m can then be calculated. The camera scale m consists of the detector system (camera) magnification from scintillator-to-camera and the pixel size ($\mu\text{m}/\text{pixel}$).

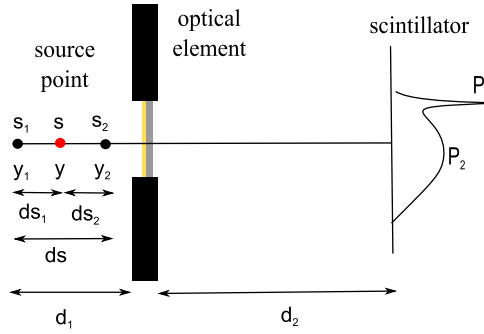


Figure 4.2: Schematic for the geometrical scale factors check, consisting of a source point with two beam position monitors (upstream s_1 and downstream s_2), optical elements, and a scintillator. P_1 is the position (in pixels) of a peak feature from X-rays that passed through a slit onto the scintillator and P_2 is the peak feature from X-rays transmitted through the Au mask.

When the beam is moved, the position (in pixels) of a peak feature from X-rays that passed through a slit onto the scintillator P_1 is defined as $P_1 = -\frac{M}{m}y$ with y is source point position. The correlation of y , vertical BPM value y_1, y_2 and distance between them based on schematic in Fig. 4.2 is defined as $y = y_1 + \frac{ds_1}{ds}(y_2 - y_1)$.

Then the P_1 is derived as

$$\begin{aligned}
P_1 &= -\frac{M}{m}\left(y_1 + \frac{ds_1}{ds}(y_2 - y_1)\right) \\
&= -\frac{M}{m}y_1 - \frac{M}{m}\frac{ds_1}{ds}(y_2 - y_1) \\
&= -\frac{M}{m}y_1 - \frac{M}{m}\frac{ds_1}{ds}y_2 + \frac{M}{m}\frac{ds_1}{ds}y_1 \\
&= \left(-\frac{M}{m}\left(1 - \frac{ds_1}{ds}\right)\right)y_1 - \frac{M}{m}\frac{ds_1}{ds}y_2, \tag{4.1}
\end{aligned}$$

where ds is the distance between downstream and upstream beam position monitors (BPMs), ds_1 is the distance from the upstream BPM to the source point, ds_2 is the distance from the downstream BPM to the source point, and y_1, y_2 are the readouts from the upstream and downstream BPMs, respectively.

When the optical element is moved, the ratio $(M + 1)/m$ is defined as

$$P_1 = \frac{M + 1}{m}y_{mask}, \tag{4.2}$$

where y_{mask} is the position of the optical element in μm . P_1 and P_2 were recorded during this study, and the ratio between M and m (geometrical scale factors) were calculated using Eqs. 4.1 and 4.2. We also evaluated the geometry scale through physical tape measure; the results are presented in Table 4.2. The geometrical magnification factors given by the tape- and beam-based measurements agreed within a few percent at both beam lines (see Table 4.3).

Table 4.2: Evaluation of geometry scale by tape measurement.

| Parameter | LER | HER | Unit |
|--------------------------------------|--------------------|--------------------|----------------------------|
| Distance from source to optics | 9.468 ± 0.005 | 10.261 ± 0.010 | m |
| Distance from optics to scintillator | 31.789 ± 0.005 | 32.689 ± 0.010 | m |
| Magnification (M) | 3.358 ± 0.002 | 3.186 ± 0.003 | |
| Scintillator camera scale (m) | 51.8 | 52.4 | $\mu\text{m}/\text{pixel}$ |

Table 4.3: Geometrical scale factors check for LER and HER using the ratio of geometrical magnification M and scintillator camera scale m . The ratios given by tape- and beam-based measurements are agreed within a few percent at both beam lines.

| | M/m | $(M+1)/m$ |
|------------------------------------|------------------|------------------|
| Tape measurement (pixels/mm) | | |
| LER | 66.27 ± 0.10 | 85.58 ± 0.10 |
| HER | 61.51 ± 0.10 | 80.59 ± 0.10 |
| Beam-based measurement (pixels/mm) | | |
| LER | 69.50 ± 0.50 | 86.00 ± 0.60 |
| HER | 59.20 ± 0.50 | 79.30 ± 0.10 |

4.2 Emittance control knob

In SuperKEKB there is a tool for enlarges the vertical beam size intentionally by making an asymmetric bump, called an "iSize" bump, at one of the strongest non-interleaved sextupole magnets in each SuperKEKB ring. A screenshot of emittance control knob 'ECK' measurement technique is shown in Fig. 4.3.

The ECK method [37] enlarges the beam size intentionally and measures the overall consistency factor between the reported beam size measurements and Structured Accelerator Design (SAD) simulation. The variation in the vertical beam size with respect to the bump height is defined as

$$(\sigma_{y_{meas}})^2 = (con \sigma_{y0})^2 + (con R)^2 (h - h_0)^2, \quad (4.3)$$

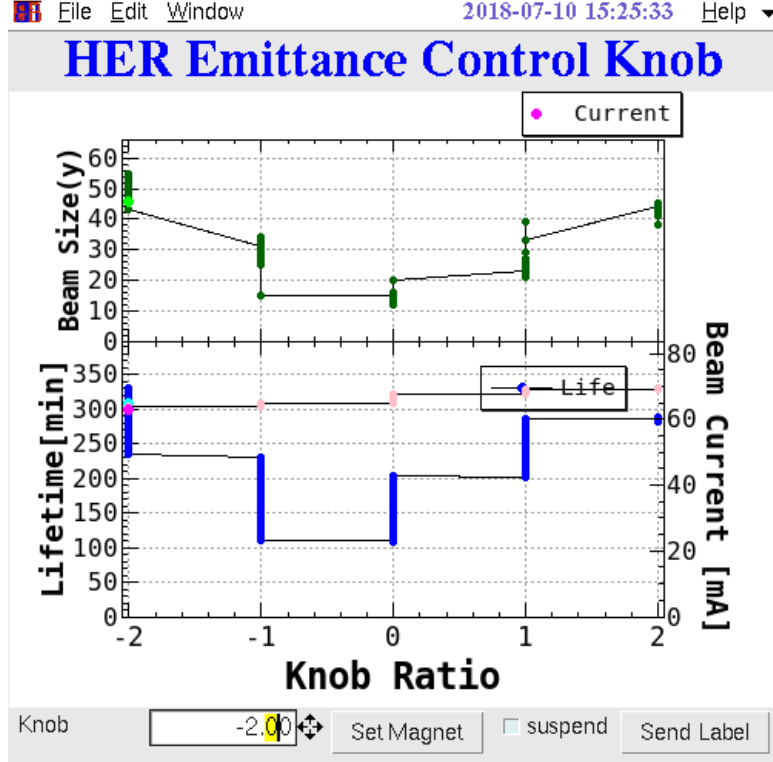


Figure 4.3: The emittance control knob 'ECK' measurement technique for HER, enlarging the vertical beam size intentionally by making an asymmetric bump.

where σ_{y0} and $\sigma_{y_{meas}}$ are the minimum vertical beam size and measured beam size, respectively. The relation between the vertical beam size σ_y , vertical emittance ε_y , and a vertical beta function β_y is given by

$$\sigma_y = \sqrt{\varepsilon_y \beta_y}. \quad (4.4)$$

The parameters h and h_0 are the bump height and its offset, con is the consistency factor, and R is a linear coefficient defined as

$$R^2 = \Delta\varepsilon_y \beta_{y,source} + (\eta_{y,source} \sigma_p)^2, \quad (4.5)$$

where $\Delta\varepsilon_y$ is the change in vertical emittance for a unit of bump-height squared as shown in Fig. 4.4, $\eta_{y,source}$ is the change in vertical dispersion for a unit of bump-height, and σ_p is the momentum spread. The beam parameters

$\Delta\varepsilon_y$, $\beta_{y,source}$, $\eta_{y,source}$, and σ_p are given by the optics model (as shown in Table 4.4).

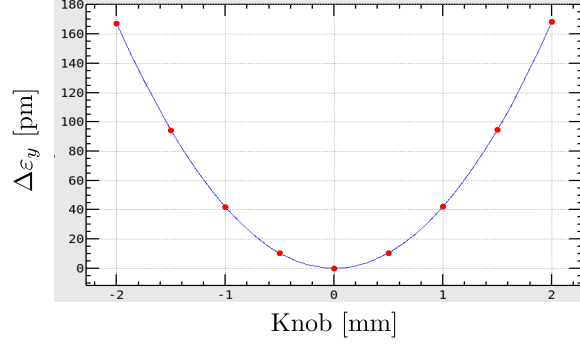


Figure 4.4: The $\Delta\varepsilon_y$ knob parameter as a change in vertical emittance for a unit of bump-height squared.

The results of this study for both beam lines are shown in Figs. 4.5, 4.6, and Table 4.5. The minimum measured beam size σ_{y0} and vertical emittance ε_y for LER (HER) are $\sim 30 \mu\text{m}$ ($\sim 35 \mu\text{m}$) and $\sim 13 \text{pm}$ ($\sim 160 \text{pm}$), respectively. The value of ε_y for LER is close to the design value given by the optical estimation $\sim 10 \text{pm}$. The measured value for HER is an order of magnitude higher than the design value. The PSF was studied using beam lifetime data to further investigate the discrepancy in both rings, as described in Subsection 4.3.

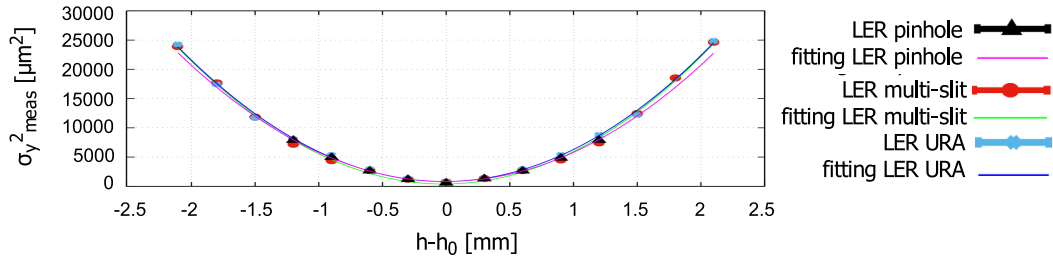


Figure 4.5: LER emittance control knob data for all optical elements at 200 mA beam current. Data points are fitted using the function in Eq. 4.3 with consistency factor (*con*) and minimum vertical beam size (σ_{y0}) as free parameters. Phase 1 design value $\varepsilon_y = 10 \text{pm}$, measured value $\varepsilon_y = 13 \text{pm}$.

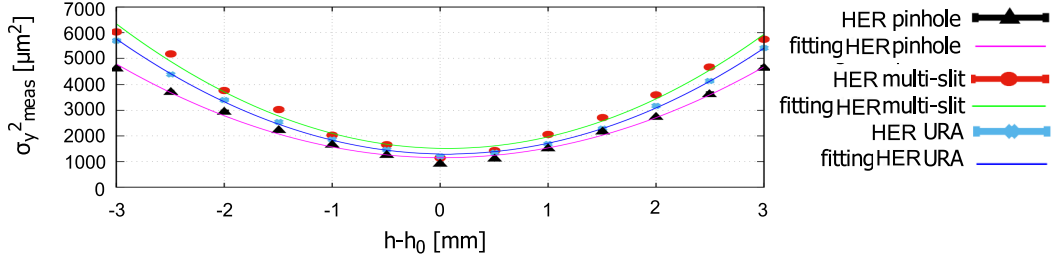


Figure 4.6: HER emittance control knob data for all optical elements at 190~195 mA beam current. Data points are fitted using the function in Eq. 4.3 with consistency factor (*con*) and minimum vertical beam size (σ_{y0}) as free parameters. Phase 1 design value $\varepsilon_y = 10$ pm, measured value $\varepsilon_y = 160$ pm.

Table 4.4: XRM beam parameter during Phase 1 measurement.

| Parameter | | LER | HER | Unit |
|---|-----------------------|----------------------|----------------------|-------------------------|
| Beam current | I | 188.7 – 200.7 | 208.1 – 258.6 | A |
| Beta function | $\beta_{y,source}$ | 67.4 | 7.6 | m |
| Vertical beam size (based on optics estimation) | $\sigma_{y,source}$ | ~ 25 | ~ 9 | μm |
| Change in vertical emittance per bump-height squared | $\Delta\varepsilon_y$ | 70.21 ± 0.03 | 42.19 ± 0.10 | pm/mm^2 |
| Change in vertical dispersion per bump-height | $\eta_{y,source}$ | 0.056 | 0.017 | m/mm |
| Momentum spread | σ_p | 7.7×10^{-4} | 6.3×10^{-4} | |
| Bunch length | $\sigma_z(I_b)$ | $4.58 + 0.59I_b$ | $5.34 + 0.88I_b$ | mm |
| Number of bunches/ring | n_b | 1576 | 1576 | |

4.3 Beam lifetime technique

The beam lifetime, which was recorded during the emittance control knob studies, was used to study the PSF. A bunch of charged particles (electrons/positrons) in a ring decays due to the quantum lifetime (emission of SR), Coulomb scattering (elastic and inelastic scattering on residual gas atoms), bremsstrahlung (photon emission induced by residual gas atoms), and the Touschek effect (electron–electron scattering). None of these mechanisms is related to beam

Table 4.5: Results of the emittance control knob method. From this data, the value of ε_y for LER (HER) is found to be ~ 13 pm (~ 160 pm). This is close to the design value for LER, but much higher for HER, indicating the possibility of a spread function. The PSF was studied using beam lifetime data and the consistency factor *con* to investigate this discrepancy.

| Mask | $\sigma_{y0}(\mu\text{m})$ | Consistency factor (<i>con</i>) |
|-------------|----------------------------|-----------------------------------|
| LER | | |
| pinhole | 28.80 ± 1.01 | 0.92 ± 0.02 |
| multi-slits | 32.50 ± 1.51 | 0.86 ± 0.02 |
| URA | 30.07 ± 0.98 | 0.94 ± 0.01 |
| HER | | |
| pinhole | 33.60 ± 0.78 | 1.01 ± 0.02 |
| multi-slits | 37.06 ± 0.83 | 1.12 ± 0.02 |
| URA | 36.83 ± 0.72 | 1.02 ± 0.01 |

size except for Touschek effect.

During the phase 1 commissioning, the lifetime was dominated by Touschek scattering [38] as shown in Fig 4.7. Touschek collisions transfer momentum from transverse to longitudinal motion, and both electrons can slip outside the range of longitudinal acceptance, in which case they are lost.

Piwinski [39], Khan [40], and Carmignani [41] express the loss rate as

$$\frac{1}{\tau} = \left\langle \frac{c r_e^2 n_p}{8\pi\gamma^2 \sigma_z (\Delta p/p)^3 \sqrt{\sigma_x^2 \sigma_y^2 - \sigma_p^4 D_x^2 D_y^2}} F(\xi) \right\rangle, \quad (4.6)$$

where τ is the Touschek lifetime, n_p is the number of particles, D is dispersion, σ_p is the relative momentum spread, $\Delta p/p$ is the momentum acceptance, $F(\xi)$ is the Touschek factor, and $\langle \rangle$ denotes an average over the whole circumference of the storage ring. For a flat beam with a very small vertical oscillations ($D_y = 0$), Khan [40] derived the loss rate as

$$\frac{1}{\tau} = \left\langle \frac{c r_e^2 n_p}{8\pi\gamma^2 \sigma_z \sigma_x \sigma_y (\Delta p/p)^3} F(\xi) \right\rangle. \quad (4.7)$$

In our analysis, we considered the beam parameters σ_x , $\Delta p/p$, and $F(\xi)$

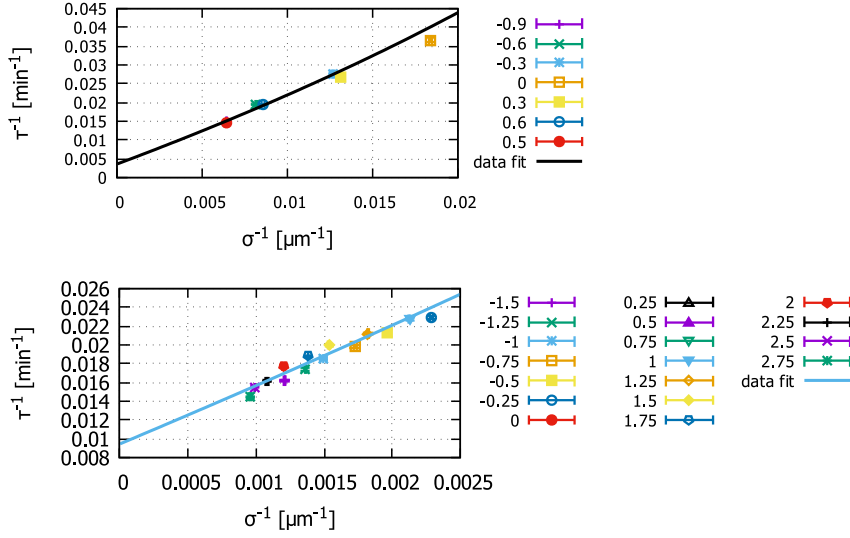


Figure 4.7: Relation between lifetime and measured beam size for LER (left) and HER (right). By fitting $1/T$ vs $1/\sigma_y$ via linear function $1/T = \alpha_1 (1/(\sigma_y/cal)) + b$, with $\sigma_y = \sqrt{\sigma_{meas}^2 - \sigma_{psf}^2}$. A small value of b , representing non-Touschek lifetime sources.

to be constant, which implies that the Touschek lifetime is proportional to σ_z/I_b and the vertical beam size σ_y . The bunch current I_b decreased during the measurements (see Table 4.4) and as the bunch length σ_z is a function of I_b [42], we should consider this correction in the analysis. The measured value $\sigma_{y_{meas}}$ will be larger than the actual beam size σ_y because of the PSF. If σ_y is convolved with a Gaussian smearing function of size σ_s , then $\sigma_{y_{meas}}^2 = (\sigma_y^2 + \sigma_s^2) con^2$, where con is the consistency factor from the emittance control knob method. The Touschek lifetime can then be represented as

$$\tau = \left\langle k \frac{\sigma_z}{I_b} \sigma_y \right\rangle = \left\langle k \frac{\sigma_z}{I_b} \sqrt{\frac{\sigma_{y_{meas}}^2}{con^2} - \sigma_s^2} \right\rangle. \quad (4.8)$$

Fitting the lifetime using the bunch length correction, i.e., $\tau I_b/\sigma_z$ vs $\sigma_{y_{meas}}$ data using Eq. 4.8 with k and σ_s as free parameters, gives results shown in Figs. 4.8 and 4.9.

Using the correlation between the vertical beam size σ_y , beta function β_y , and emittance ε_y given by Eq. 4.4 and the parameters in Table 4.4, we can

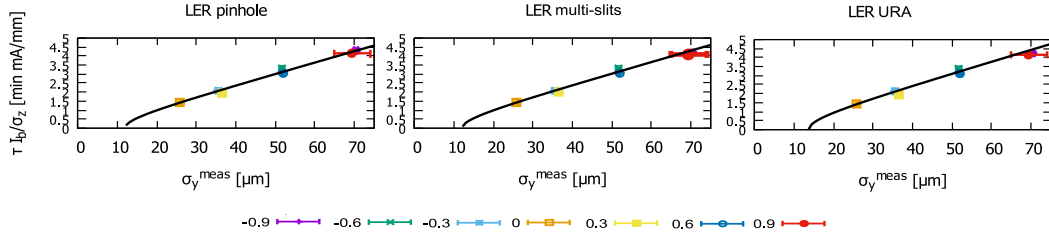


Figure 4.8: Relation between lifetime and measured beam size for LER with bunch length correction for each bump height, fitted using Eq. 4.8 to obtain the PSF factor σ_s .

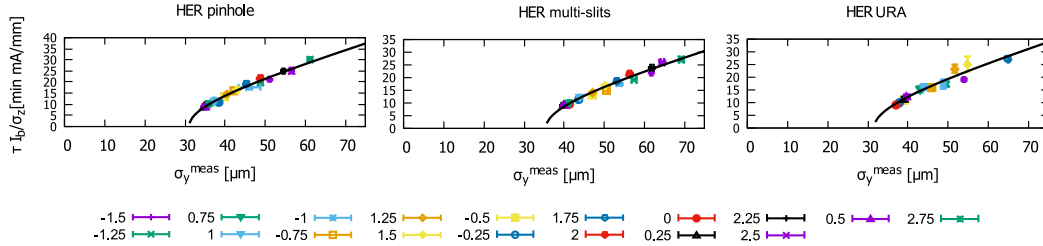


Figure 4.9: Relation between lifetime and measured beam size for HER with bunch length correction for each bump height, fitted using Eq. 4.8 to obtain the PSF factor σ_s .

calculate a minimum vertical beam size σ_{y0} from the smallest measured beam size $\sigma_{y_{meas}}$, which corresponds to the minimum vertical emittance ε_{y0} . The averaged values of σ_s , σ_{y0} , and ε_{y0} over all measurements made with the three optical elements are given in Table 4.6.

Table 4.6: Average of PSF σ_s , minimum vertical beam size σ_{y0} as fitting results of Figures 4.8 and 4.9, and vertical emittance ε_{y0} measured with all three optical elements.

| | LER | HER | Unit |
|--------------------|------------------|------------------|---------------|
| σ_s | 15.63 ± 2.90 | 31.58 ± 0.72 | μm |
| σ_{y0} | 21.56 ± 2.91 | 16.93 ± 0.74 | μm |
| ε_{y0} | ~ 10 | ~ 35 | pm |

The LER vertical emittance ε_y is consistent with the optics estimation (~ 10 pm), but for HER, the emittance is $3.5\times$ the optics estimate (~ 35 pm). These results indicate unknown sources that make our measurement in HER

bigger than optics estimation.

4.4 Spatial resolution of the detector system

Regarding the detector, several parameters affect the spatial resolution: focus defects, diffraction effects, and spherical aberrations [43]. The relationships between the spatial resolution R_f and the scintillator depth dz (141 μm), numerical aperture of the camera NA (0.03132), XRM magnification M (3.2), and wavelength of visible light from the scintillator λ (550 nm) are

$$R_f \sim \frac{dzNA}{M}, \text{ defect of focus } \sim 1.4 \mu\text{m}, \quad (4.9)$$

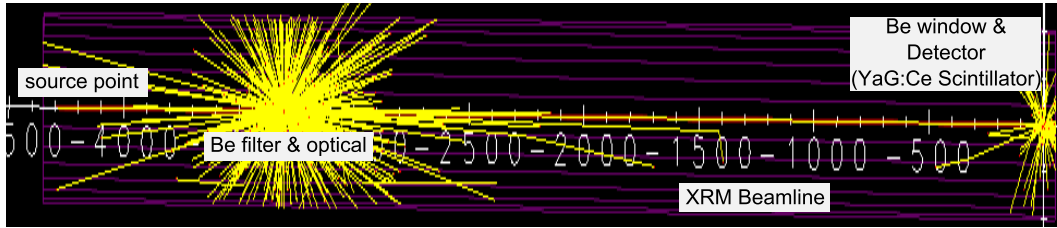
$$R_f \sim \frac{\lambda}{MNA}, \text{ diffraction effect } \sim 5.5 \mu\text{m}, \quad (4.10)$$

$$R_f \sim \frac{dz(NA)^2}{M}, \text{ spherical aberration } \sim 1 \mu\text{m}. \quad (4.11)$$

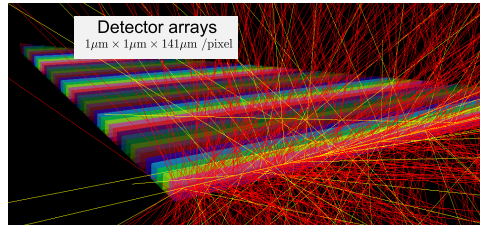
The effects contribute $\sim 5.8 \mu\text{m}$ of smearing at the source point. Additionally, the resolution of the detector can be limited by the spatial distribution of the deposited energy imparted from ionizing radiation. This distribution is affected by scattered X-rays or secondary electrons that may deposit energy far away from the primary photon interaction site. The EGS5 (Electron-Gamma-Shower) code [44] is a general-purpose package for conducting Monte Carlo simulations of the coupled transport of electrons and photons in an arbitrary geometry for particles with energy from a few keV to several hundred GeV. In our case, EGS5 calculated the absorbed dose of an X-ray pencil beam passing through the Be filter, optical elements, Be window, and onto the flat surface of the 141- μm -thick YAG:Ce scintillator. Further analysis attempted to determine the effect of scattering anywhere in the beamline or detector of the imaging system.

We calculated the absorbed dose of 6 – 50 keV X-ray pencil beams from the source point to the YAG:Ce scintillator. The parameters applied in the

EGS5 simulation were: sampling of angular distributions of photoelectrons in various regions, explicit treatment of K- and L-edge fluorescent photons, explicit treatment of K and L Auger electrons, coherent (Rayleigh) scattering in various media, linearly polarized photon scattering in all regions, incoherent scattering function for Compton scattering angles in all regions, and doppler broadening of Compton scattering energies. A view of the XRM beamline given by the EGS5 simulation is shown in Fig. 4.10; the X-rays passed through the Be filter (some photons were scattered and their energy deposited on the Be filter), then reached the scintillator via the Be window. The EGS5 calculation results in Fig. 4.11, The peak spectrum energy for LER and HER is estimated to be 11 keV and 18 keV, respectively. The scattering range is $<1 \mu\text{m}$ with a background/peak ratio of $\approx 10^{-4}$.



(a) CGView of XRM beamline given by EGS simulation.



(b) Detector arrays.

Figure 4.10: EGS5 simulation results: (a) X-ray pencil beam from source point passed through the Be filter, optical element, Be window, and onto the YAG:Ce scintillator; (b) Detector (YAG:Ce) pixel arrays, which consist of 50 arrays ($1 \mu\text{m} \times 1 \mu\text{m} \times 141 \mu\text{m}$ for each detector pixel). Yellow and red lines represent photons and electrons, respectively.

Altogether, the contribution from focus defects, diffraction effects, spherical aberrations, and scattering effects is $\approx 6 \mu\text{m}$ at the source point. This cannot account for the smearing observed in the lifetime studies. Other possible sources

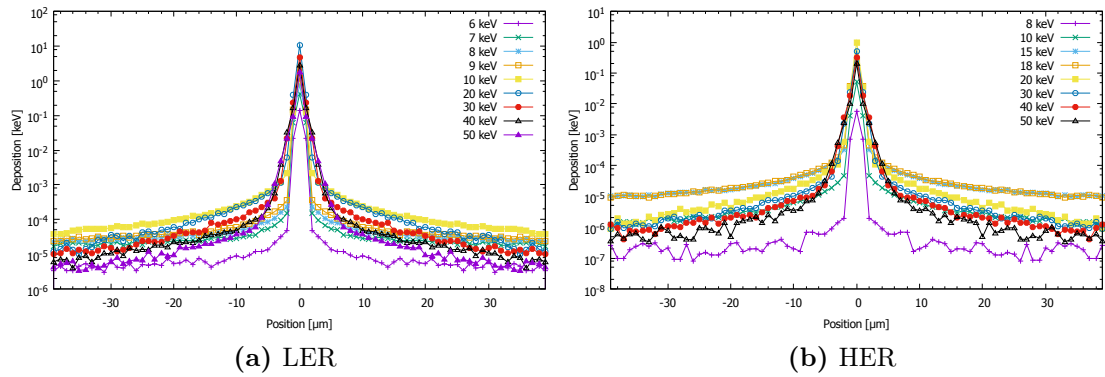


Figure 4.11: Deposited energy in YAG:Ce for given X-ray energy: (a) LER and (b) HER.

of smearing or resolution loss include beam tilt or motion, camera misfocus, or some source of scattering not simulated by EGS5 (small angle scattering), such as impurities or inhomogeneities in the Be filters. For the Phase 2 commissioning, new optical elements were installed for XRM, and we have replaced the Be filters with thinner ones.

5 | Phase 2 of SuperKEKB Commissioning

Continuing studies were made during the Phase 2 (May – July 2018) with the purpose to reduce the PSF that we found in Phase 1 (especially in the HER beamline).

5.1 Strategy in Phase 2

Several new types of equipment have been installed in the HER beamline: thinner Be filters, optical elements that have been re-optimized, LUAG:Ce scintillator screen, and CCD camera.

5.1.1 Thinner Be filter

The functions of a Be filter in the XRM system are to separate the vacuum between the X-ray extraction chamber and XRM beamline, and to reduce the X-ray power density. In Phase 1, a 16 mm of Be was added in the HER XRM system to increase the margin of safety regarding the heat load [34]. The Phase 1 XRM systematics study suggested the PSF made the beam size bigger than the optic estimation. The Be filter was considered one of the sources because of the possibility of X-ray diffraction on it, e.g., a small-angle scattering mainly due to density fluctuation or poly-crystal structure [45]. The example of the X-ray diffraction pattern from Be window is shown in Fig. 5.1, they have strong Deby-Sherer and small-angle scattering mainly due to density fluctuation or

poly-crystal structure [45]. For that reason, we have replaced the Be filter in

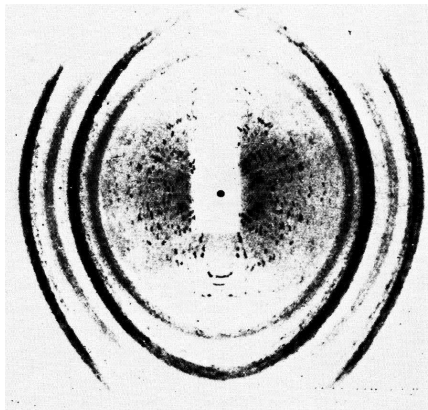


Figure 5.1: Powder pattern obtained from a beryllium window (Air product and Chemicals, 1973) [45].

HER with the thinner ones, from 16 mm to 0.2 mm which is the same thickness as Be window.

5.1.2 Optimizing the pinhole size

The pinhole size is optimized by simulating detector image for a point source in both rings using various pinhole (slit) sizes. The procedure is as same as the Phase 1, differing only in the diamond thickness (800 μm) and Be filter thickness. The minimum standard deviations of resulting PSFs were found to be 33 μm for LER and 31 μm for HER as shown in Fig. 5.2. We took 31 μm as the new minimum slit size for HER and kept 33 μm as the minimum slit sizes for LER. The same optical element patterns as in Phase 1 are then rescaled with 31 μm as the minimum slit size. The detail parameter and pattern of the optical elements for Phase 2 commissioning in HER are listed in Table. 5.1.

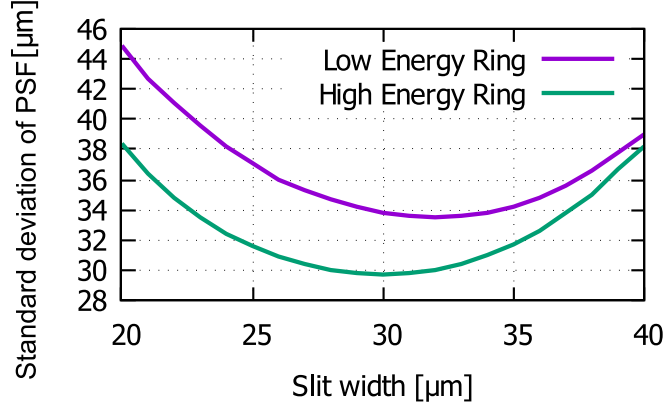


Figure 5.2: Standard deviation of images for various slit widths for LER and HER in Phase 2. The 33 μm (31 μm) slit size was taken as the optimum slit and basic size for LER (HER) ring.

Table 5.1: Parameters of the optical elements for Phase 2 commissioning for HER ring.

| Optical element | Parameter | Value |
|--|-------------------|-------------------|
| PH (pinhole) | width | 31 μm |
| Multi-slits | Diamond thickness | 800 μm |
| | Au thickness | 20 μm |
| | Number of slits | 17 |
| Pattern, S=slit, M=Au mask (μm) | | |
| 31S-21M-31S-62M-31S-21M-31S-103M-31S-21M-31S-41M-31S-21M-31S-186M-31S-21M-31S-41M-31S-21M-31S-62M-31S-21M-31S-41M-31S-21M-31S-103M-31S | | |
| URA | Diamond thickness | 800 μm |
| | Au thickness | 20 μm |
| | Number of slits | 12 |
| Pattern, S=slit, M=Au mask (μm) | | |
| 62S-31M-62S-93M-31S-31M-31S-31M-62S-124M-31S-155M-124S-31M-124S-62M-31S-31M-31S-31M-93S-62M-31S | | |

5.2 Scintillator, lens, and camera system

5.2.1 LuAG:Ce Scintillator

59

We then replaced the YAG:Ce with LuAG:Ce to improve the spatial resolution. A comparison between YAG:Ce and LuAG:Ce for X-ray imaging was

observed [46]. The LuAG:Ce single crystal is denser compared to YAG:Ce (6.76 and 4.55 gram/cm³, respectively), and the X-rays are absorbed stronger by LuAG. 1.7 times more X-ray radiation is absorbed in the range between 1 and 40 keV, as calculated using X-ray radiation attenuation coefficients. The LuAG:Ce screen has higher conversion efficiency than YAG:Ce screen, so that the signal-to-noise ratio of the image is better for use in the imaging system. Another X-ray imaging system with a YAG:Ce screen has been demonstrated successfully for vertical beam size measurement in Diamond Light Source, DLC [47].

5.2.2 Lens and camera system

Pentax C1614A lenses [48] were used for both rings with 16.0 mm of focal length, 1:1.4 maximum aperture ratio, 0.3 m minimum object distance, and 58 gram weight. The distance between lens and scintillator is 5 cm, so the extension tube set (macro ring) [48] was inserted between the lens and camera to shift the focal point further than the mechanical limit of the lens for the close-up application. The extender that we used is shown in Fig. 5.4.

We also used an acA2440-20gm-Basler ace CCD camera [49] with 2448 × 2048 pixel grayscale resolution, 3.45 μm × 3.45 μm pixel size and 23 fps of frame rate. The exposure time was set to 800 μs to not saturate the white balance at ~ 700 mA beam current.

5.3 Study results

The primary goal in Phase 2 is to reduce the PSF that we found in the HER during the Phase 1. The display of the X-ray monitor in the control room for HER and LER rings is shown in Fig. 5.6, showing the vertical and horizontal beam sizes (we will only discuss the vertical beam size measurements). The emittance control knob used in Phase 1 was repeated to check the consistency between the measured beam size and SAD simulation. The beam parameters and the ECK results during Phase 2 are shown in Table. 5.2 and Fig. 5.7, respectively. The bunch length correction also taken into account in the life-

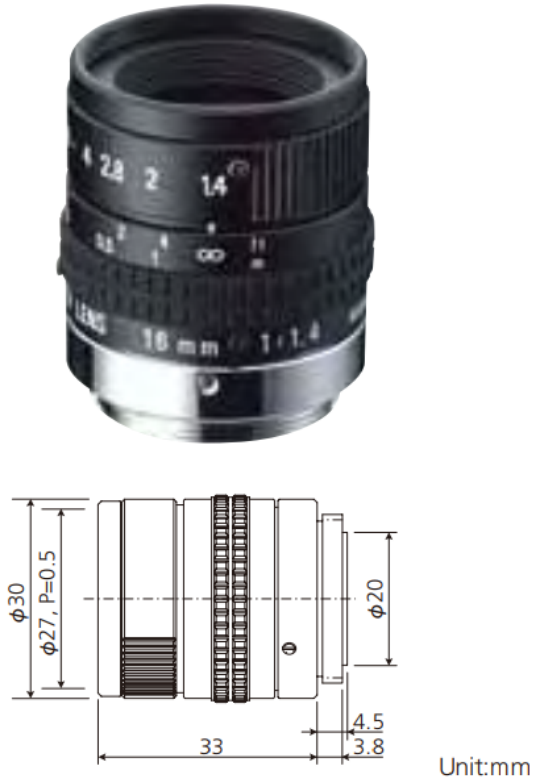


Figure 5.3: Pentax C1614A lenses for Phase 2 XRM imaging system [48].

Table 5.2: XRM beam parameter in HER during Phase 2 commissioning of SuperKEKB Operation.

| Parameter | | HER | Unit |
|---|-----------------------|------------------------|--------------------|
| Beta function at XRM source point | $\beta_{y,source}$ | 7.64 | m |
| Vertical emittance/(bump-height)squared | $\Delta\varepsilon_y$ | 41.978 ± 0.020 | pm/mm ² |
| Change in vertical dispersion/bump-height | $\eta_{y,source}$ | 0.019 | m/mm |
| Momentum spread | σ_p | 6.304×10^{-4} | |
| Beam current | I | 60 – 100 | mA |
| Number of bunches/ring | n_b | 788 | |

time study, simulations of the bunch lengthening with the microwave instability (MWI) simulation are made with the result as shown in Fig. 5.8 [50]. The lifetime study as Phase 1 (Subsection 4.3) was repeated, fitting the lifetime with

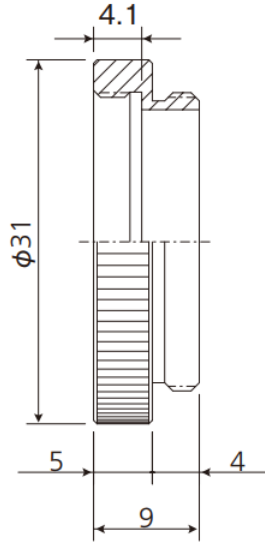


Figure 5.4: Macro ring to be inserted between lens and camera to shorten the object distance (close up to scintillator) [48].



Figure 5.5: A Basler acA2440-20gm CCD camera for the Phase 2 XRM imaging system [49].

the bunch length correction using Eq. 4.8 with k and σ_s as free parameters, gives results as shown in Fig 5.9. The average of PSF factor σ_s was found to be $6.60 \pm 0.73 \mu\text{m}$. The study results suggest the PSF $\sigma_s \sim 6.6 \mu\text{m}$, which is $\sim 5 \times$ smaller than in the Phase 1. This PSF correspond to the PSF source from camera system and scattering beamline as has been explained in Subsection 4.4. This σ_s indicate that the minimum beam size that we measured is correspond

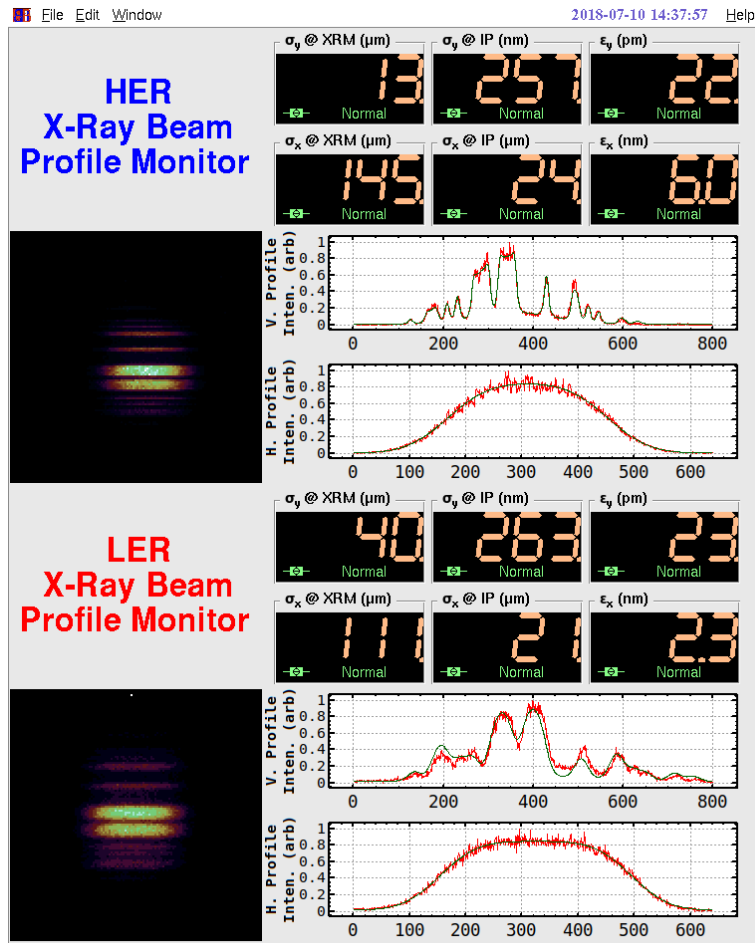


Figure 5.6: XRM panel in control room, showing the beam sizes at the XRM source in both rings, emittances, and beam sizes at interaction point.

to the emittance at full current (12.9 pm). Now that the σ_s is small enough, its should not be as a limit factor in the σ_y measurements and will be able to measure the beam size at zero current $\sigma_y \sim 7 \mu\text{m}$.

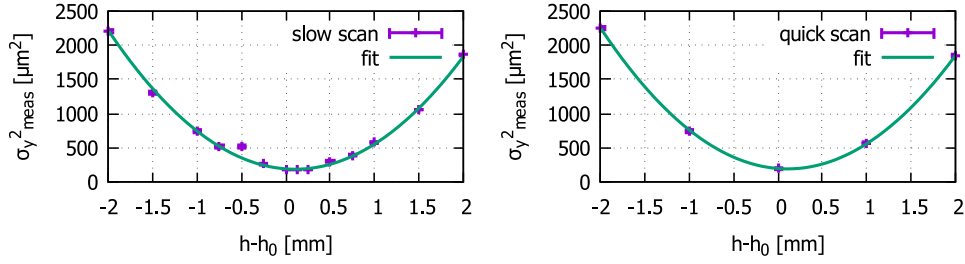


Figure 5.7: HER emittance control knob study for URA mask, taken with slow (left) and quick (right) knob scans. We did a quick scan after slow scan to avoid the change of beam condition during the measurements. The consistency factors between measured and SAD simulation beam sizes are 0.996 ± 0.007 and 1.002 ± 0.003 for slow and quick scans, respectively.

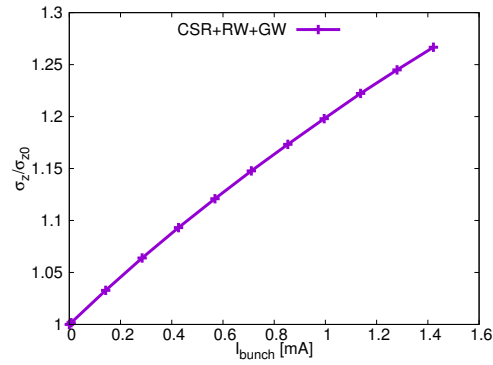


Figure 5.8: The MWI simulation to predict the bunch lengthening with all the wakes: coherent synchrotron radiation (CSR), resistive wall (RW), and geometrical wake (GW), with the σ_{z0} is 5.33 mm [50].

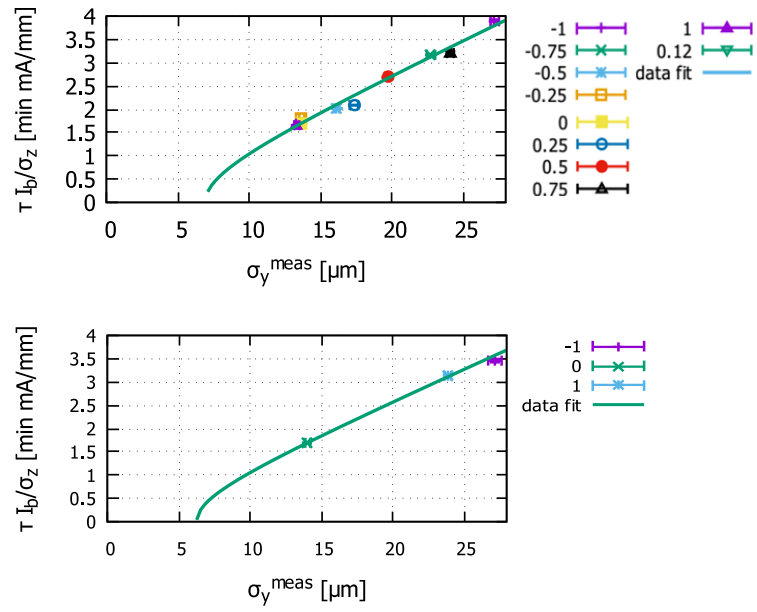


Figure 5.9: Relation between lifetime and measured beam size with bunch length correction for each bump height: (top) slow scan, (bottom) quick scan. Fitted using Eq. 4.8 to obtain the PSF factor σ_s . The average of σ_s was found to be 6.60 ± 0.73 μm , which is about 5 times smaller than Phase 1.

6 | Coded Aperture Reconstruction Image

This chapter explores the fundamentals of coded aperture imaging in general and the possibility to be implemented in the XRM image reconstruction. In the next phase, we will replace the scintillator with 128 channels of silicon with 2-mm sensing depth and a pixel pitch of 50 μm , with the aim to provide high-resolution bunch-by-bunch, turn-by-turn measurements for low emittance tuning, collision tuning, and instability measurements. In the current phase, we are using the template-fitting method that has excellent capability in the reconstruction of the image source, but in the future, for a single-bunch measurement this method cannot keep up with the vast volumes of data in real-time. We are investigating a fast reconstruction method based on coded aperture (CA) imaging for XRM. This method is important for measuring the beam sizes of all 2500 bunches in the SuperKEKB accelerator over thousands of turns, as needed for instability studies and luminosity tuning.

6.1 The History of Coded Aperture

Coded aperture techniques were first proposed in 1961 by Mertz and Young [27] that overcomes the conflicting requirements for imaging with a single pinhole camera. Figure. 6.1 shows the concept of coded aperture, the single pinhole is replaced by many pinholes (called the aperture), so that many overlap images are formed on the screen.

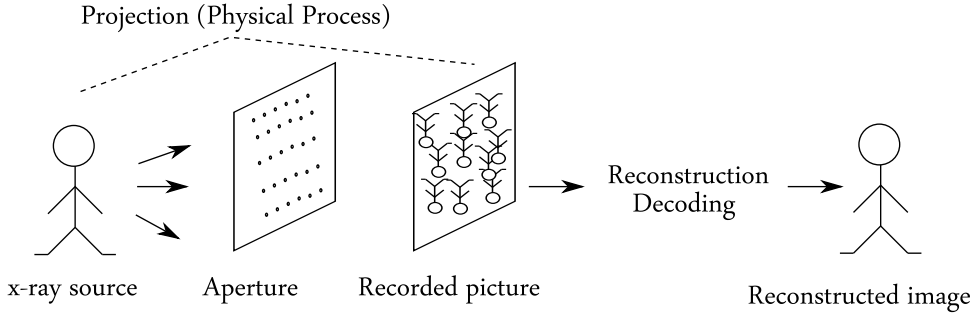


Figure 6.1: The basic concept of coded aperture imaging (adopted from [31]). In an attempt to obtain a higher signal to noise (SNR) ratio, a multiple-pinhole aperture is used to form many overlapping images of the object. There are two steps: the first is physical process, the projection of the source through the aperture; the second process is decoding.

Coded aperture try to achieve the resolution of small pinholes while maintaining a high signal throughput. The basic idea is to overcome photon shortage by opening many small pinholes instead if a larger one because some resolution limit will be reached. These pinholes are placed in arrays called pattern. Since the number of photons passing through a pinhole of the coded aperture is independent of photon passing trough all other pinholes, each pinhole is independent of the others. In a far-field approximation, i.e., when the object is sufficiently far from mask and detector (in astronomy), the projection process will follows the equation:

$$\mathbf{R}_{\text{image}} = \mathbf{O} \times \mathbf{A}_{\text{mask}}, \quad (6.1)$$

where $\mathbf{R}_{\text{image}}$ is the counts recorded by the detector, \mathbf{O} the number of photons emitted per unit area of the object, \mathbf{A}_{mask} the transmission of the coded aperture, and \times indicates non-periodic correlation. As the pinholes can be several numbers (in astronomy could be several hundreds), $\mathbf{R}_{\text{image}}$ does not resemble \mathbf{O} in any immediate way. An alternative way of looking at the same process is to say that a point in the image is not represented on the detector by point, but rather by pattern of points. This is the mask itself, as follows from Equation. 6.1

when \mathbf{O} is replaced with Dirac's delta function δ :

$$\mathbf{R}_{\text{image}} = \delta \times \mathbf{A}_{\text{mask}} = \mathbf{A}_{\text{mask}}. \quad (6.2)$$

Therefore, each point source is present in the projection not as a point but as a known pattern. Different point sources are characterized by the pattern shift and in this sense the signal from the source is encoded. In a more general case the pattern \mathbf{A}_{mask} is associated with decoding pattern \mathbf{G}_{mask} such that

$$\mathbf{A}_{\text{mask}} \otimes \mathbf{G}_{\text{mask}} = \delta, \quad (6.3)$$

where \otimes indicates periodic correlation, the matched filtering process is

$$\mathbf{R}_{\text{image}} \otimes \mathbf{G}_{\text{mask}}. \quad (6.4)$$

The result of this equation is to produce a perfect copy of the object \mathbf{O} . In fact, given a linearity of correlation operations and Equation. 6.1 can be write (as proven in Appendix B.3):

$$\hat{\mathbf{O}} \equiv \mathbf{R}_{\text{image}} \otimes \mathbf{G}_{\text{mask}} = (\mathbf{O} \times \mathbf{A}_{\text{mask}}) \otimes \mathbf{G}_{\text{mask}} = \mathbf{O} * (\mathbf{A}_{\text{mask}} \otimes \mathbf{G}_{\text{mask}}), \quad (6.5)$$

where $\hat{\mathbf{O}}$ is the estimate object/reconstructed image. It is clear that the closer the $(\mathbf{A}_{\text{mask}} \otimes \mathbf{G}_{\text{mask}})$ approximates the delta function, the better will be the estimate $\hat{\mathbf{O}}$. The $(\mathbf{A}_{\text{mask}} \otimes \mathbf{G}_{\text{mask}})$ quantity is the system point spread function (SPSF). In practice, image quality may be lost because the SPSFs of almost all coded apertures are not delta functions. Typically, the SPSF is a delta function surrounded by sidelopes which are not flat. Equation 6.5 can be the basis for decoding regardless of whether optical or digital techniques are employed. The choice of decoding function and whether to use optical or digital methods is usually closely linked to the choice of the aperture pattern. Several aperture pattern that have been used with their advantages and limitations are explained in Subsections 6.1.1 and 6.1.2.

6.1.1 Fresnel zone plates

The Fresnel zone plates (FZP) was proposed by Mertz and Young [27] as shown in Fig. 6.2. The FZP is defined such that the radius of the n^{th} zone is given by [51]

$$r_{n(\text{fzp})} = r_{1(\text{fzp})}\sqrt{n(\text{fzp})}, \quad (6.6)$$

where r_1 is the radius of innermost zone. The total open area equals the closed area, hence the FZP always has a transmission of 0.5. The FZP could produce the delta function SPSF but it is impractical to build because imperfect imaging properties hold only if the plates is infinite and has a continuously varying transmission and this entails fabrication difficulties.

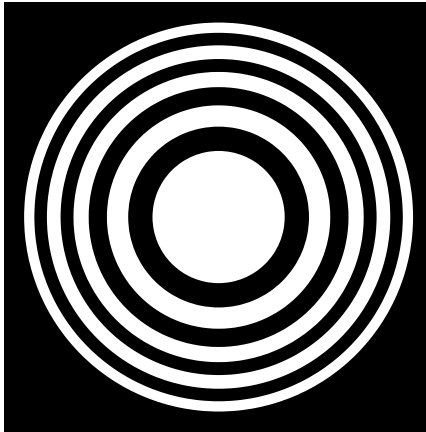


Figure 6.2: The practical Fresnel zone plate.

6.1.2 Random arrays

The advent of more manageable aperture gave new momentum in the field. In 1968, Dicke pointed out that random array has reasonable a self-correlation properties [14]. Unfortunately, just like FZP, a random array provides an ideal reconstructed images only if it is infinite. In 1971, the Non Redundant Arrays (NRA) were proposed [52]. These arrays are compact but have ideal properties only on a small field of view and contain a small number of holes, which prevents

great improvements in the SNR. The difficulty was overcome in 1978, when Fenimore and Cannon introduced the rectangular Uniformly Redundant Arrays (URA), which have an ideal PSF and are finite [51].

6.2 Fundamental of Code Aperture Imaging

6.2.1 Mathematical Formulation of Coded Aperture Imaging

Coded aperture imaging is a technique well developed among x-ray astronomers [14] which can, due to higher X-ray collection efficiency, improve on the spatial resolution of a pinhole camera. In astronomy applications, the object is typically 2-dimensional while the XRM is a 1-dimensional device. We consider the geometrical optics of the CA as shown in Fig 6.3, where \mathbf{r}_o , b , and f are the source position, source-to-mask distance, and mask-to-detector distance, respectively, the number of counts recorded at the detector position \mathbf{r}_i is given by [53]

$$R_{\text{image}}(\mathbf{r}_i) \propto \int \int_{\mathbf{r}_o} O(\mathbf{r}_o) A_{\text{mask}} \left(\frac{b}{z} \mathbf{r}_i + \frac{f}{z} \mathbf{r}_o \right) \cos^3(\theta) d^2 \mathbf{r}_o, \quad (6.7)$$

where $\theta = \arctan(|\mathbf{r}_i - \mathbf{r}_o|/z)$ characterizes the trajectories of skew rays through the system, O is the distribution of the object plane, and A_{image} is the transmission of the aperture (at the mask plane). If we define

$$\begin{aligned} \boldsymbol{\xi} &= -\frac{f}{b} \mathbf{r}_o, \\ O'(\mathbf{r}) &= O\left(\frac{-b}{f} \mathbf{r}\right), \\ A'_{\text{mask}}(\mathbf{r}) &= A_{\text{mask}}\left(\frac{-b}{z} \mathbf{r}\right). \end{aligned} \quad (6.8)$$

We obtain the form

$$R_{\text{image}}(\mathbf{r}_i) \propto \int \int_{\xi} O'(\xi) A'_{\text{mask}}(\mathbf{r}_i - \xi) \times \cos^3 \left[\arctan \left(\frac{|\mathbf{r}_i + \frac{b}{f} \xi|}{z} \right) \right] d^2 \xi. \quad (6.9)$$

Here O' and A'_{mask} are, respectively, rescaled and reflected forms of the object and aperture. The scaling coefficient for O' is the magnification of the pinhole camera (the negative sign indicates that the object is inverted), whereas the scaling coefficient for A'_{mask} is the ratio of the size of the mask to the size of its projection on the detector. In the far-field approximation, i.e., the object is sufficiently far from the mask and detector, the rays coming from the same point source in the object can be considered parallel so that $\cos^3(\theta) \cong 1$. Under this approximation, the relation in Eq. 6.9 is reduced to convolution [31], which is the correlation of the rescaled object with the rescaled mask.

$$R_{\text{image}}(\mathbf{r}_i) \propto \int \int_{\xi} O'(\xi) A'_{\text{mask}}(\mathbf{r}_i - \xi) d^2 \xi,$$

$$R_{\text{image}} = O' * A'_{\text{mask}}. \quad (6.10)$$

If we have an ideal pair of mask and decoding pattern $(A_{\text{mask}}, G_{\text{mask}})$, i.e., a pair such that $A_{\text{mask}} \otimes G_{\text{mask}} = \delta$, then the reconstructed image \hat{O} is defined as [31]

$$\begin{aligned} \hat{O} &= (O' * A'_{\text{mask}}) \otimes G'_{\text{mask}} = \mathfrak{R}[O' * (G'_{\text{mask}} \otimes A')_{\text{mask}}] \\ &= \mathfrak{R}(O' * \delta) = \mathfrak{R}(O'), \end{aligned} \quad (6.11)$$

where \mathfrak{R} is reflection operator. The reconstructed object is the object itself apart from a rescaling constant.

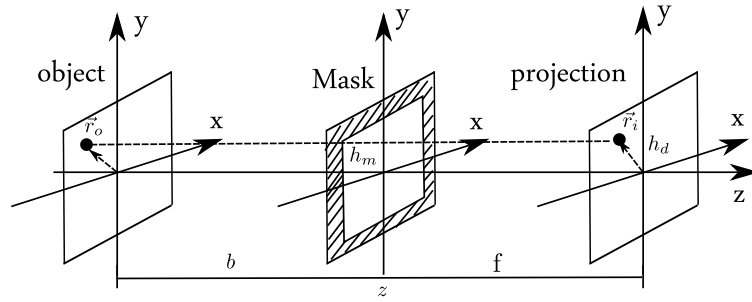


Figure 6.3: Geometrical optic of coded aperture imaging.

6.2.2 Coded Aperture Imaging in X-Ray Beam Size Monitor

There are two steps in the coded aperture imaging concept: the first is encoding, and the second is decoding.

Encoding

The encoding is the physical process of projecting of the object through the mask and onto the detector. In the XRM, after passing through an optical element, the X-rays from a point source form a diffraction pattern with an arrange of peaks on the detector depending on the pattern of the optical element. This pattern is the point response function (PRF), i.e., the expected X-ray intensity distribution at the image plane for a given X-ray spectrum, beamline geometry, and optical element. As has been described in Chapters 2 and 3.

Decoding

The second step of coded aperture imaging is extracting the encoded data (image reconstruction). Various methods for image reconstruction are possible, direct deconvolution (using Fourier transform, FT) and correlation methods are examples. The straightforward way of performing the image reconstruction is employing the Fourier transform which reduces a convolution to a simple multiplication. Providing the Fourier transform of each function in Eq. 6.10

with a noise term N_{noise} , the estimate \hat{O} is then given by:

$$\hat{O} = \mathcal{F}^{-1} \left(\frac{\mathcal{F}(R_{\text{image}})}{\mathcal{F}(A_{\text{mask}})} \right) = O - \mathcal{F}^{-1} \left(\frac{\mathcal{F}(N_{\text{noise}})}{\mathcal{F}(A_{\text{mask}})} \right). \quad (6.12)$$

The main problem with direct deconvolution methods is that $\mathcal{F}(A_{\text{mask}})$ might have small terms. The mask aperture A_{mask} is usually defined as an array of ones and zeros where the ones have the same pattern in the array as do the pinholes in the aperture. Another method of decoding is suggested by Eqs. 6.10 and 6.11 as shown in Eq. 6.13 where N is a noise term. The choice of the decoding matrix G_{mask} must be such that $G_{\text{mask}} * A_{\text{mask}}$ is as close as possible to a delta function, to preserve the object features within the system resolution. One method is to use the array A_{mask} itself as the decoding matrix which is the auto-correlation method [31].

$$\begin{aligned} \hat{O} &= (O' * A'_{\text{mask}} + N) \times G_{\text{mask}} = (O' * A'_{\text{mask}}) \times G_{\text{mask}} + N \times G_{\text{mask}} \\ &= O' * (A'_{\text{mask}} \times G_{\text{mask}}) + N_{\text{noise}} \times G_{\text{mask}}. \end{aligned} \quad (6.13)$$

If $A'_{\text{mask}} \times G_{\text{mask}} = \delta$ then Eq. 6.13 becomes $\hat{O} = O' + N_{\text{noise}} \times G_{\text{mask}}$. The noise term is still present but unlike in the Fourier transform method, is not ill-behaved. An improvement over the auto-correlation method process can be obtained by a balanced correlation method [53], that is achieved by using the G_{mask} array as,

$$\begin{aligned} G_{\text{mask}}(i, j) &= 1 \quad \text{if } A_{\text{mask}}(i, j) = 1, \\ G_{\text{mask}}(i, j) &= -\rho_A / (1 - \rho_A) \quad \text{if } A_{\text{mask}}(i, j) = 0, \end{aligned} \quad (6.14)$$

where ρ_A is the density of the aperture array. The balanced method is similar to the mismatch method of Brown [54] that defined G_{mask} array as

$$\begin{aligned} G_{\text{mask}}(i, j) &= 1 \quad \text{if } A_{\text{mask}}(i, j) = 1, \\ G_{\text{mask}}(i, j) &= -1 \quad \text{if } A_{\text{mask}}(i, j) = 0. \end{aligned} \quad (6.15)$$

If the $\rho_A = 0.5$ the balanced correlation is the same as the Brown mismatch approach; the balanced correlation will work better than the mismatch when ρ_A is not 0.5 [31].

6.2.3 Implementation

In implementing the coded aperture imaging, we proceed as below for the Phase 1 data:

1. We defined b and f with the beamline arrangement as shown in Fig. 6.3.
2. The mask aperture A_{mask} is 12-slits pattern as shown in Fig. 3.12 with 47 pixels size. The holes occupy $\sim 48\%$ of the aperture then we defined G_{mask} as

$$\begin{aligned} G_{\text{mask}}(i, j) &= 1 \quad \text{if } A_{\text{mask}}(i, j) = 1 \\ G_{\text{mask}}(i, j) &= -0.917 \quad \text{if } A_{\text{mask}}(i, j) = 0. \end{aligned} \quad (6.16)$$

3. We constructed the G_{mask} pattern, the correlation between A_{mask} and G_{mask} is a δ function as shown in Fig. 6.4
4. The detector is 128 channels of silicon with 2-mm sensing depth and a pixel pitch of 50 μm .
5. The pixel size of the projection image R_{image} in the detector is 128, so we need to re-binned it into 47 pixels to make it suitable for G_{mask} in the deconvolution process.
6. Deconvolution process using the direct convolution (FT) and correlation methods, we considered without noise term.
7. In the case of XRM, the object is a single source with a Gaussian vertical spread. Therefore, we applied Gaussian fitting in the reconstructed image.

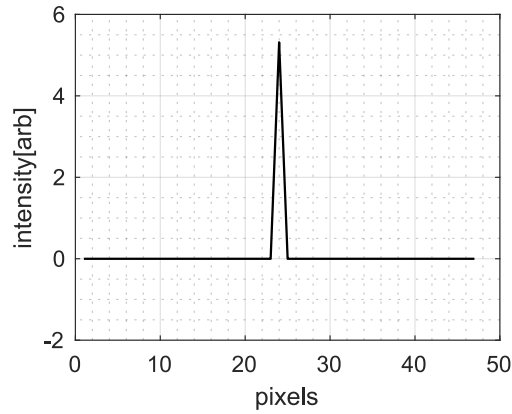


Figure 6.4: Correlation between A_{mask} and G_{mask} .

The results of decoding using both methods are shown in Figs. 6.5 and 6.6. The reconstructed image is a Gaussian function with an artifact/sidelobe even though the correlation between A_{mask} and G_{mask} is a perfect delta function. This artifact could be because the masking region of the image does not entirely block the x-rays, allowing some background to leak through the mask pixels.

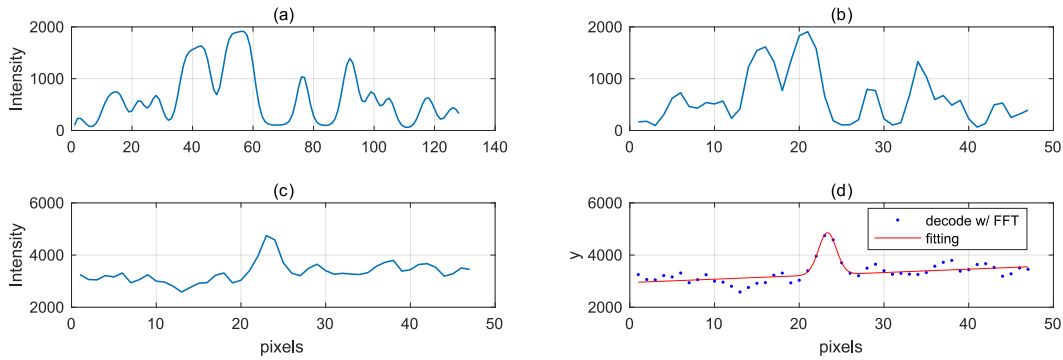


Figure 6.5: Image reconstruction process using direct deconvolution/FT method: (a) recorded image in 128 pixels, (b) recorded image in 47 pixels, (c) decode image using FT, (d) fitting result.

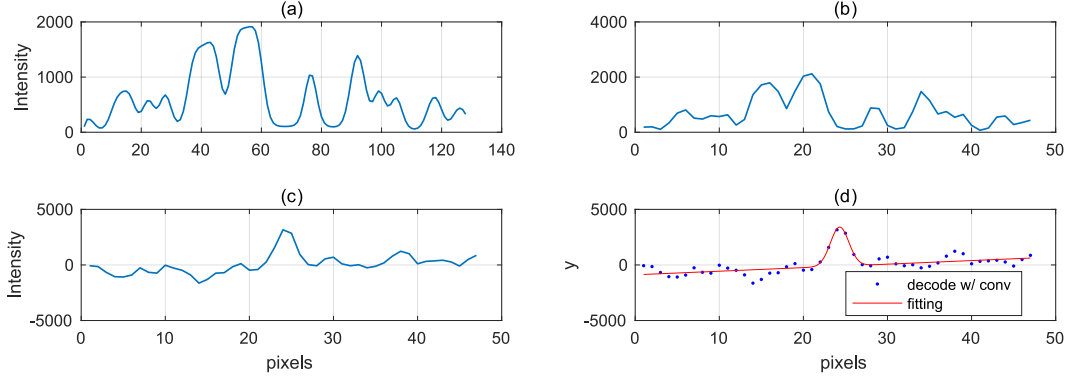


Figure 6.6: Image reconstruction process using correlation methods: (a) recorded image in 128 pixels, (b) recorded image in 47 pixels, (c) decode image using correlation method, (d) fitting result.

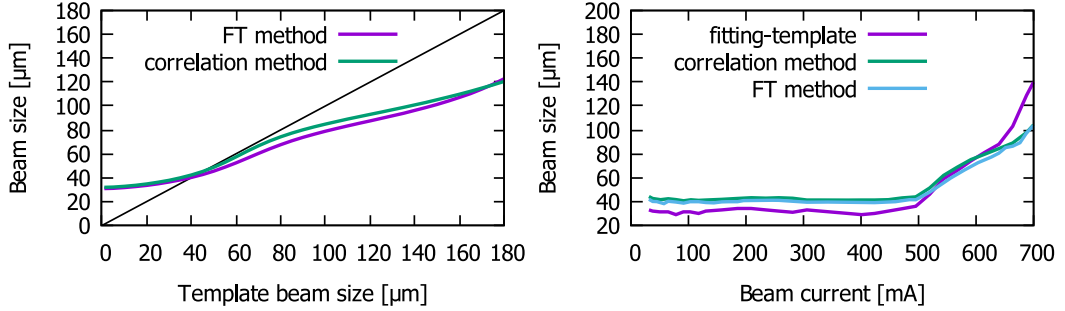


Figure 6.7: Comparison of CA deconvolution technique and fitting-template method.

During the Phase 1 of SuperKEKB commissioning (Spring 2016), we collected data of beam size as a function of beam current using the fitting-template method. Figure 6.7 shows the comparison of CA deconvolution technique and fitting-template method. For beam size smaller than $80 \mu\text{m}$ as shown in Fig. 6.7 (left), the result is reasonable. For large beam sizes, there is a significant deviation compared to the template beam size. One reason is the difficulty in Gaussian fitting, especially at large beam sizes. This difficulty could be because of the artifact that appears as we mentioned before. In Fig. 6.7 (right), there is a small deviation between CA deconvolution and fitting-template at the lower beam current ($< 500 \text{ mA}$). At the beam current less than 500 mA ,

the raw beam size is on the range $38 - 41 \mu\text{m}$. The point-spread function (PSF) of the single slit ($33 \mu\text{m}$) when the detector (Si) sees it is $\sim 34 \mu\text{m}$ (include the geometrical magnification ~ 3 times), then we would be able to see the raw beam size smaller than the PSF. In further study, we need to study the fitting-method for the simulated detector image and compare it with the phase I data result.

7 | Summary and Outlook

This chapter summarizes the work presented in this thesis and discusses possible direction for future research.

7.1 Summary

7.1.1 X-Ray Beam Size Monitor

The SuperKEKB facility is the upgrade of KEKB to increase the luminosity 40 times, to $8 \times 10^{35} \text{ cm}^{-2}\text{s}^{-1}$, with the overarching mission is to search a new physics beyond the standard model of the particle physics in the B meson regime. It has two rings: High Energy Ring (HER) and Low Energy Ring (LER) for 7 GeV electron and 4 GeV positron, respectively.

Beam instrumentation in the accelerator is the 'eyes' of the machine operators, its entail the design, construction and operation of instruments to observe particle beams, and also the research and development to find new or improve existing technique to fulfill particularly new requirements. Several beam parameters that we need to measure in the accelerator (e.g., SuperKEKB) are beam position (to know the horizontal and vertical positions of the beam throughout the accelerator chamber), beam intensity, and lifetime measurement. Other parameters are beam loss, beam profile (actual shape of the beam, both transverse and longitudinal planes), and collision rate to measure of how well the beams overlap at the collision point.

There are two different types of synchrotron radiation (SR) monitors for beam profile diagnostics in SuperKEKB: SR interferometer (visible-light moni-

tors) and x-ray beam size monitor (XRM). The XRM is used primarily for vertical bunch profile measurements, and the visible light monitors is used primarily for horizontal bunch profile measurements, with the possibility of vertical measurements at larger beam sizes for comparison with the XRM measurements.

Primary aim of the XRM is for vertical beam size measurements that eventually has the capability for a high-resolution bunch-by-bunch, turn-by-turn measurements for low emittance tuning, collision tuning, and instability measurements. The motivation of the presented research was to study the development of the XRM, consist of design the mask patterns, calibration of the XRM during the commissioning of the SuperKEKB operation, and explore the image reconstruction technique using uniformly redundant arrays (URA) coded aperture.

The main idea of the XRM system was to propagate the X-rays from SR source point (bending magnet) through optical elements to the observation plane (detector). It formed a diffraction pattern with an array of peaks on the detector depending on the pattern of the optical elements. This pattern is a point spread function (PSF), i.e., the expected X-ray intensity distribution at the observation plane for a given X-ray spectrum, beamline geometry, and optical elements. We used a Fresnel-Kirchhoff diffraction approximation to estimate the propagation of the X-ray distribution from the SR source to the detector.

7.1.2 Optical Element

There are two types of the optical element for XRM in both rings: a single pinhole and coded apertures (CA). In the pinhole imaging, the hole should be small to provide resolution. However, a small hole often has an insufficient area to collect enough X-rays to produce an interpretable image. The capability of CA become useful to overcome the limitation of pinhole imaging and provide better resolution. Because CA offers greater open aperture and photon throughput than a single pinhole, that makes CA has a capability for a better statistical resolution in a single-shot measurement. Accordingly, three optical elements/masks have been designed and installed at each ring: pinhole,

17 multi-slits, and 12-slits Uniformly Redundant Array (URA).

7.1.3 Phase 1 and 2 Commissioning

In the Phase 1 commissioning, the overall performance at the low energy ring (LER) were consistent with expectations based on the optics estimation $\varepsilon_y \sim 10$ pm and will be able to measure the design beam size at zero current (~ 14 μm). The high energy ring (HER) measurement predicted $\varepsilon_y \sim 35$ pm, which is $3.5 \times$ larger than the optics estimation and suggested a large point spread function (PSF) $\sigma_s \sim 31$ μm .

Studies were made during Phase 2 commissioning with several new equipment improvements in the HER: thinner Be filters, updated optical elements, a new scintillator screen, and CCD camera with the purpose to reduce the PSF. The results show a PSF $\sigma_s \sim 6.6$ μm , which is $5 \times$ smaller than in Phase 1. This revised σ_s indicates that the minimum measured beam size corresponds to the emittance at the design current (12.9 pm). The σ_s is also small enough to measure the design beam size at zero current, $\sigma_y \sim 7$ μm . The resulting vertical beam size measurements in Phase 1 and 2 are summarized in Table 7.1.

Table 7.1: Vertical beam size measurements in Phase 1 and 2.

| Parameter | Phase 1 | | Phase 2 | Unit |
|------------------------------|------------------|------------------|------------------|---------------|
| | LER | HER | HER | |
| σ_y optics estimation | ~ 25 | ~ 9 | ~ 9 | μm |
| σ_y measured | 21.56 ± 2.90 | 16.93 ± 0.75 | 12.35 ± 0.39 | μm |
| σ_s (inferred PSF) | 15.63 ± 2.90 | 31.58 ± 0.72 | 6.60 ± 0.73 | μm |

7.2 Direction for future work

For further explorations and refinement following present work, two directions of research are identified and are presented below.

7.2.1 Fast detector for single-shot measurement

In the next phase, the scintillator will be supplemented by 128 channels of silicon with 2-mm sensing depth and a pixel pitch of 50 μm . This detector system will have a capability for the single-shot measurement which is useful for studying beam instabilities.

7.2.2 Image reconstruction based on URA coded aperture

In the current phase, we are using the template-fitting method that has excellent capability in the reconstruction of the image source, but in the future, for a single-bunch measurement this method cannot keep up with the vast volumes of data in real-time. An investigating of fast reconstruction method based on URA coded aperture imaging for XRM more deeply become interesting. This method is essential for measuring the beam sizes of all 2500 bunches in the SuperKEKB accelerator over thousands of turns, as needed for instability studies and luminosity tuning.

Appendix A

Synchrotron Radiation

A.1 Derivation of the SR spatial distribution emitted by relativistic charges on circular orbit

Recalling Eq. 2.1, the total radiated SR power in the relativistic case can be expressed by:

$$P_{tot} = \frac{e^2 c}{6\pi\epsilon_0(m_0c^2)^2} \left(\frac{d\vec{p}}{d\tau} \right)^2 \quad (\text{a.1})$$

that for the case of a circular acceleration in a bending dipole ($d\vec{v}/d\tau \perp \vec{v}$), reduces to:

$$P_{tot} = \frac{e^2 c \gamma^2}{6\pi\epsilon_0(m_0c^2)^2} \left(\frac{d\vec{p}}{dt} \right)^2 \quad (\text{a.2})$$

It is worth nothing that in a circular trajectory with the radius ρ , a change of the orbit angle $d\alpha$ causes a momentum variation $dp = p d\alpha$. the latter could also be expressed by:

$$\frac{dp}{dt} = p\omega = \frac{pv}{\rho} = \frac{E}{\rho} \quad (\text{a.3})$$

Therefore by substituting $\gamma = E/m_0c^2$ in Eq. a.2, the dependency of the radiated power on the particle energy E is obtained:

$$P_{tot} = \frac{e^2 c}{6\pi\epsilon_0(m_0c^2)^4} \frac{E^4}{\rho^2} \quad (\text{a.4})$$

By inserting the obtained Poynting vector at the radiated time in the expression of the total power radiated power per unit solid angle (see reference [19]), the latter becomes

$$\frac{dP}{d\Omega} = \frac{1}{c\mu_0} \vec{E}^2 (1 + \vec{n}\vec{\beta}) R^2 \quad (\text{a.5})$$

By using the electric expression (see reference [17]), the radiated power distribution can be expressed as follows:

$$\begin{aligned} \frac{dP}{d\Omega} &= \frac{1}{c\mu_0} \frac{e^2}{(4\pi\epsilon_0)^2} \frac{1}{c^2 a^6} \cdot \left\{ \vec{R} \times \left[\left(\vec{R} + \vec{\beta} R \right) \times \dot{\vec{\beta}} \right] \right\}^2 (1 + \vec{n}\vec{\beta}) R^2 \\ &= \frac{1}{c\mu_0} \frac{e^2}{(4\pi\epsilon_0)^2} \frac{R^5}{c^2 a^5} \left\{ \vec{n} \times \left[\left(\vec{n} + \vec{\beta} \right) \times \dot{\vec{\beta}} \right] \right\}^2 \end{aligned} \quad (\text{a.6})$$

Recalling the reference coordinates system K^* , see reference [19]: in K^* , the

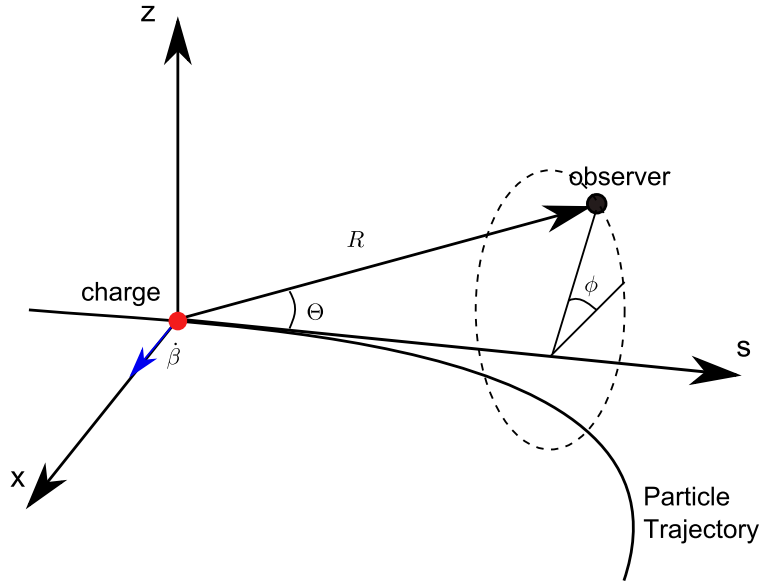


Figure 1: The geometry used for the treatment of synchrotron radiation, featuring K^* as coordinates system moving along the trajectory.

vector position \vec{R} , pointing from the observer to the moving particle, and its

unit vector are given by

$$\vec{R} = -R \begin{pmatrix} \sin \Theta \cos \phi \\ \sin \Theta \sin \phi \\ \cos \Theta \end{pmatrix} \quad (\text{a.7})$$

$$\vec{n} = \begin{pmatrix} -\sin \Theta \cos \phi \\ -\sin \Theta \sin \phi \\ -\cos \Theta \end{pmatrix} \quad (\text{a.8})$$

The Lorentz force \vec{F} of an electron traveling along a trajectory in a magnet is then expressed by:

$$\vec{F} = -e\vec{v} \times \vec{B} = -e \begin{pmatrix} -vB_z \\ 0 \\ 0 \end{pmatrix} = \gamma m_0 \dot{\vec{v}} \quad (\text{a.9})$$

By the nature of the particle circular motion, we recall that

$$\vec{v} = \begin{pmatrix} 0 \\ 0 \\ v \end{pmatrix}, \quad \dot{\vec{v}} = \begin{pmatrix} \dot{v}_x \\ 0 \\ 0 \end{pmatrix}, \quad \text{and} \quad \vec{B} = \begin{pmatrix} 0 \\ B_z \\ 0 \end{pmatrix} \quad (\text{a.10})$$

Therefore: $\gamma m_0 \dot{v}_x = evB_z = ec\beta B_z$. The bending radius of a trajectory in a magnet can be evaluated according to:

$$\frac{1}{\rho} = \frac{e}{p} B_z = \frac{eB_z}{\gamma m_0 v} \Rightarrow B_z = \frac{\gamma m_0 v}{e\rho} \quad (\text{a.11})$$

and the transverse acceleration of the particle becomes:

$$\dot{v}_x = \frac{c^2 \beta^2}{\rho} \quad (\text{a.12})$$

obtaining finally:

$$\vec{\beta} = \frac{\vec{v}}{c} = \begin{pmatrix} 0 \\ 0 \\ v/c \end{pmatrix} \quad (\text{a.13})$$

and

$$\dot{\vec{\beta}} = \begin{pmatrix} \dot{v}/c \\ 0 \\ 0 \end{pmatrix} = \begin{pmatrix} (c\beta^2)/\rho \\ 0 \\ 0 \end{pmatrix} \quad (\text{a.14})$$

By using the mathematical identity:

$$\left\{ \vec{n} \times \left(\left[\vec{n} + \vec{\beta} \right] \right) \times \dot{\vec{\beta}} \right\} = \left(\vec{n} + \vec{\beta} \right) \left(\vec{n} \cdot \dot{\vec{\beta}} \right) - \dot{\vec{\beta}} \left(1 + \vec{n} \cdot \vec{\beta} \right) \quad (\text{a.15})$$

and recalling a

$$a = R(1 + \vec{n} \cdot \vec{\beta}) = R(1 - \beta \cos \Theta) \quad (\text{a.16})$$

the radiation power per unit solid angle is finally obtained:

$$\frac{dP}{d\Omega} = \frac{1}{c\mu_0} \frac{e^2}{(4\pi\epsilon_0)^2} \frac{\beta^4 (\beta^2 - 1) \sin^2 \Theta \cos^2 \phi + (1 - \beta \cos \Theta)^2}{(1 - \beta \cos \Theta)^5} \quad (\text{a.17})$$

A.2 Energy Radiated per-unit Frequency per-unit Solid Angle

Radiation field $E_x(t) = E_{\text{rad}}$ and its Fourier transform $E_x(\omega)$

$$\begin{aligned} E_x(t) &= \frac{e}{4\pi\epsilon_0 c^2 R_0} a'_\perp(t) & (\text{a.18a}) \\ &\equiv \frac{1}{\sqrt{2\pi}} \int_{-\infty}^{\infty} E_x(\omega) e^{-i\omega t} d\omega, \end{aligned}$$

$$\begin{aligned} E_x(\omega) &= \frac{1}{\sqrt{2\pi}} \int_{-\infty}^{\infty} E_x(t) e^{i\omega t} dt \\ &= \frac{e}{32^{1/2} \pi^{3/2} \epsilon_0 c^2 R_0} \int_{-\infty}^{\infty} a'_\perp(t) e^{i\omega t} dt. & (\text{a.18b}) \end{aligned}$$

The energy density (energy per solid angle $d\Omega^2$) emitted by a single electron is given by the time integral of the Poynting vector $\vec{S} = \epsilon_0 c^2 \vec{E} \times B$

$$\begin{aligned} \frac{d^2 W}{d\Omega^2} &= R_0^2 \frac{d^2 W}{dx dy} = R_0^2 \int |\vec{S}(t)| dt \\ &= R_0^2 \epsilon_0 c^2 \int E_x(t) B_y(t) dt = R_0^2 \epsilon_0 c \int |E_x(t)|^2 dt. & (\text{a.19}) \end{aligned}$$

if we consider only a single pulse of radiation, we can extend the limits of integration to $\pm \infty$

$$\frac{d^2 W}{d\Omega^2} = R_0^2 \epsilon_0 c \int_{-\infty}^{\infty} |E_x(t)|^2 dt = R_0^2 \epsilon_0 c \int_{-\infty}^{\infty} |E_x(\omega)|^2 d\omega = 2R_0^2 \epsilon_0 c \int_0^{\infty} |E_x(\omega)|^2 d\omega, \quad (\text{a.20})$$

where we used the fact that $\frac{1}{2\pi} \int_{-\infty}^{\infty} e^{i(\omega-\omega')t} dt = \delta(\omega - \omega')$. We thus find the

spectral energy density radiated by a single electron is given by

$$\frac{d^3W}{d\Omega^2 d\omega} = 2R_0^2 \epsilon_0 c |E(\omega)|^2 = \frac{e^2}{16\pi^3 \epsilon_0 c^3} \left| \int_{-\infty}^{\infty} a'_{\perp}(t) e^{i\omega t} dt \right|^2 \quad (\text{a.21})$$

By(incoherently) adding the effects of I_{el}/e electrons per second, where I_{el} is the electron current in the synchrotron, and dividing the photon energy, we obtain the spectral photon flux density

$$\frac{d^2F}{d^2\Omega} = \frac{1}{\hbar\omega} \frac{I_{\text{el}}}{e} \frac{d^3W}{d^2\Omega d\omega} \Delta\omega, \quad (\text{a.22a})$$

$$\frac{d^2F}{d^2\Omega} = \alpha \frac{\Delta\omega}{\omega} \frac{I}{e} |A(\omega)|^2. \quad (\text{a.22b})$$

with

$$\alpha = \frac{e^2}{4\pi\epsilon_0 \hbar c} = \frac{1}{137} \quad (\text{a.23})$$

is the fine-structure constant. The components of the spectral-flux of the synchrotron radiation with polarization σ and π can be approximated by the x and z components with the angular photon frequency ω .

$$\frac{d^2F_{\sigma,\pi}}{d^2\Omega} = \alpha \frac{\Delta\omega}{\omega} \frac{I}{e} |A_{\sigma,\pi}(\omega)|^2. \quad (\text{a.24})$$

The wave-front amplitude $A_{\sigma\pi}$ is defined as

$$\begin{bmatrix} A_{\sigma} \\ A_{\pi} \end{bmatrix} = \frac{\omega}{2\pi} \int_{-\infty}^{\infty} dt' \begin{bmatrix} -\sin \omega_p t' \\ \psi \end{bmatrix} \exp(i\omega t(t')) dt' \quad (\text{a.25})$$

Introducing the critical frequency ω_c

$$\omega_c = \frac{3}{2} \gamma^3 \omega_p = \frac{3\gamma^3 c}{2\rho}, \quad (\text{a.26})$$

the exponent in the integrand of Eq. a.25 becomes

$$\omega_t(t') = \frac{3\eta}{2} \left(\tau + \frac{\tau^3}{3} \right) \quad (\text{a.27})$$

Here

$$\begin{aligned} \eta &= \frac{1}{2} \frac{\omega}{\omega_o} (1 + X^2)^{\frac{3}{2}}, \\ X &= \gamma\psi, \\ \tau &= \frac{\gamma\omega_p t'}{\sqrt{1 + X^2}}. \end{aligned} \quad (\text{a.28})$$

The integrals in Eq. a.25 can be expressed as the modified Bessel functions

$$K_{2/3}(\eta) = \sqrt{3} \int_0^\infty \tau \sin \left[\frac{3}{2} \eta \left(\tau + \frac{1}{3} \tau^3 \right) \right] d\tau, \quad (\text{a.29a})$$

$$K_{1/3}(\eta) = \sqrt{3} \int_0^\infty \tau \cos \left[\frac{3}{2} \eta \left(\tau + \frac{1}{3} \tau^3 \right) \right] d\tau. \quad (\text{a.29b})$$

The result is

$$\begin{bmatrix} A_\sigma \\ A_\pi \end{bmatrix} = \frac{\sqrt{3}}{2\pi} \gamma \frac{\omega}{\omega_c} (1 + X^2) (-i) \begin{bmatrix} K_{2/3}^2(\eta) \\ \frac{X^2}{1+X^2} K_{1/3}^2(\eta) \end{bmatrix}. \quad (\text{a.30})$$

Inserting this into Eq. a.24, we finally obtain the angular density of the spectral flux:

$$\begin{bmatrix} \frac{d^2 F_\sigma}{d^2 \Omega} \\ \frac{d^2 F_\pi}{d^2 \Omega} \end{bmatrix} = \frac{3\alpha}{4\pi^2} \gamma^2 \frac{\Delta\omega}{\omega} \frac{I}{e} \left[\frac{\omega}{\omega_c} \right]^2 (1 + X^2)^2 \begin{bmatrix} K_{2/3}^2(\eta) \\ \frac{X^2}{1+X^2} K_{1/3}^2(\eta) \end{bmatrix}. \quad (\text{a.31})$$

In the forward direction $\psi = 0$, the flux for the π component vanishes. In

practical units (photons/s/mrad²/0.1%BW) this becomes

$$\left. \frac{d^2 F}{d^2 \Omega} \right|_{\psi=0} = 1.33 \times 10^{13} E_{el}^2 [\text{GeV}] I_{el}[A] \left(\frac{\omega}{\omega_c} \right)^2 K_{2/3}^2 \left(\frac{\omega}{2\omega_c} \right), \quad (\text{a.32})$$

giving the spectral flux per mrad² solid angle and per 0.1% photon energy bandwidth.

Appendix B

URA Image Reconstruction

B.1 Definitions

Convolution :

$$F * G = \int F(x)G(y - x)dx \quad (\text{b.33})$$

Correlation:

$$F \times G = \int F(x)G(x + y)dx \quad (\text{b.34})$$

Circular/periodic Correlation:

$$F \otimes G = \int F(x)G(x \oplus y)dx \quad (\text{b.35})$$

\oplus indicates sum modulo D , $x \oplus y$ is $x + y$ if $0 \leq (x + y) < D$ and the remainder of the division $(x + y)/D$ otherwise.

B.2 Theorem 1: Correlation with a constant

If F is a constant function, then :

$$\begin{aligned} F \times G &= \int F(x)G(x + y)dx = \int F \cdot G(x + y)dx & (\text{b.36}) \\ &= F \int G(x + y)dx = F \int G(\xi)d\xi \end{aligned}$$

B.3 Theorem 2: $(O \times A) \otimes G = O * (A \otimes G)$

$$(O \times A) \otimes G = O * (A \otimes G) \quad (\text{b.37})$$

Proof

$$\begin{aligned} (O \times A) \otimes G &= \int_y \left(\int_x O(x)A(x+y)dx \right) G(y \oplus z)dy \quad (\text{b.38}) \\ &= \int_x O(x) \left(\int_y A(x+y)G(y \oplus z)dy \right) dx \end{aligned}$$

by replacing $\xi = x + y$

$$\begin{aligned} \int_x O(x) \int_y A(x+y)G(y \oplus z)dydx &= \int_x O(x) \int_\xi A(\xi)G(\xi - x \oplus z)d\xi dx \quad (\text{b.39}) \\ &= \int_x O(x)H(z - x)dx = O * H \end{aligned}$$

where

$$H(z - x) = \int_\xi A(\xi)G(\xi - x \oplus z)d\xi \quad (\text{b.40})$$

since it is recognized that $H = A \otimes G$, the theorem is proven.

Abbreviations List

| | |
|----------------|---|
| ARES | Accelerator Resonantly coupled with Energy Storage |
| BPM | Beam Position Monitor |
| CA | Coded Aperture |
| CesrTA | Cornell Electron/Positron Storage Ring Test Accelerator |
| CCD | Charge Coupled Device |
| CP | Conjugation Parity |
| CSR | Coherent Synchrotron Radiation |
| CT | Current Transformer |
| DC | Direct Current |
| DCCT | DC Current Transducers |
| DLS | Diamond Light Source |
| ECK | Emittance Control Knob |
| EGS | Electron Gamma Shower |
| FT | Fourier Transform |
| FZP | Fresnel Zone Plates |
| GW | Geometrical Wake |
| HER | High Energy Ring |
| HOM | Higher Order Mode |
| IP | Interaction Point |
| KEK | Ko Enerugi Kasokuki Kenkyu Kiko |
| LER | Low Energy Ring |
| LuAG:Ce | Lutetium aluminium garnet doped with cerium |
| MURA | Modified Uniformly Redundant Array |
| MWI | Microwave Instability |
| NRA | Non Redundant Array |
| PSF | Point Spread Function |

| | |
|---------------|---|
| PRF | Point Response Function |
| RW | Resistive Wall |
| RA | Random Array |
| RF | Radio Frequency |
| RMS | Root Mean Square |
| SAD | Structured Accelerator Design |
| SEM | Scanning Electron Microscope |
| SNR | Signal to Noise Ratio |
| SR | Synchrotron Radiation |
| QCS | Quadrupoles and compensation Solenoids |
| URA | Uniformly Redundant Array |
| XRM | X-ray Beam Size Monitor |
| YAG:Ce | Yttrium Aluminum Garnet doped with Cerium |

Symbol

| | |
|-------------------|--|
| α | Fine structure constant |
| a | Acceleration |
| A | Amplitude |
| A_{mask} | Mask/aperture array |
| β | Ratio of relative velocity to the speed of light |
| β_y | Vertical beta function |
| B | Magnetic field |
| c | Speed of light |
| χ^2 | Chi-squared |
| C | Circumference |
| cal | Calibration factor |
| δ | Phase shift |
| d | Effective bunch length for the nano-beam scheme |
| ds | Distance between downstream and upstream BPMs |
| d_z | Scintillator depth |
| D | Dispersion |
| D_{SRM} | Slit separation |
| $\Delta p/p$ | Momentum acceptance |
| e | Elementary electric charge |
| e^+ | Positron |
| e^- | Electron |
| E | Electric field |
| E_b | Beam energy |

| | |
|--------------------------|--------------------------------------|
| E_c | Critical energy |
| E_{rad} | Radiation energy |
| η_y | Vertical dispersion |
| F_{SRM} | Distance from mirror to source point |
| ε_y | Vertical emittance |
| ε_x | Horizontal emittance |
| ϵ_0 | Vacuum permittivity |
| $F(\xi)$ | Touschek factor |
| $\frac{d^2F}{d\Omega^2}$ | Spectral photon flux density |
| γ | Lorentz factor |
| G_{mask} | Decoding array |
| h | Bump height |
| h_0 | Offset of bump height |
| \bar{h} | Plank constant divided by 2π |
| I | Beam current |
| I_b | Bunch current |
| K | Bessel function |
| λ | wave length |
| \mathcal{L} | Luminosity |
| L | Distance from source to mask |
| L' | Distance from mask to detector |
| m_e | Electron mass |
| M | Geometrical magnification |
| m | Scintillator camera scale |
| n | Number of fit parameters |
| n_b | Maximal number of bunches |

| | |
|---------------------|---|
| N_e | Number of events |
| N_c | Number of detector channel |
| N | Number of particles in a bunch |
| N_{noise} | Noise term |
| n_p | Number of particle |
| n_{pole} | Number of magnet pole |
| n_{fzp} | n^{th} radius in FZP |
| NA | Numerical aperture of the camera |
| ω_c | Critical frequency |
| Ω^2 | Solid angle |
| ω | Frequency |
| P_o | Point source |
| P_1 | Position of peak feature from X-rays that passed through a slit onto detector |
| P_2 | Position of peak feature from X-rays that transmitted through the Au mask |
| R, r | Electron radius |
| R_f | Spatial resolution |
| R_L | Reduction factor of the luminosity |
| R_{ξ_y} | Reduction factor of the beam-beam parameter |
| R_{image} | Electron radius |
| \vec{r} | Electron path |
| r_1 | Distance from source to mask as a function of θ |
| r_2 | Distance from mask to detector as a function of θ |
| r_e | Classical electron radius |
| $r_{n(\text{fzp})}$ | Radius of the n^{th} zone |
| $r_{1(\text{fzp})}$ | Radius of the innermost zone |

| | |
|-----------------|-------------------------------|
| ρ | Radius of the bending magnet |
| ρ_A | Density of the aperture array |
| s | Source position |
| s_1 | Upstream BPM position |
| s_2 | Downstream BPM position |
| S | Wavefront |
| \vec{S} | Poynting vector |
| σ_x | Horizontal beam size |
| σ_y | Vertical beam size |
| σ_z | Bunch length |
| σ_p | Cross section |
| σ_i | Residual weighting |
| σ_p | Momentum spread |
| σ_s | Smearing factor size |
| σ_{beam} | RMS beam size |
| s_i | Signal height |
| t | Observer time |
| τ | Emitter time |
| \mathcal{T} | Touschek lifetime |
| T | Real transmission |
| T_{Be} | Thickness of beryllium filter |
| T'_{Be} | Thickness of beryllium window |
| θ_1 | Angle from source to mask |
| θ_2 | Angle from mask to detector |

| | |
|--------------------------|----------------------------------|
| $U(P)$ | Light disturbance at point P |
| φ | Phase angle |
| v | Particle motion |
| ξ_y | Vertical beam-beam parameter |
| $\frac{d^2W}{d\Omega^2}$ | Energy density |
| v | Degree of freedom |
| y | Vertical source position |
| y_1 | Vertical upstream BPM position |
| y_2 | Vertical downstream BPM position |
| y_m | Vertical coordinate of mask |
| y_d | Vertical coordinate of detector |

List of Figures

| | | |
|-----|--|----|
| 1.1 | Facilities and components of the SuperKEKB accelerator facility. Ring's circumference is ~ 3 km with four experimental hall buildings (Fuji, Nikko, Tsukuba, and Oho) [2]. | 2 |
| 1.2 | Schematic view of beam collision in the nano-beam scheme. The red and blue lines represent positron and electron beams, respectively. The size of the overlap region is d , which is considered to be an effective bunch length for the nano-beam scheme. | 5 |
| 2.1 | Lorentz transformation for the relativistic case, shapes the emitted SR angular distribution in a forward narrow cone: (left) Power distribution in the center of mass frame ($v = 0$), and (right) Power distribution in the laboratory frame ($v = 0.9c$) [19]. | 13 |
| 2.2 | The spectral distribution of synchrotron radiation from bending magnet for LER and HER in linear scale (left) and log scale (right). The critical energies are 4.4 and 7.2 keV for LER and HER, respectively. The critical energy corresponds to critical frequency ω_c , and divides the spectrum into two parts of equal radiated power: 50% of the total power is radiated at frequencies lower than ω_c and 50% is radiated at frequencies higher than ω_c . In the X-ray beam size monitor, we are using $E > E_c$ | 15 |
| 2.3 | Setup of the SR monitor based on visible light interferometry at Photon Factory, KEK [26]. | 16 |

| | | |
|------|---|----|
| 2.4 | Schematic of the XRM beamline at each of the SuperKEKB rings (not to scale). It consists of a beryllium filter placed upstream of the optics to reduce the heat load, three sets of optical elements (a single pinhole and two sets of coded apertures), a beryllium window, and the detector system. For the Phase 1 (Phase 2) of SuperKEKB commissioning, a 141- μm -thick YAG:Ce (LuAG:Ce) scintillator with a CCD camera focused on it as the imaging system. The scintillator screen is tilted 45° in the horizontal plane, so that the camera and lens are out of the way beam. In the next phase, the scintillator will be supplemented by 128 channels of silicon detector with 2-mm sensing depth and a pixel pitch of 50 μm , for a single-shot measurement. | 19 |
| 2.5 | Kirchhoff formulation of diffraction by a plane screen. | 20 |
| 2.6 | Kirchhoff formulation of diffraction by a plane screen. | 20 |
| 2.7 | Fraunhofer diffraction on single slit. | 21 |
| 2.8 | Fraunhofer diffraction pattern on single slit. | 22 |
| 2.9 | Schematic of double slit aperture. | 23 |
| 2.10 | Fraunhofer diffraction pattern on double slit. | 24 |
| 3.1 | The resolution is defined where the increment of $x^2/v = 1$. A narrower x^2/v distribution around the $y = x$ line (blue area), a better statistical resolution. The resolution chart can be calculated by comparing each beam size in x and y axes at $\Delta(x^2/v) = 1$, for example at 20 μm beam size, the resolution is a distance between O' and O. | 28 |
| 3.2 | Expected X-ray intensity distribution at the detector (PSF pattern) for a point source in using a pinhole. | 30 |
| 3.3 | Standard deviation of images for various slit widths for LER and HER. The 33 μm slit size was taken as the optimum slit and basic size for both rings. | 31 |
| 3.4 | Pairs of 33 μm slits were simulated with different separations between the pairs (16, 20, 21, 22, 25, 33, and 50 μm). The 22 μm slit separation size is optimal for small beam sizes. | 31 |

| | | |
|------|--|----|
| 3.5 | Expected X-ray intensity distribution at detector (PSF pattern) for a point source using 17 multi-slit. | 32 |
| 3.6 | Series of multi-slit patterns with their resolutions. The spacing size for 15-, 16-, 17.ver1-, and 17.ver2-slits was 13151911319151, 131517191315171, 1213151272151311, and 1315121912131215, respectively. A spacing size of 1 means 22 μm , 2 means 44 μm , 3 means 66 μm , and so on. The 17.ver2-slits achieve better resolution than the others with the small beam sizes that we are interested in ($<30 \mu\text{m}$). | 32 |
| 3.7 | The multi-slit coded aperture pattern, consist of 17-slit with 33 μm and 22 μm as minimum slit and gap sizes, respectively. The holes occupied $\approx 40\%$ of the area. | 33 |
| 3.8 | A simple one-dimensional optimum-coded mask based on the modulo 15 cyclic difference set (0, 1, 2, 3, 7, 10, 11, 13). This figure is adapted from Ref. [35]. | 34 |
| 3.9 | A simple two-dimensional optimum-coded mask based on the modulo 63 cyclic difference set (0, 1, 2, 3, 4, 5, 11, 16, 17, 21, 23, 26, 27, 28, 29, 31, 35, 37, 40, 43, 45, 46, 48, 49, 50, 52, 53, 56, 57, 59, 61). (b) and (c) show two possible designs. This figure is adapted from Ref. [35]. | 34 |
| 3.10 | The URA pattern for XRM, based on the modulo 47 cyclic different set consist of 12-slit with 33 μm and 22 μm as the minimum slit and gap sizes, respectively. The holes occupied $\approx 48\%$ of the area | 35 |
| 3.11 | Expected X-ray intensity distribution at detector (PRF pattern) for a point source using 12-slit URA. | 35 |
| 3.12 | Mask pattern (pinhole, 17 multi-slits, and 12-slits URA) for both rings. The mask consists of 20- μm -thick gold masking material on 600- μm -thick diamond substrates. | 36 |
| 3.13 | Three types of optical elements imaged using a 1000 \times Scanning Electron Microscope: (left) pinhole, (middle) multi-slits, and (right) URA. | 36 |

- 3.14 Simulated detector images showing the number of photons/pixel for single-pass 1 mA bunches for different beam sizes in LER. A series of detector images templates are generated for a range of beam sizes, and these are then compared with the data to find the closest match. (a) Pinhole mask, (b) multi-slits mask consisting of 17 peaks, and (c) URA mask consisting of 12 peaks. The number of peaks represents the number of slits that allow light to pass through. 37
- 3.15 Simulated detector images showing the number of photons/pixel for single-pass 1 mA bunches for different beam sizes in HER. A series of detector image templates are generated for a range of beam sizes, and these are then compared with the data to find the closest match. (a) Pinhole mask, (b) multi-slits mask consisting of 17 peaks, and (c) URA mask consisting of 12 peaks. The number of peaks represents the number of slits that allow light to pass through. 37
- 3.16 Calculated χ^2/v contours for each mask in LER at single-pass 1 mA bunch current. The x- and y-axes are the beam size, to get the resolution we compared it each other at the point where $(\Delta\chi^2/v) = 1$. A narrower χ^2/v distribution around the $y = x$ line, a better statistical resolution that we achieve. The coded apertures show the superiority in resolution compares to pinhole. 38
- 3.17 Calculated χ^2/v contours for each mask in HER at single-pass 1 mA bunch current. The x- and y-axes are the beam size, to get the resolution we compared it each other at the point where $(\Delta\chi^2/v) = 1$. A narrower χ^2/v distribution around the $y = x$ line, a better statistical resolution that we achieve. The coded apertures show the superiority in resolution compares to pinhole. 38

| | | |
|------|--|----|
| 3.18 | Single-bunch, single-turn vertical beam size resolutions for 1 mA bunch current in LER and HER for each optical element (pin-hole, multi-slits, and URA) calculated by comparing each beam size in x- and y-axes of Figs. 3.16, 3.17 at $\chi^2/v = 1$. The 17 multi-slits is estimated to provide 2 – 3 μm resolution for 10 – 25 μm vertical beam sizes at 1 mA bunches. For larger beam sizes ($> 30 \mu\text{m}$), the 12-slits URA mask has better resolution than the 17 multi-slits. | 39 |
| 3.19 | Location of XRM beamline for the LER in Fuji straight-section. | 40 |
| 3.20 | Location of XRM beamline for the HER in Oho straight-section. | 40 |
| 3.21 | Optical system at Fuji straight-section (LER). The X-ray beam goes through the optical elements via a beryllium filter that is placed between the source point and optic box to reduce the heat load. The optical element is mounted on a stage controlled by a stepper motor that allows vertical motion. | 41 |
| 3.22 | Detector system at Fuji straight-section (LER) for Phase 1 commissioning of SuperKEKB operation. The incoming X-rays go through to the scintillator via the Be window. | 42 |
| 3.23 | Detection system at Fuji straight-section (LER) for Phase 1 commissioning of SuperKEKB. Inside the detector box: Be extraction window and a 141- μm -thick YAG:Ce scintillator with CCD camera. The scintillator is tilted 45° in the horizontal plane, so that the camera and lens are out of the way beam. The camera and lens are also tilted 45°, so that they view the scintillator face-on. This does not effect the image in the vertical direction. | 42 |
| 4.1 | XRM panel in the control room, showing LER and HER vertical beam sizes. | 43 |

| | | |
|-----|---|----|
| 4.2 | Schematic for the geometrical scale factors check, consisting of a source point with two beam position monitors (upstream s_1 and downstream s_2), optical elements, and a scintillator. P_1 is the position (in pixels) of a peak feature from X-rays that passed through a slit onto the scintillator and P_2 is the peak feature from X-rays transmitted through the Au mask. | 44 |
| 4.3 | The emittance control knob 'ECK' measurement technique for HER, enlarging the vertical beam size intentionally by making an asymmetric bump. | 47 |
| 4.4 | The $\Delta\varepsilon_y$ knob parameter as a change in vertical emittance for a unit of bump-height squared. | 48 |
| 4.5 | LER emittance control knob data for all optical elements at 200 mA beam current. Data points are fitted using the function in Eq. 4.3 with consistency factor (<i>con</i>) and minimum vertical beam size (σ_{y0}) as free parameters. Phase 1 design value $\varepsilon_y = 10$ pm, measured value $\varepsilon_y = 13$ pm. | 48 |
| 4.6 | HER emittance control knob data for all optical elements at 190~195 mA beam current. Data points are fitted using the function in Eq. 4.3 with consistency factor (<i>con</i>) and minimum vertical beam size (σ_{y0}) as free parameters. Phase 1 design value $\varepsilon_y = 10$ pm, measured value $\varepsilon_y = 160$ pm. | 49 |
| 4.7 | Relation between lifetime and measured beam size for LER (left) and HER (right). By fitting $1/T$ vs $1/\sigma_y$ via linear function $1/T = \alpha_1 (1/(\sigma_y/cal)) + b$, with $\sigma_y = \sqrt{\sigma_{meas}^2 - \sigma_{psf}^2}$. A small value of b , representing non-Touschek lifetime sources. | 51 |
| 4.8 | Relation between lifetime and measured beam size for LER with bunch length correction for each bump height, fitted using Eq. 4.8 to obtain the PSF factor σ_s | 52 |
| 4.9 | Relation between lifetime and measured beam size for HER with bunch length correction for each bump height, fitted using Eq. 4.8 to obtain the PSF factor σ_s | 52 |

| | | |
|------|--|----|
| 4.10 | EGS5 simulation results: (a) X-ray pencil beam from source point passed through the Be filter, optical element, Be window, and onto the YAG:Ce scintillator; (b) Detector (YAG:Ce) pixel arrays, which consist of 50 arrays ($1\ \mu\text{m} \times 1\ \mu\text{m} \times 141\ \mu\text{m}$ for each detector pixel). Yellow and red lines represent photons and electrons, respectively. | 54 |
| 4.11 | Deposited energy in YAG:Ce for given X-ray energy: (a) LER and (b) HER. | 55 |
| 5.1 | Powder pattern obtained from a beryllium window (Air product and Chemicals, 1973) [45]. | 58 |
| 5.2 | Standard deviation of images for various slit widths for LER and HER in Phase 2. The $33\ \mu\text{m}$ ($31\ \mu\text{m}$) slit size was taken as the optimum slit and basic size for LER (HER) ring. | 59 |
| 5.3 | Pentax C1614A lenses for Phase 2 XRM imaging system [48]. | 61 |
| 5.4 | Macro ring to be inserted between lens and camera to shorten the object distance (close up to scintillator) [48]. | 62 |
| 5.5 | A Basler acA2440-20gm CCD camera for the Phase 2 XRM imaging system system [49]. | 62 |
| 5.6 | XRM panel in control room, showing the beam sizes at the XRM source in both rings, emittances, and beam sizes at interaction point. | 63 |
| 5.7 | HER emittance control knob study for URA mask, taken with slow (left) and quick (right) knob scans. We did a quick scan after slow scan to avoid the change of beam condition during the measurements. The consistency factors between measured and SAD simulation beam sizes are 0.996 ± 0.007 and 1.002 ± 0.003 for slow and quick scans, respectively. | 64 |
| 5.8 | The MWI simulation to predict the bunch lengthening with all the wakes: coherent synchrotron radiation (CSR), resistive wall (RW), and geometrical wake (GW), with the σ_{z_0} is $5.33\ \text{mm}$ [50]. | 64 |

| | | |
|-----|--|----|
| 5.9 | Relation between lifetime and measured beam size with bunch length correction for each bump height: (top) slow scan, (bottom) quick scan. Fitted using Eq. 4.8 to obtain the PSF factor σ_s . The average of σ_s was found to be $6.60 \pm 0.73 \mu\text{m}$, which is about 5 times smaller than Phase 1. | 65 |
| 6.1 | The basic concept of coded aperture imaging (adopted from [31]). In an attempt to obtain a higher signal to noise (SNR) ratio, a multiple-pinhole aperture is used to form many overlapping images of the object. There are two steps: the first is physical process, the projection of the source through the aperture; the second process is decoding. | 68 |
| 6.2 | The practical Fresnel zone plate. | 70 |
| 6.3 | Geometrical optic of coded aperture imaging. | 73 |
| 6.4 | Correlation between A_{mask} and G_{mask} | 76 |
| 6.5 | Image reconstruction process using direct deconvolution/FT method: (a) recorded image in 128 pixels, (b) recorded image in 47 pixels, (c) decode image using FT, (d) fitting result. | 76 |
| 6.6 | Image reconstruction process using correlation methods: (a) recorded image in 128 pixels, (b) recorded image in 47 pixels, (c) decode image using correlation method, (d) fitting result. | 77 |
| 6.7 | Comparison of CA deconvolution technique and fitting-template method. | 77 |
| 1 | The geometry used for the treatment of synchrotron radiation, featuring K^* as coordinates system moving along the trajectory. | 84 |

List of Tables

| | | |
|-----|--|----|
| 1.1 | Final machine parameters for the KEKB and SuperKEKB [6, 8–11]. | 6 |
| 1.2 | Beam Instrumentation of SuperKEKB [12]. | 8 |
| 3.1 | Parameters of the optical elements for Phase 1 commissioning. . . | 30 |
| 3.2 | XRM beamline parameters. | 40 |
| 4.1 | Machine parameters in Phase 1 commissioning of SuperKEKB Operation. | 44 |
| 4.2 | Evaluation of geometry scale by tape measurement. | 46 |
| 4.3 | Geometrical scale factors check for LER and HER using the ratio of geometrical magnification M and scintillator camera scale m . The ratios given by tape- and beam-based measurements are agreed within a few percent at both beam lines. | 46 |
| 4.4 | XRM beam parameter during Phase 1 measurement. | 49 |
| 4.5 | Results of the emittance control knob method. From this data, the value of ε_y for LER (HER) is found to be ~ 13 pm (~ 160 pm). This is close to the design value for LER, but much higher for HER, indicating the possibility of a spread function. The PSF was studied using beam lifetime data and the consistency factor con to investigate this discrepancy. | 50 |
| 4.6 | Average of PSF σ_s , minimum vertical beam size σ_{y_0} as fitting results of Figures 4.8 and 4.9, and vertical emittance ε_{y_0} measured with all three optical elements. | 52 |

| | | |
|-----|---|----|
| 5.1 | Parameters of the optical elements for Phase 2 commissioning for HER ring. | 59 |
| 5.2 | XRM beam parameter in HER during Phase 2 commissioning of SuperKEKB Operation. | 61 |
| 7.1 | Vertical beam size measurements in Phase 1 and 2. | 81 |

Bibliography

- [1] KEK Annual Report. 1996. <https://lib-extopc.kek.jp/preprints/PDF/1995/9522/9522001.pdf>.
- [2] SuperKEKB Accelerator Laboratory. http://http://www2.kek.jp/accl/eng/acclmap_superkekb.html.
- [3] Kazuhito Ohmi. Beam-photoelectron interactions in positron storage rings. *Phys. Rev. Lett.*, 75:1526–1529, Aug 1995.
- [4] Y. Suetsugu, K. Shibata, T. Ishibashi, K. Kanazawa, M. Shirai, S. Terui, and H. Hisamatsu. First commissioning of the superkekb vacuum system. *Phys. Rev. Accel. Beams*, 19:121001, Dec 2016.
- [5] Werner Herr and Bruno Muratori. Concept of luminosity. 2006. <https://cds.cern.ch/record/941318/files/p361.pdf>.
- [6] Yuki Yoshi Ohnishi, Tetsuo Abe, Toshikazu Adachi, Kazunori Akai, Yasushi Arimoto, Kiyokazu Ebihara, Kazumi Egawa, and Hitoshi Fukuma John Flanagan, Yoshihiro Funakoshi, Kazuro Furukawa, Takaaki Furuya, Naoko Iida, Hiromi Inuma, Hoitomi Ikeda, Takuya Ishibashi, Masako Iwasaki, Tatsuya Kageyama, Susumu Kamada, Takuya Kamitani, Ken ichi Kanazawa, Mitsuo Kikuchi, Haruyo Koiso, Mika Masuzawa, Toshihiro Mimashi, Takako Miura, Takashi Mori, Akio Morita, Tatsuro Nakamura, Kota Nakanishi, Hiroyuki Nakayama, Michiru Nishiwaki, Yujiro Ogawa, Kazuhito Ohmi, Norihito Ohuchi, Katsunobu Oide, Toshiyuki Oki, Masaaki Ono, Masanori Satoh, Kyo Shibata, Masaaki Suetake, Yusuke Suetsugu, Ryuhei Sugahara, Hiroshi Sugimoto, Tsuyoshi

Suwada, Masafumi Tawada, Makoto Tobiyama, Noboru Tokuda, Kiyosumi Tsuchiya, Hiroshi Yamaoka, Yoshiharu Yano, and Shin-ichi Yoshimoto Mitsuhiko Yoshida, Demin Zhou, and Zhanguo Zong. Accelerator design at SuperKEKB, 2013. <https://10.1093/ptep/pts083>.

- [7] P.Raimondi. 2nd SuperB Workshop, Frascati, 2006.
- [8] T. Adachi K. Akai Y. Arimoto K. Egawa Y. Enomoto J.W. Flanagan H. Fukuma Y. Funakoshi K. Furukawa N. Iida H. Iinuma H. Ikeda T. Ishibashi M. Iwasaki T. Kageyama H. Kaji T. Kamitani T. Kawamoto S. Kazama M. Kikuchi T. Kobayashi K. Kodama H. Koiso M. Masuzawa T. Mimashi T. Miura F. Miyahara T. Mori A. Morita S. Nakamura T.T. Nakamura H. Nakayama T. Natsui M. Nishiwaki K. Ohmi T. Oki S. Sasaki M. Satoh Y. Seimiya K. Shibata M. Suetake Y. Suetsugu H. Sugimoto M. Tanaka M. Tawada S. Terui M. Tobiyama S. Uehara S. Uno X. Wang K. Watanabe Y. Yano S.I. Yoshimoto R. Zhang D. Zhou X. Zhou Z.G. Zong Y. Ohnishi, Abe. Commissioning of the phase-1 SuperKEKB B-factory and update on the overall status. *Proceedings of NA-PAC2016, Chicago, IL, MOB31001*, 2016. <http://www-linac.kek.jp/linac-paper/2016/napac16-ohnishi-commissioning.pdf>.
- [9] SuperKEKB design report, 2014. <https://kds.kek.jp/indico/event/15914/>.
- [10] Ken ichi Kanazawa. Status of superkekb construction. *Nuclear and Particle Physics Proceedings*, 273-275:204 – 209, 2016. 37th International Conference on High Energy Physics (ICHEP).
- [11] KEK Design Report. 2015. http://www-acc.kek.jp/kekb/publication/KEKB_design_report/02.Parameter.pdf.
- [12] M.Tobiyama, M. Arinaga, J.W. Flanagan H. Fukuma, H. Ikeda, H. Ishii, K. Mori, E. Mulyani, M. Tejima, G. Bonvicini, G.S. Varner, and E. Mulyani. Beam Commissioning of SuperKEKB Rings at Phase 1, Feb. 2017. doi:10.18429/JACoW-IBIC2016-MOAL03.

- [13] J.W. Flanagan, H. Fukuma, S. Hiramatsu, H. Ikeda, K. Kanazawa, T. Mitsuhashi, J. Urakawa, G.S. Varner, J.P. Alexander, and M.A. Palmer. X-ray Monitor Based on Coded-Aperture Imaging for KEKB Upgrade and ILC Damping Ring, 2008. <http://accelconf.web.cern.ch/AccelConf/e08/papers/tuocm02.pdf>.
- [14] R.H.Dicke. Scatter-Hole Cameras for X-Rays and Gamma Rays, August 1968. <http://adsabs.harvard.edu/abs/1968ApJ...153L.101D>.
- [15] *Lawrence Berkeley National Laboratory, X-ray Data Booklet, 2nd Edition*. University of California, Berkeley, California, 2009.
- [16] R.P.Feynman et al. *The Feynman Lecture on Physics, Volume I Chapter.34*. Caltech, California, 1963.
- [17] J.D.Jakson. *Classical Electrodynamics*. John Wiley and Sons, Inc, New York, 1975.
- [18] K.J.Kim. Characteristics of synchrotron radiation. *AIP Conference Proceedings*, 184(1):565–632, 1989. <http://dx.doi.org/10.1063/1.38046>.
- [19] Klaus Wille. *Synchrotron Radiation*. Joint Universities Accelerator School, Lecture Note, 2013.
- [20] T. Ericson A. Hofmann and P. Y. Landshoff. *The Physics of Synchrotron Radiation*. Cambridge University Press Cambridge, UK, 2014.
- [21] R. Bartolini. *Synchrotron Radiation*. Joint Universities Accelerator School, Lecture Note, 2013.
- [22] S. Takano. Beam Diagnostics with Synchrotron Radiation in Light Sources. *Proceedings of IPAC Kyoto, Japan*, pages 2392–2396, 2010. <http://accelconf.web.cern.ch/AccelConf/IPAC10/papers/wezmm01.pdf>.
- [23] G.Kube. Review of Synchrotron Radiation Based Diagnostics for Transverse Profile Measurement. *Proceedings of DIPAC Venice, Italy*, pages 6–10, 2007. <http://accelconf.web.cern.ch/AccelConf/d07/papers/moo1a03.pdf>.

- [24] T.Mitsuhashi. Measurement of small transverse beamsize using interferometry. *Proceeding of 5th European Workshop on Diagnostics and Beam Instrumentation, ESRF, Grenoble, France*, pages 26–30, 2001. <https://accelconf.web.cern.ch/accelconf/d01/papers/IT06.pdf>.
- [25] Born Max and Wolf Emil. *Principles of Optics: Electromagnetic Theory of Propagation, Interference and Light Diffraction, 7th(expanded) edition*. Cambridge University Press, Cambridge, 1999.
- [26] T. Mitsuhashi. *Optisc and it's application for beam instrumentation*. KEK, Sokendai, Lecture Note, 2018.
- [27] L.Mertz and N.O.Young. Fresnel transformation of images. *Proceedings of the International Conference on Optical Instrumentation and Technique, Chapman and Hall, London*, page 305, 1961.
- [28] A Sommerfield. *Optics, Lectures on Theoretical Physics, vol. IV*. Press Inc, New York, 1954.
- [29] W.Goodman. *Introduction to Fourier Optics*. McGraw-Hill, New York, 1968.
- [30] P.R.Bevington and D.Keith Robinson. *Data Reduction and Error Analysis for the Physical Sciences*. McGraw-Hill, New York, 2003.
- [31] E.E.Fenimore and T.M.Cannon. Coded aperture imaging with uniformly redundant arrays, Feb 1978. <http://ao.osa.org/abstract.cfm?URI=ao-17-3-337>.
- [32] J.P. Alexander, A. Chatterjee, C. Conolly, E. Edwards, M.P. Ehrlichman, J.W. Flanagan, E. Fontes, B.K. Heltsley, A. Lyndaker, D.P. Peterson, N.T. Rider, D.L. Rubin, R. Seeley, and J. Shanks. Design and performance of coded aperture optical elements for the CESR-TA x-ray beam size monitor, 2014.
- [33] J.Rehm, A.F.D. Morgan, and C. Thomas. Beam diagnostics system for the diamond synchrotron light source. *EPAC2004*, pages 2765–

- 2767, 2004. <http://accelconf.web.cern.ch/accelconf/e04/papers/thplt127.pdf>.
- [34] J.W.Flanagan, A. Arinaga, H. Fukuma, H. Ikeda, A. Lyndaker, D.P. Peterson, and N.T. Rider. High-power tests at CesrTA of x-ray optics elements for SuperKEKB. *IBIC13*, pages 844–847, 2013. <http://accelconf.web.cern.ch/AccelConf/IBIC2013/papers/wepf15.pdf>.
- [35] R. J. Proctor, G. K. Skinner, and A. P. Willmore. The design of optimum coded mask X-ray telescopes. 187:633–643, June 1979.
- [36] J.W.Flanagan, Mitsuhiro Arinaga, Hitomi Ikeda, Ken-ichi Kanazawa Hitoshi Fukuma, Toshiyuki Mitsuhashi, and Gary S. Varner. Design consideration for x-ray beam profile monitor for SuperKEKB. *Proceedings of the 7th meeting of Particle society of Japan*, (2010):618–622. http://pasj.jp/web_publish/pasj7/proceedings/P_4PM/P_EH_4PM/WEPS095.pdf.
- [37] N.Iida, J. W. Flanagan, Y. Funakoshi, and K. Oide. Synchrotron radiation interferometer calibration check by use of a size control bump in KEKB. *Proc. of PAC07, Albuquerque, New Mexico, TUPAN042*, pages 1978–1480, 2007. <http://accelconf.web.cern.ch/AccelConf/p07/PAPERS/TUPAN042.PDF>.
- [38] E.Mulyani and J.W.Flanagan. Calibration of X-ray Monitor during the Phase I of SuperKEKB commissioning. In *Proc. IBIC'16*, pages 525–528, Feb. 2017. doi:10.18429/JACoW-IBIC2016-TUPG72.
- [39] A.Piwinski. *The Touschek Effect in Strong Focusing Storage Rings*. DESY 98-179, 1998. <https://arxiv.org/pdf/physics/9903034.pdf>.
- [40] S.Khan. *Collective phenomena in synchrotron radiatiation sources (Prediction, diagnostics, countermeasures)*. Springer, 2006.
- [41] N.Carmignani. *Touschek lifetime studies and optimization of the ESRF (present and upgrade lattice)*. Springer, 2015.

- [42] H Ikeda and D Zhou. Updated results for bunch length measurements using streak camera, 2016. http://research.kek.jp/people/dmzhou/BeamPhysics/mwi/20160908_Bunch_Length_dmzhou.pdf.
- [43] Andreas Koch, Carsten Raven, Per Spanne, and Anatoly Snigirev. X-ray imaging with submicrometer resolution employing transparent luminescent screens, Jul 1998. <http://josaa.osa.org/abstract.cfm?URI=josaa-15-7-1940>.
- [44] H.Hirayama and Y.Namito. *The EGS5 code system*. KEK, Tsukuba, 2013. http://rcwww.kek.jp/research/egs/egs5_manual/slac730-130308.pdf.
- [45] T. Mitsuhashi. *Private Communication*.
- [46] Jan TouÅ¡, Martin HorvÅ¡th, Ladislav PÅna, Karel BlaÅŸek, and Bruno Sopko. High-resolution application of yag:ce and luag:ce imaging detectors with a ccd x-ray camera. *Nuclear Instruments and Methods in Physics Research Section A: Accelerators, Spectrometers, Detectors and Associated Equipment*, 591(1):264 – 267, 2008. Radiation Imaging Detectors 2007.
- [47] C.Bloomers and J.W.Flanagan G. Rehm. Measurements of small vertical beamsizes using a coded aperture at diamond light source, 2014. <http://www.slac.stanford.edu/econf/C140914/papers/tuczb2.pdf>.
- [48] 2012. http://www.ricoh-imaging.co.jp/english/products/catalog/pdf/2012_PENTAX_MV_eng.pdf.
- [49] <https://www.baslerweb.com/en/products/cameras/area-scan-cameras/ace/aca2440-20gm/>.
- [50] D. Zhou. *Private Communication*.
- [51] E.E.Fenimore T.M.Cannon. Coded aperture imaging: Many holes make light work. *Optical Engineering*, 19:19 – 19 – 7, 1980.
- [52] Marcel J.E.Golay. Point arrays having compact, nonredundant autocorrelations. *J. Opt. Soc. Am.*, 61(2):272–273, Feb 1971.

- [53] R. Accorsi and R. Lanza. Near-field artifact reduction in planar coded aperture imaging. *Journal of Applied Optics (OSA)*, 40(26):4698–4705, 2001.
- [54] C.M. Brown. Multiplex imaging and random array, Ph.D. Thesis, 1972.

Acknowledgments

Alhamdulillah, all the praises and thanks to Allah for His greatness and for giving me the strength and courage to complete this thesis.

This thesis would not have been possible without the support of many people. I would like to take this opportunity to thank all who supported, commented and encouraged me during my thesis period.

First and foremost, I would like to sincerely express my gratitude and appreciation to my thesis advisor, Prof. John W. Flanagan, who has been provided continuous support and guidance throughout my doctoral study. I am always indebted to his constant trust and advice with full of wisdom. It is only with his patient encouragement that I was able to enjoy learn in the field of accelerator physics.

I would like to thank the members of my thesis committee, Prof. Toshiyuki Mitsunashi, Prof. Makoto Tobiyama, Prof. Hitoshi Fukuma, Prof. Takashi Naito, Prof. Gary Varner, and Dr. Hitomi Ikeda, for their careful reviews, as well as the valuable comments and suggestions for improvement of my dissertation. The discussions during the optics and its application for beam instrumentation class that held by Prof. Mitsunashi have been invaluable to clarify my understanding.

I would like to thank all the member of SuperKEKB beam monitoring group, I have had the privilege of working with them and have made contributions to my research experience. Also, I thanks to Gaku Mitsuka for the camera system in the phase 2 commissioning. I would like to thank the members of KEKB commissioning group, Yuki Yoshi Ohnishi, Yoshihiro Funakoshi, Yusuke Suet-sugu, and others for providing the beam and allowing us to do the calibration studies. Also, thanks to Demin Zhou for the bunch length simulation result that very helpful in understanding the XRM systematics.

Particularly, I would like to thank Prof. Tohru Honda, Prof. Shinichiro Michizono from Department of Accelerator Science, also Minami Ono, Noriko Yamamura, Tomoko Yanagisawa, Kenichi Yoshida, Hideaki Onuma, Harumi Michikawa, and Yumemi Katsuki of the KEK SOKENDAI office for their consistent support.

I could not omit to thank many people in BATAN Indonesia especially Prof. Pramudita Anggraita in Center of Science and Accelerator Technology (PSTA), to whom I have always been grateful for introducing me to the field of accelerator physics and encouraged me in the academic life. I would like to acknowledge the Ministry of Research, Technology and Higher Education of Indonesia for giving me a chance to study at SOKENDAI through a Research and Innovation in Science and Technology Project (RISET-Pro) scholarship.

Many of my friends are deserving of acknowledgments for their help and encouragement: Sigit Basuki Wibowo, Widya Rika Puspita, M Abdur Rehman, Kouki Hirose, Liu Na, Du Baiting, and many others. Many thanks to Rifka Juwita, Hani Susanti, Nuri Trianti, Anis Fitri Meiningtyas, Nurul Ainina, Tri Handayani, and many others, for supported me and enriched my life so many ways. Their consistent support and sisterhood enable me to enjoy the life in Tsukuba. The help from Shiori Kanaeda is deeply appreciated, who welcoming and support me a lot during my early life in Tsukuba.

Finally, I want to give my warmest thanks to my family for their love, endless encouragement, and patient.

Emy Mulyani

Declaration

I declare that I wrote this Ph.D.–thesis independently and without any other references and resources than stated in the bibliography. The work was conducted from November 2014 to September 2018 under the supervision of – Professor John W. Flanagan, at the High Energy Accelerator Research Organization (KEK), Oho 1-1, Tsukuba, Japan

Emy Mulyani,